Modelling Brain Tissue using Magnetic Resonance Imaging

Dyrby, Tim Bjørn

Publication date:
2008

Document Version
Publisher's PDF, also known as Version of record

MODELLING BRAIN TISSUE USING MAGNETIC RESONANCE IMAGING

Tim Bjørn Dyrby, BSc.EE., MSc.

Danish Research Centre for Magnetic Resonance, Copenhagen University Hospital Hvidovre, Hvidovre, Denmark

Intelligent Signal Processing Group, Informatics and Mathematical Modelling, Technical University of Denmark, Lyngby, Denmark

Memory Disorders Research Group, Department of Neurology, Rigshospitalet, Copenhagen University Hospital, Copenhagen, Denmark.

Supervisor:
Prof. Lars Kai Hansen,

Funding generously donated by:
The VELUX Foundation and European Union (grant QLRT-2000-00446, Impact of age-related brain white matter changes on transition to disability in the elderly "Leukoaraiosis And DISability").

Ph.D. school
COPENHAGEN IMAGE AND SIGNAL PROCESSING GRADUATE SCHOOL, 2008

Preface

This thesis was submitted as partial fulfilment of the requirements for attaining a PhD degree at the Department of Informatics and Mathematical Modelling (IMM), Technical University of Denmark. The work described herein was primarily undertaken at the Danish Research Centre for Magnetic Resonance (DRCMR), Copenhagen University Hospital Hvidovre, from February 2004 to May 2008.

The project was carried out under the primary supervision of Prof. Lars Kai Hansen from the Intelligent Signal Processing Group, IMM, Technical University of Denmark, under the guidance of the local supervisor at DRCMR, William F.C. Baaré and together with the supervision of Gunhild Waldemar from the Department of Neurology, Rigshospitalet, Copenhagen University Hospital, Copenhagen.

May 2008 // .....

Tim B. Dyrby

Acknowledgments

I am greatful for all my colleagues at DRCMR who were always helpful in supplying useful comments and the wonderful research spirit that exist among the many PhD students at the department. Thanks to Terry Jernigan for some intense talks and your guidance on research problems. Thanks to Egill Rostrup for our many discussions over the years on the LADIS study and to Lars Hanson for staying cool on my flying questions on MRI and q-space. Thanks to Lise V. Søgaard for her encourage in the postmortem scanning and enormously patience for the many questions. To William Baaré and Matthew Liptrot for always being there no matter what, and especially for you teaching me writing scientific English.

From the Research Laboratory for Sterology and Neuroscience, Bispebjerg Hospital, I would like to thank Bente Pakkenberg for a fruitful collaboration and for her taking the time to listen; to Nina Eriksen for helping with the histological staining. Thanks to Jacob Jelsing for introducing me to the histology, the use of pig brains and for a fantastic teamwork over our many scanning weekends and our highly nerdy travels for presenting our work - I am looking forward for our next adventures. Also thanks to Nanna Lind for taking care of the pigs, weekend after weekend while I adjusted and acquired the MRI data.
From the UCL in London I did like to thank Daniel Alexander for a good collaboration and always taking the time when a reconstruction program failed. To Kiran Seunarine for good discussions on tractography and fibre orientated distributions.

From the Manchester University in Manchester I am great full to Geoff Parker for introducing me to the tractography research field, the good discussions and for your advices. Also thank to Hamied Haroon for always being helpful and happy for a quick discussion.
To my supervisor Lars Kai Hansen, I have a smile for you ;-), thanks for your always trusted support and for introducing me to neuroscience and mathematical modelling now many years ago.

The project has not been realised if not Gunhild Waldemar had believed my ideas on tractography. Thanks for giving me the opportunity.

Finally, huge thanks to my friends and family for all your patience, understanding and continuing support. **To my loving wife Lone** *- lets fly on the wings of love and enjoy our precious three children;* ***Clara****,* ***Albert*** *and* ***Oline****.*

This project was generously supported by a grant from *The Velux Foundation* and *European Union (grant QLRT-2000-00446, Impact of age-related brain white matter changes on transition to disability in the elderly "Leukoaraiosis And DISability").*

Table of Content

Manuscript I: Dyrby *et al.* 2008	Dyrby TB., Jelsing J., Alexander D. C., Baaré W.F.C., Søgaard LV., Optimisation of post mortem diffusion-weighted imaging. *Submitted*
Manuscript II: Dyrby *et al.* 2007	Dyrby TB., Søgaard LV., Parker GJ., Alexander DC., Lind NM., Baaré WFC., Hay-Schmidt A., Eriksen N., Pakkenberg B., Paulson OB., Jelsing J. Validation of in vitro probabilistic tractography. Neuroimage. 2007 Oct 1;37(4):1267-1277. Epub 2007 Jul 10.
Manuscript III: Dyrby *et al.* 2008	Dyrby TB., Rostrup E., Baaré WFC., van Straaten ECW., Barkhof F., Vrenken H., Ropele S., Schmidt R., Erkinjuntti T., Wahlund L-O., Pantoni L., Inzitari D., Paulson OB., Hansen LK., Waldemar G. on behalf of the LADIS study group, Segmentation of Age-related White Matter Changes in a Clinical Multi-centre Study. Neuroimage. 2008, doi:10.1016/j.neuroimage.2008.02.024
Manuscript IV: Dyrby *et al.* 2005	Dyrby T. Liptrot MG., Standardizing MR image Intensity In Multi-Center Studies. (Oral presentation) Proc Intl Soc Magn Reson Med 2005. (Miami, USA)

Abbreviation

3D	3 Dimensional
T1	T1 relaxation time
T2	T2 relaxation time
T1W	T1 weighted
T2W	T2 weighted
BDA	Biotin Dextran Amine
BEDPOST	Bayesian Estimation of Diffusion Parameters Obtained using Sampling Techniques
CC	Corpus Callosum
CNR	Contrast to Noise Ratio
CNS	Central Nervous System
CSF	Cerebrospinal Fluid
DNA	Deoxyribonucleic acid
DW	Diffusion-weighted
DWI	Diffusion-weighted Imaging
EM	Electron Microscopic
EPI	Echo Planar Imaging
EU	European Union
FA	Fractional Anisotropy
FACT	Fibre Assignment by Continuous Tractography
FLAIR	FLuid-Attenuated Inversion Recovery
fMRI	Functional MRI
GM	Gray Matter
HARDI	High-Angular Resolution Diffusion Imaging
IVOH	Intravoxel Orientational Heterogeneity
LADIS	Leukoaraiosis And DISability
MD	Mean Diffusivity
MC	Monte Carlo
MCMC	Markov Chain Monte Carlo
MPRAGE	Magnetization Prepared Rapid Gradient Echo
MRI	Magnetic Resonance Imaging
NEX	Number of excitations
PAS-MRI	Persistent Angular Structure MRI
PDF	Probability density function
PGSE	Pulse Gradient Spin Echo
PICo	Probabilistic Index of Connectivity
PNS	Peripheral Nervous System
PVE	Partial Volume Effect
RF	Radio Frequency
ROI	Region Of Interest
SE	Spin Echo
SH	Spherical Harmonics
SNR	Signal to Noise Ratio
VBM	Voxel based morphometry
WM	White Matter
WMC	White Matter Changes

English summary

Diffusion MRI, or diffusion weighted imaging (DWI), is a technique that measures the restricted diffusion of water molecules within brain tissue. Different reconstruction methods quantify water-diffusion anisotropy in the intra- and extra-cellular spaces of the neural environment. Fibre tracking models then use the directions of greatest diffusion as estimates of white matter fibre orientation. Several fibre tracking algorithms have emerged in the last few years that provide reproducible visualizations of three-dimensional fibre bundles. One class of these algorithms is probabilistic tractography. Although probabilistic tractography currently holds great promise as a powerful non-invasive connectivity-measurement tool, its accuracy and limitations remain to be evaluated.

Probabilistic tractography was assessed post mortem in an in vitro environment. Postmortem DWI benefits from the possibility of using high-field experimental MR scanners and long scanning times, thereby significantly improving the signal-to-noise ratio (SNR) and anatomical resolution. Moreover, many of the degrading effects observed in vivo, such as physiological noise, are no longer present. However, the post mortem environment differs from that of in vivo both due to a lowered environmental temperature and due to the fixation process itself. We argue that the perfusion fixation procedure employed in this thesis ensures that the postmortem tissue is as close to that of in vivo as possible. Different fibre reconstruction models were tested on a range of different b-values (a b-value is a summary measurement of the strength of the applied diffusion gradients). We conclude that for robust reconstruction of fibre directions, and subsequently for tractography, b-values in the range of ~2000 s/mm^2 and ~8000 s/mm^2 should be used. Within a two year period, no statistical inter- or intra-brain difference in the diffusion coefficient was found in perfusion fixated minipig brains. However, a decreasing tendency in the diffusion coefficient was found at the last time points about 24 months post mortem and might be explained by an ongoing chemical reaction due to the fixative used. Short-term instabilities within the first 15 hours of DWI scanning were observed and found likely to be caused by the preparation of the postmortem tissue prior to MR scanning. This artefact can be avoided e.g. by simply excluding DW-volumes obtained in the first time period of the scanning session.

Probabilistic tractography was validated against two invasive in vivo neuronal tracers that were used to derive a gold standard. A high spatial agreement between tractography and the gold standard was found, and some of the widely known limitations of tractography methods could be confirmed e.g. uncertainty in regions containing crossing fibres, and definition of tract termination. In the thesis we delve behind the published results to describe all the practical issues that had to be considered in order to ensure a reliable outcome, and a successful experiment. This includes the selection of independent anatomical data to be used to derive a gold standard, the selection of a gyrated animal model in place of the human brain, objective selection of the seed region to initiate, and a waypoint region to constrain the tractography results.

Dansk resumé *(Danish summery)*

Diffusions MRI eller diffusionsvægtet billededannelse (DWI) er en teknik til bestemmelse af vandmolekylers begrænsede diffusion i hjernevæv. Der findes forskellige rekonstruktionsmetoder, som kvantificerer anisotropien af vandets diffusion i det neurale intra- and extracellulære rum. Fibersporingsmetoder anvender retningen for maksimal anisotropi til at bestemme orienteringen af fiberretningerne i den hvide substans. Indenfor de seneste år er flere forskellige fibersporingsmetoder blevet præsenteret, som kan reproducere visaliseringen af de estimerede fiberbundter udfra de estimerede fiberretninger. Probabilistisk traktografi tilhører en af disse sporingsmetoder. Selvom probabilistisk traktografi er en lovende non-invasiv metode til bestemmelse af hjernens konnektivitet, er metodens begrænsninger og præcision ikke dokumenteret.

Probabilistisk traktografi er blevet undersøgt post mortem i et in vitro miljø. Fordelen ved at udføre DWI postmortem er, at der kan anvendes højfelts eksperimentelle MR scannere samt en længere scanningstid, hvorved både signal-støj forholdet og billedets anatomiske opløsning forbedres. Derudover eksisterer mange af de kendte problemer ikke, som er relateret til in vivo eksperimenter, såsom fysiologisk støj. Forskellen mellem in vivo og postmortem er blandt andet en typisk lavere omgivende temperatur idet hjernen er udtaget og at postmortem vævet er fikseret. Vi argumenterer for, at perfusionsfikseringsproceduren anvendt i denne afhandling sikrer, at det fikserede hjernevæv ligner in vivo hjernevæv så meget som muligt. Forskellige fiber rekonstruktionsmodeller er blevet testet på en række forskellige b-værdier (b-værdier udtrykker styrken af de anvendte diffusionsgradienter til optagelse af DWI). For at opnå en robust rekonstruktion af fiberretninger konkluderer vi, at b-værdier bør vælges i området mellem ~2000 s/mm^2 og ~8000 s/mm^2. Indenfor en toårig periode fandt vi ingen signifikant ændring af diffusionkoefficienten hverken mellem eller ved gentagne målinger af de undersøgte minigrisehjerner. Ved de sidste målepunkter omkring 24 mdr post mortem fandt vi dog en tendens til, at diffusionkoefficienten aftager. Det kan sandsynligtvis relateres til fortsatte kemiske reaktioner pga. det anvendte fiksativ. Korttidsustabillitetsartefakter blev observeret i diffusionsbillederne indenfor det første 15 timer af en scanningssession og kan relateres til forberedelserne af postmortem hjernevævet. Artefaktet kan omgåes bl.a. ved at ekskludere DWI data optaget indenfor den første tidsperiode af en scanningssession.

Probabilistisk traktografi blev valideret mod to invasive in vivo neurale tracere avendt som gold standard. Der blev fundet stor spatial overensstemmelse mellem traktografi og gold standard, og traktografimetoders kendte begrænsninger blev bekræftet såsom usikkerhed i regioner indeholdende krydsende fibre og ved terminering. I denne afhandling gennemgåes de praktiske betragtninger, som ligger bag de publiserede resultater. Dette omhandler valget af uafhængige anatomiske data der kan anvendes som gold standard, valget af en dyremodel lignende den humane, det objektive valg af seed region hvorfra traktografien startes samt waypoint region til at specificere fiberbundter sporet med traktografi.

CHAPTER 1

Introduction

Several diseases, injuries and even age-related factors can alter the properties of our brain. For example, dementia is a neurodegenerative disease that leads to substantial white matter (WM) changes that continuously degenerate the fibre bundles within the brain. In the early stages of such disease, the brain remains highly flexible, adapting and compensating for such changes. Therefore, early stages of neurodegenerative diseases cannot easily be detected using traditional somatosensory or cognitive tests. Several initiatives are therefore currently seeking ways to detect and measure early biological markers of this and similar neurodegenerative diseases. Among these, several attempts are ongoing to image early, pre-clinical changes using neuroimaging methods such magnetic resonance imaging. Magnetic Resonance Imaging (MRI) is a non-invasive method for in vivo visualisation of anatomical tissue compositions in the brain. A wide range of different imaging modalities are offered by MRI which allow pathological changes to be assessed from differing perspectives. Therefore, optimally combined imaging modalities are believed to increase both sensitivity and specificity in the search for biological markers of neurodegenerative diseases such as dementia.

This PhD project involves two complementary research paths that use different structural MRI modalities to model brain tissue and which, when united, can produce detailed connectivity maps enhancing the visualisation of degenerated brain regions affected by age or disease.

In the first research path, age-related white matter changes (WMC) which are believed to act as early biological markers for the ensuing development of dementia, were automatically segmented using an optimised artificial neural network. Different MRI modalities were combined to produce six neural networks, each with its own set of input features, for the segmentation of WMC. These were then validated against a clinical multi-centre cohort of elderly subjects (the LADIS[1] study), and the segmentation method with the best *generalization* (a measure of the performance of a neural network, or any other supervised/trained mathematical model) was thus identified (Manuscript III & IV).

Segmenting out the age-related WMC only permits identification of those pathological changes confined to the WM and hence neglects any fibre bundles and GM regions which are concurrently affected. Recently, it has become possible to evaluate anatomical brain connectivity non-invasively by taking advantage of the restricted self-diffusion of water molecules within tissue using diffusion MRI, or diffusion weighted imaging (DWI). Several *tractography* methods (the identification and visualization of fibre bundles in WM based on DWI) have emerged in the last few years which provide reproducible visualizations of three-dimensional fibre bundles. Although tractography currently holds great promise as a powerful in vivo and non-invasive connectivity-measurement tool, its accuracy and limitations remain to be validated. In the second research path, independent anatomical data was used to validate a tractography method (Manuscript II).

1 *Leukoaraiosis And DISsability (LADIS) study, a European 5th Framework project investigating the impact of age-related WMC on the transition to disability.*

However, in order to obtain a reliable validation of tractography methods and to identify where its limitations lay, it was realised that the sources of ambiguity acumulated during acquisition of a DWI dataset and during its progression through the different processing stages, would also have to be determined and minimised (Manuscript I).

In this thesis, focus has been placed upon the second research path which includes both the validation of tractography (Manuscript II) and the optimisation of DWI upon post mortem brains for supsequent tractography (Manuscript I). However the first research path does constitute a substantial part of the PhD project (as Manuscripts III & IV) and is therefore covered in Chapter 6, Conclusion and Future Perspectives.

The thesis comprises the following chapters. Chapter 2 is an introduction to molecular diffusion and brain physiology. Chapter 3 introduces DWI as a measure of the diffusion of water molecules. Relevant reconstruction and fibre tracking methods are reviewed and sources of ambiguity accumulated in the different processing stages are mentioned. Chapter 4 introduces the concept of post mortem imaging and includes the findings of Manuscript I. Chapter 5 covers Manuscript II on validating tractography methods. Here, focus is placed upon the considerations made to ensure a reliable validation. Finally, Chapter 6 draws conclusions over the PhD project as a whole, and offers perspectives into the future.

Aims of the study

- To optimise DWI on perfusion fixated (post mortem) brains such that tractography methods may be applied in a neuroanatomical environment as close to that of in vivo as possible, and yet without many of the problems associated with in vivo imaging that are liable to degrade the accuracy of any tractography approach (Manuscript I).

- To validate the anatomical accuracy of a probabilistic tractography method using independent anatomical data. Two invasive in vivo tracers were used to derive a golden standard (Manuscript II).

- To optimise and validate the generalization abilities of an artificial neural network to segment age-related WMC in a clinical multi-centre cohort (Manuscript III and VI).

Manuscripts

The PhD comprises the following four manuscripts, but this thesis will focus on the content of manuscripts I & II.

I: Dyrby et *al. 2008:*
Dyrby TB., Jelsing J., Alexander D. C., Barré W.F.C., Søgaard LV., Optimisation of post mortem diffusion-weighted imaging. Submitted

II: Dyrby et *al. 2007:*
Dyrby TB., Søgaard LV., Parker GJ., Alexander DC., Lind NM., Hay-Schmidt A., Eriksen N., Pakkenberg B., Paulson OB., Jelsing J. Validation of in vitro probabilistic tractography. Neuroimage. 2007 Oct 1;37(4):1267-1277. Epub 2007 Jul 10.

III: Dyrby et *al. 2008:*
Dyrby TB., Rostrup E., Baaré WFC., van Straaten ECW., Barkhof F., Vrenken H., Ropele S., Schmidt R., Erkinjuntti T., Wahlund L-O., Pantoni L., Inzitari D., Paulson OB., Hansen LK., Waldemar G. on behalf of the LADIS study group, Segmentation of Age-related White Matter Changes in a Clinical Multi-centre Study. Neuroimage. 2008, doi:10.1016/j.neuroimage.2008.02.024

IV: Dyrby et *al. 2005:*
Dyrby T. Liptrot MG., Standardizing MR image Intensity In Multi-Center Studies. (Oral presentation) Proc Intl Soc Magn Reson Med 2005. (Miami, USA)

CHAPTER 2

Principles of diffusion and brain physiology

In diffusion weighted (DW)MRI, the diffusion of water molecules is used to probe tissue microstructures and their environment within the brain. Based on such measurements, detailed anatomical information can be extracted so that the physical properties of the fibre bundles connecting the different brain regions can be estimated and changes due to neurodegenerative diseases can be detected. However, before discussing such advanced measurements, we have to be introduced to the basic principles of molecular diffusion, brain physiology and how to link these two topics. In this chapter, we first describe the basic principles of free as well as restricted diffusion of water molecules. Also, molecular displacement and the diffusion coefficient will be introduced. Then, the neuroanatomical environment of the brain is described from the single neuron to the macroscopic level including the organisation of the cerebral cortical and the fibre bundles. Finally, we link together how water molecules experience the neuroanatomical environment via diffusion, and how this is expected to be reflected in the diffusion coefficient.

2.1 Molecular diffusion

Molecules in a solution are all subject to Brownian motion which is named after the Scottish botanist Robert Brown, who in 1827 observed the irregular motion of pollen grains in liquid suspension under his microscope. It was first in 1905 that this diffusion phenomenon of particles subject to Brownian motion was theoretically described by Einstein (Einstein, 1905).

In the following sections the diffusion coefficient of molecules subject to Brownian motion will be defined and environmental factors that change the diffusion coefficient will be covered in the free as well as in the restricted environment.

2.1.1 Free diffusion

Diffusion can be illustrated by a simple experiment: the spreading of an ink drop in a glass of water. Immediately after the ink has been dropped into the water at time t_o, it will be subject to Brownian motion (by random bombardment of the water molecules) and start to diffuse. After some time t_1, the ink has now started to spread out in the water, and after sufficient time t_2 the colour of the water has become homogeneous as further diffusion is restricted by the surface of the glass and hence the net diffusion ceases. A state of equilibrium of the ink concentration is reached and kept constant by the continuous Brownian motion.

The example illustrates free diffusion which exists in the time period befor the ink reaches the boundary of the glass. Due to Brownian motion each particle experiences a random trajectory in space and thus the ink is isotropically distributed from its initial position.

This physical diffusion phenomenon is described by Fick's second law. However, we must first define Fick's first law that describe the diffusive flux density (J) of a substance, here molecules, which is proportional to the concentration gradient ∇C:

$$J = -D \cdot \nabla C \tag{2.1}$$

where the constant of proportionality, *D (m²/s)*, is the diffusion coefficient.

When substituting Fick's first law in (Eq. 2.1) with the equation of conservation of mass,

$$\frac{\partial C}{\partial t} = -\nabla \cdot J \tag{2.2}$$

Fick's second law is derived,

$$\frac{\partial C}{\partial t} = \nabla \cdot \left(D \cdot \nabla C \right) \tag{2.3}$$

which expresses a prediction on how diffusion causes the concentration field of a substance to change with time.

In case of free diffusion in a liquid, Fick's second law states that the concentration of the diffusing substance, *C*, satisfies a conditional displacement probability density function *p*,

$$p(\mathbf{x}|\mathbf{x}_0, t_d) = \frac{1}{\left(\sqrt{4 \cdot \pi \cdot D \cdot t_d}\right)^3} \exp\left(- \frac{(\mathbf{x} - \mathbf{x}_0) \cdot D^{-1} \cdot (\mathbf{x} - \mathbf{x}_0)}{4 \cdot t_d} \right) \tag{2.4}$$

which is a Gaussian probability density function that describes the probability of a particle that over a time period t_d has diffused to position *x* given its initial position at x_o in space. Now, based on an experiment probing the displacement of molecules using for example diffusion MRI the diffusion coefficient can be estimated, and hence the displacement of diffusing molecules at any time interval can be predicted.

From Fick's second law we see that the diffusion coefficient *D* (length²/time) determines the 'velocity' of the diffusion of e.g. the ink in our hypothetical experiment. If *D* is known, the mean displacement, $r = x - x_o$, that the molecules (e.g. the ink) have diffused over a time period t_d can be expressed by the Einstein equation for molecular displacement in space,

$$\left\langle r^2 \right\rangle = 6 \cdot D \cdot t_d \tag{2.5}$$

where the squared distance r^2 is integrated over space and t_d is the diffusion time.

To describe how environmental factors influence the diffusion coefficient of particles we use the Stoke-Einstein equation,

$$D = k \cdot T \,/(6 \cdot \pi \cdot \eta \cdot a) \tag{2.6}$$

where k is the Boltzmann constant, T the absolute temperature, η the viscosity of the media and a is the radius of the particle.

2.1.2 *Restricted diffusion*

Diffusion over extended periods of time may be hindered or restricted by collisions with boundaries. For example, after time t_2 further diffusion of the ink in the glass of water is restricted by the boundary of the glass. If the molecular displacement is observed at very short time intervals, most of the molecules do not have the time to reach the boundaries and will behave as if they diffuse freely (as described above). However, as the diffusion time increases, a larger fraction of the molecules collide into the boundary and the squared displacement, as given in (Eq. 2.5), will no longer be linearly proportional with the diffusion time. Instead, the displacement probability density function, p, will reflect the spatial dimensions of the boundaries. This is precisely the key feature used in diffusion weighted MRI where water molecules are used as probes to measure the structure of the neuroanatomical environment.

Until now we have assumed that the structural restrictions for the molecular motion are not permeable. However, in a biological environment restrictions are permeable and the degree of permeability varies according to a given situation and tissue type. Permeable restrictions lead to a lowered diffusion coefficient compared to free diffusion.

2.2 The neuroanatomical environment

Two thirds of the human body consists of water and the brain itself consists of 80% water. Thus there are a lot of water molecules in the brain that via Brownian motion can be commandeered to probe the boundaries within the brain tissue. The neuroanatomy of the brain is introduced in this section with a focus upon some of the anatomical structures that might lead to a change of the diffusion coefficient. We first introduce the basic component of the brain, the neuron. Then we move on to the macroscopic level and describe the organisation of grey and white matter.

2.2.1 *The neuron*

The neuron is the canonical processing unit, highly specialised in handling and processing information. The latter refers to the plasticity of the brain, for example relating to the skill of learning. Plasticity is also related to the robustness of the brain to recover or optimise vital brain function after a malfunction, e.g. that caused by a traumatic brain injury (Sidaros et al., 2008). In the brain, some unique neuronal types can be identified according to their location in the nervous system and their distinct shape. Schematically, each neuron has inputs - the dendrites (as well as the cell-body itself), a central command unit - the cell-body, and outputs - the axon terminals (Fig. 2.1).

The cell-body (soma) is the central part of the neuron and includes the nucleus of the cell where the Deoxyribonucleic acid (DNA) is kept. The nucleus controls the activities of the cell by regulating gene expression and hence protein synthesis.

The dendrites branch out from the cell-body of a neuron in a manner akin to a tree ('neuron' is in Greek word for tree) and form connections to the axon terminals originating from a single or many different neurons. The output of the neuron is the axon which starts from the axon hill on the cell-body and ends at the axon terminal(s) where its information is delivered to the synapse. The communication between dendrites and axonal terminals is established in the synaptic cleft where axonal and dendritic synapses interface and communicate via chemical signalling. Based on the information received at the dendrites, the cell-body builds up an action potential and at a certain threshold the neuron begins creating spiking electrical pulses, which then propagate along the axon towards the axonal terminal. The axons conduct information within the CNS and peripheral nervous system (PNS), and can do so over a wide range of distances, e.g. at more than one metre the sciatic nerve is one of the longest axons in the human body, whereas the interneuronal distances within the brain are only a few micrometers. When the electrical signal reaches the synapses at the axonal terminals chemical substances are released in response and these are then delivered either to other neurons, or the neuron itself, via the synaptic cleft.

For an elementary survival in nature, fast reaction time to potentially lethal situations is mandatory (*"observation-decision-reaction"*). This issue is closely linked to a time delay determined by how fast the signal can be propagated along the axon. Evolution has minimised this delay by using myelin. Segments of myelin that are wrapped several times around the axon facilitate the conductance of the electrical impulses along the axons. This myelin sheath is supplied by glial cells which in the CNS comprise oligodendrocyte cells, and in the PNS, Schwann cells. Between each of the segments of the myelin sheath is a small gap of about 1-2 μm. These gaps are known as the 'nodes of Ranvier' and an *internode* is the section between two such nodes. The thickness of the myelin sheath is related to the diameter of the axon, as is the internodal length. In human brains, the size of axons varies in diameter from 1 μm to >10 μm. For example, in corpus callosum the relative axonal diameter varies from 0.4 to > 5 μm (Aboitiz et al., 1992) and in the pyramidal tract from less the 4 μm to >10μm (Graf et al., 1984). The diameter of the axons is related to the speed of the electrical signal *propagating* along it. The thicker an axon, the faster the impulse travels. The shorter axons of interneurons are, on the contrary, often unmyelinated or sparsely myelinated; generally, axons with a diameter less than 2 μm are unmyelinated.

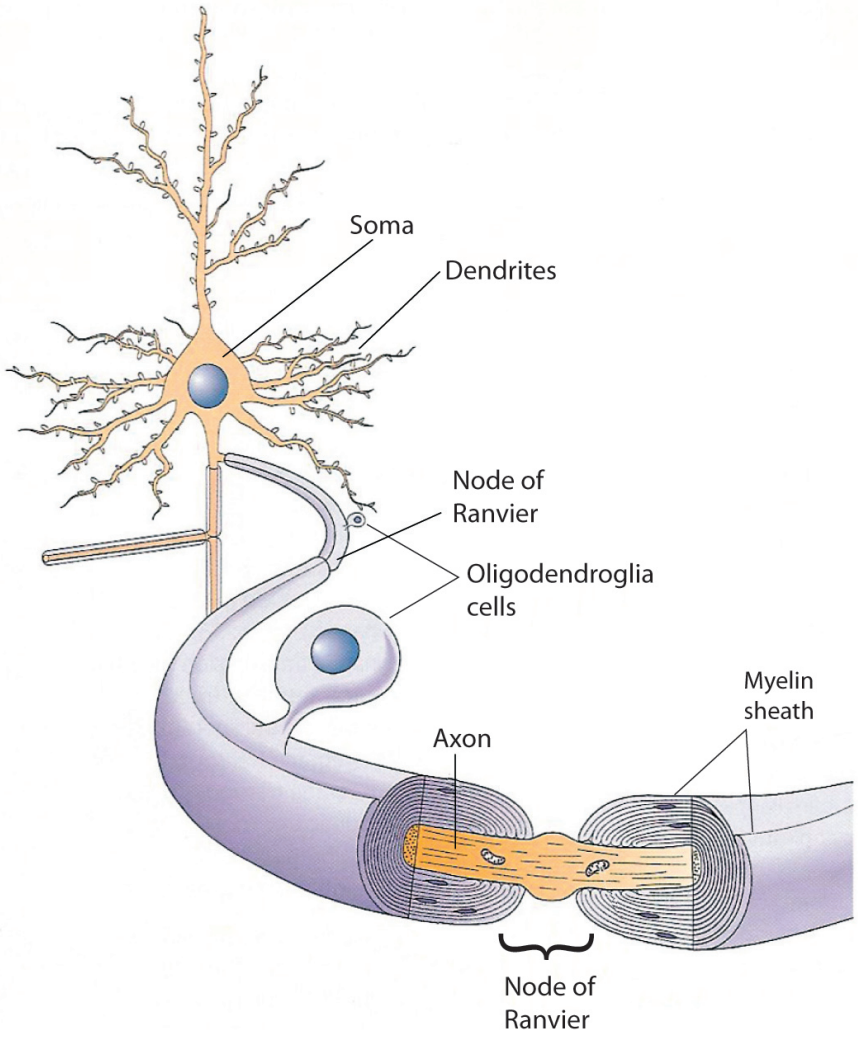

Fig. 2.1 *Basic parts of the neuron in the CNS with myelinated axons. The neuron consists of the cell-body or soma, dendrites that via chemical communication receive information from other neurons and axons along which information toward other neurons is propagated. Myelin sheaths are in segments wrapped around the axon to enhance signalling along the axons and are supplied by glial cells (oligodendrocyte cells) (From Bear et al. 2001).*

2.2.2 Grey matter

The grey matter (GM) is where all the processing of our daily impressions and the handling of our decision making takes place. The major components of GM comprise cell-bodies, glia cells and short neuronal cell extensions (dendrites and short axons). Generally, two types of GM exist within the cerebrum; the cerebral cortex and subcortical GM structures.

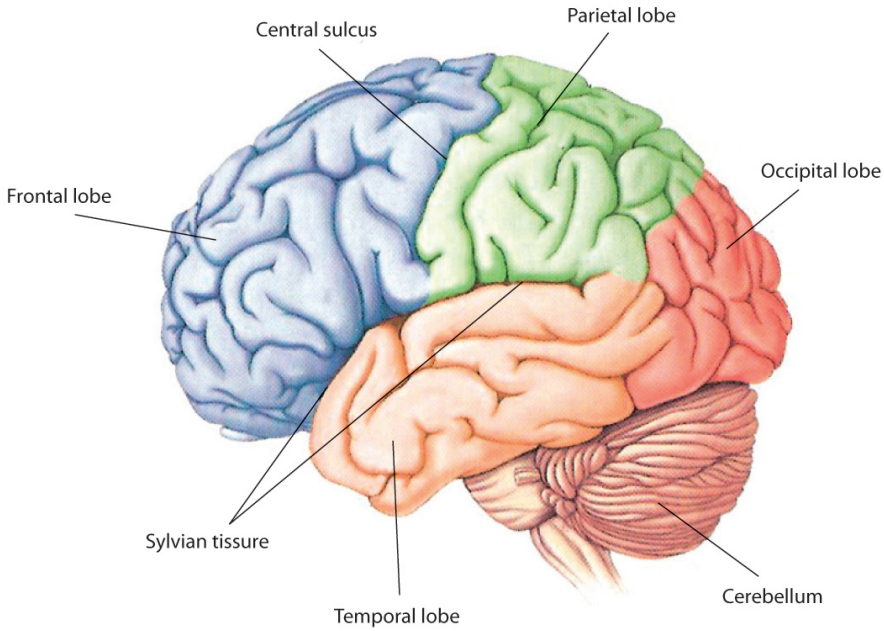

Figure 2.2 *Illustration on how the human cerebral cortex can be subdivided into four regions; the Occipital lobe (red), parietal lobe (green), temporal lobe (orange) and the frontal lobe (blue). Cerebellum is shown as brown. The frontal and the temporal lobe are divided by the sylvial fissure, and the central sulcus divides the frontal and the parietal lobe (From Bear et al. 2001).*

The cerebral cortex is placed at the surface of the cerebrum and consists of laminated sheets of neurons and its supporting tissue. The cytoarchitecture of the cerebral cortex is not homogeneous but varies in both the cell layer and structure. Brodman (1869-1918) created a cytoarchitectonic map of the cerebral cortex and numbered 47 regions wherein the cell layers and structure were uniform. These regions have since been named after him, such was the impact of his work. On the coarser level, the cerebral cortex is normally subdivided into four distinct lobes (Fig. 2.2) each being a centre handling specific tasks (Bear et al., 2001):

· The Occipital lobe: visual perception and processing.

- The Parietal lobe: somatosensory perception, integration of visual and somatospatial (spatial sense and navigation) information and attention.

- The Temporal lobe: language function and auditory perception as well as visual cognition, long term memory and emotions.

- The Frontal lobe: working memory, emotions, reasoning, movement, executive functions, and speech production. It is also involved in purposeful acts such as creativity, judgment, problem solving and planning, and complex cognitive functions; also social cognitive functions.

Subcortical GM structures are GM nucleii placed below the cerebral cortex. The grouping of the smaller GM nucleii together as the basal ganglia (caudate, putamen, pallidum, substantia nigra and hypothalamus), combined with the thalamus, define the subcortical GM structures. Many of the nucleii can be thought of as the data miners of the brain; they filter all the information of the daily impressions we receive and feed the sorted data back to the relevant cortical regions.

2.2.3 White matter

White matter contains all the major fibre bundles within the brain that interconnect the different processing units in cerebral cortex, the subcortical GM and in PNS. We define a fibre bundle to be a bundle of parallel axons that originate and terminate together. The definition of 'fibre bundles' used here is based on the recently published tracer study by (Schmahmann et al., 2006) who used 36 adult rhesus monkey brains to visualise fibre bundles emanating from different cortical regions. In the brain, the fibre bundles always choose when possible the most direct and thus the shortest pathway towards their target. Additionally, axons belonging to the same fibre bundle are not physically held together to form a cable as is the case for the nerve fibres in the PNS. Hence a fibre bundle is more flexible in its radial shape but still consistent as a bundle, even when crossing other bundles. This flexible feature utilises the optimal axonal density within WM, but also means that the axonal density along a specific fibre bundle may seem to vary within a volume of interest (such as within a voxel at the macroscopic scale).

Generally, fibre bundles can be classified into three groups depending on their destination.

Association fibre bundles connect different cerebral cortical regions within the same hemisphere (Fig. 2.3) and can further be subdivided into three groups:

- *Short association* or *U-fibres* are fibre bundles connecting to the adjacent gyrus and run immediately beneath the sixth cortical layer.

- *Neighbourhood association* fibres are placed just next to the U-fibres and typically connect to a gyrus within the same cortical lobe.

- *Long association fibres* connect to adjacent cortical lobes. When they emanate from their starting region, they enter one of the longitudinal fascicules that form the major highways within the brain and exit when approaching their target region in a gyrus. Several distinct fasciculi exists and can be visualised using tractography as shown in Fig 2.4.

Striatal fibre bundles connect to the subcortical GM structures within the striatum.

Cord fibre bundles are typically placed in the middle of the gyrus. When a cord fibre bundle enters deep WM it splits into a fibre bundle connecting to the other hemisphere e.g. contralateral cortico-cortical bundles, and into subcortical fibre bundles, such as the cortico-thalamic and pontine fibre bundles.

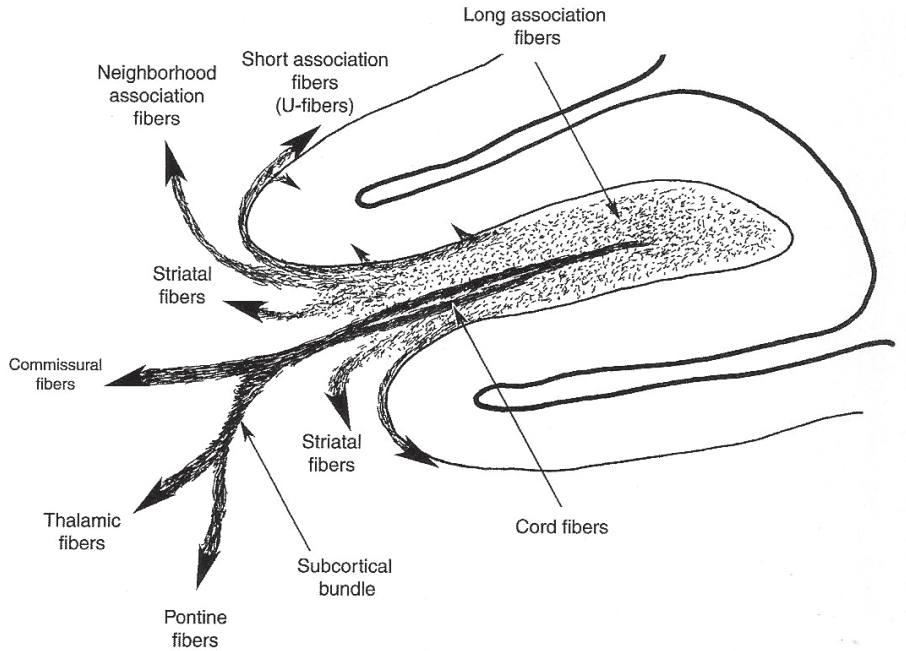

***Fig. 2.3** Diagrammatic representation of the organisation of WM fibre bundles emanating from a gyrus of the cerebral cortex found in the Rhesus monkey brain. Illustration is shown in the coronal plan. Just beneath the cerebral cortex are found the short association fibres or U-fibres that connects the adjacent gyrus. Next to the U-fibre are placed the neighbourhood association fibres, the long, and the striatal fibres. The cord fibre are found in the central of a gyrus and is a consortium of longer distance fibre projections that splits in the deep WM into projections toward the contralateral hemisphere and subcortical GM structures and include thalamic as well as pontine projections (From Schmahmann and Pandya (2006)).*

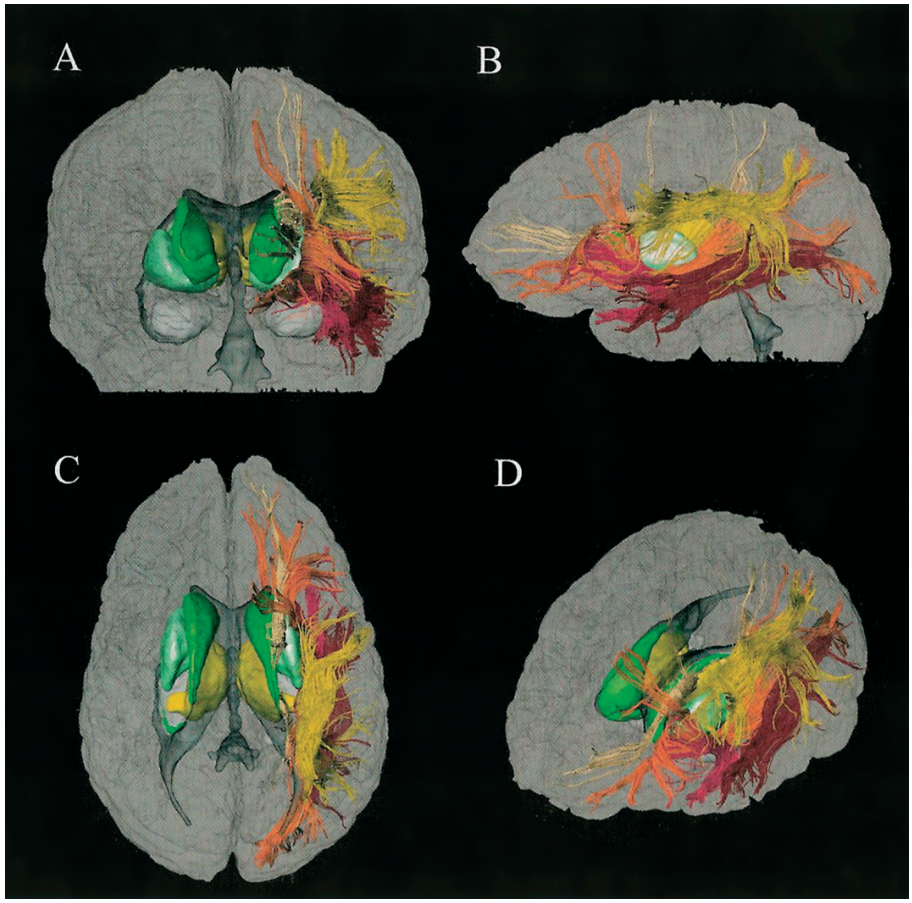

Figure 2.4 *3D visualisation of some of the long association fibres in the human brain using deterministic tractography based on DWI. On a glass brain the fibre bundles are viewed (A) anterior in the coronal plan, (B) left in the sagittal plan, (C superior in the axial plan) and (D) oblique (left-antero-superior) orientation. Colour coding: superior longitudinal fasciculus is yellow, inferior fronto-occipital fasciculus is orange, uncinate fasciculus is red and infiror longitudinal fasciculus is brown. Subcortical GM structures are green (caudate nuclei (dark green) and lentiform nuclei (light green)), thalamus (yellow) and ventricle are grey. Tractography was realised using deterministic streamline fibre tracking based on the FACT method (Mori et al., 1999). The domination fibre direction in a voxel was reconstructed from the DWI dataset using the tensor method and the in vivo DWI dataset was obtained using a b=700 s/mm² and a sampling scheme containing 30 DW directions. Constrained tractography using waypoint regions were used to segment out the different fibre bundles (From Mori et al. (2005)).*

2.3 Cellular structure

In the following section, the principles of molecular diffusion (section 2.1) are linked to the neuroanatomical environment (section 2.2) by identification of restrictions and environmental factors that are expected to be reflected in the diffusion process. We assume that the environment temperature within the neuroanatomical environment is constant and the molecular diffusion to be determined is based on water molecules.

2.3.1 Intra- and extra-cellular spaces

The intra- and extra-cellular spaces are separated by the cell membranes. In the brain, the extra-cellular space comprises 20% of the brain tissue volume and the composition includes metabolites, ions, proteins and many other substances that might affect cellular function e.g. as a result of drug delivery. Water molecules moving around freely in such a mixture of substances are slowed down due to both chemical reactions and brief bondings with them. Therefore, one would anticipate that the diffusion coefficient of the extra-cellular space be lowered than that of (pure) water, and this is precisely as predicted by the Stoke-Einstein equation (Eq. 2.6).

Within the extra-cellular space, directional restrictions to molecular diffusion in GM are dominated by the membranes of the cell-bodies and dendrites which vary in size and form. As a result, at the macroscopic level the restrictions appears highly unstructured and so no dominating structural orientation is expected. If the diffusion time is long enough that most molecules experience hindrance, then these randomly organised structures restrict molecular diffusion in such a way as to reflect the average displacement. In WM the molecules experience some structured and directionally-dependent hindrance due to the densely packed and co-aligned axons. However, the many oligodendrocytes which wrap the myelin sheath around these axons and blood vessels might disturb this picture of structured organisation. Therefore, the diffusion coefficient along the axons in the extra-cellular space is expected to reflect some of this hindrance lowering the diffusion coefficient when compared to free diffusion. Nevertheless, the diffusion coefficient is still expected to be higher than that radially to the axons and hence some anisotropic diffusion can be expected in the extra-cellular space.

The intra-cellular space occupies about 80% of the tissue volume in the brain and consists of cytoplasm which is a gelatinous, semi-transparent fluid that fills most cells. Besides water, the cytoplasm, similar to the extra-cellular space, also comprises ions, proteins etc.
The axon is akin to a long (flexible) tube, full of cytoplasm and containing a cytoskeleton. The latter determines the structure of the axon (and also the cell body) and consists of microtubules (in diameter) (~20 nm), neurofilaments (~10 nm) and microfilaments (~5 nm) (Bear et al., 2001). Both types of filaments have a random structure, in contrast to the microtubules which are highly organised along the axons. Actually, microtubules are analogous to a rail network along which other particles such as protein molecules are transported from the cell body towards the synapses (anterograde transportation), and vice versa for retrograde transportation. The microtubules play an essential role in delivering material along the axon, so much so in fact that, if they were to fail, it would cause the neuron to starve and eventually die. Microtubules originate from the axon hill of the cell body

and terminate at the synapse, and their organisation within the axon can be inspected by electron microscope (EM) (see e.g. Beaulieu, (2002)).

The restrictions in the intra-cellular space of WM tissue are highly organised and structured along or axial to the axons. In this direction, molecular diffusion is expected to be almost unrestricted, with a diffusion coefficient toward that of free diffusion, and the slight reduction caused by the substances within the cytoplasm. Radial to the axons, diffusion is restricted by the cell membrane and in part by the microtubules. The diffusion coefficient in this direction is therefore lower than that along the axons. This assumes that the diffusion time has been so long that most molecules have experienced the restrictions.

As mentioned in the previous section, these structural hindrances can vary in permeability. In WM, axons are closely wrapped with myelin sheaths and the permeability of the cell membrane between the intra- and extra-cellular space is very low. However, in cases of neurodegenerative diseases such as multiple sclerosis the myelin sheaths are degenerated and the axonal membrane becomes more permeable. In GM, it is only the cell membranes that separate the different cellular spaces. They control the flux of water molecules in and out of the cell and hence are permeable.

CHAPTER 3

Diffusion weighted imaging and tractography

Diffusion weighted magnetic resonance imaging (DWI) provides a unique probe into the microstructure of brain tissue by sampling the diffusion properties of water on a microscopic scale much smaller than the macroscopic imaging voxels. Importantly, DWI allows us to probe the properties of water diffusion in various angular directions and hence the diffusion properties of the neuroanatomical environment, described in the previous chapter, can then be modelled and the fibre bundles visualised using tractography.
In this chapter, we first offer an introduction to DWI and the methods used to derive the diffusion coefficient from such diffusion measures. (For a general introduction to the basics of MR, see the Appendix). Secondly, the most widely used reconstruction algorithms, which extract the voxel-wise orientations of the axonal fibres bundles used for fibre tracking, will be reviewed and their pros and cons discussed. Deterministic and probabilistic fibre tracking methods, used to determine a more macroscopic picture of the fibre bundles from such voxel-wise representations, are then also reviewed and discussed. Finally, we list the different sources of ambiguity that are accumulated along the different stages of realizing tractography, and how each of these adds to the uncertainty of the fibre tracking.

3.1 Diffusion weighted Imaging

The displacement of water molecules subjected to Brownian motion can be probed in the microstructure of the neuroanatomical environment by DWI. Specifically, DWI measures the displacement probability density function of molecular displacement, observed over a fixed diffusion time, and hence estimate the diffusion coefficient as was described by Fick's second law in the previous chapter.

3.1.1 Probing diffusion using MRI

In DWI, the diffusion of water molecules is first sensitized by bipolar magnetic field gradients in a Pulsed Gradient Spin Echo (PGSE) sequence (Stejskal et al., 1965). In a magnetic field gradient, the protons of the moving water molecules undergo phase shifts of their transverse magnetization. Hence, the basic idea of PGSE is first to label the spins with a position dependent phase shift. Then the molecules are allowed to diffuse over a short time period, whereafter the spins are measured at their new positions. The displacement is then derived from the loss of phase coherence of the spins.

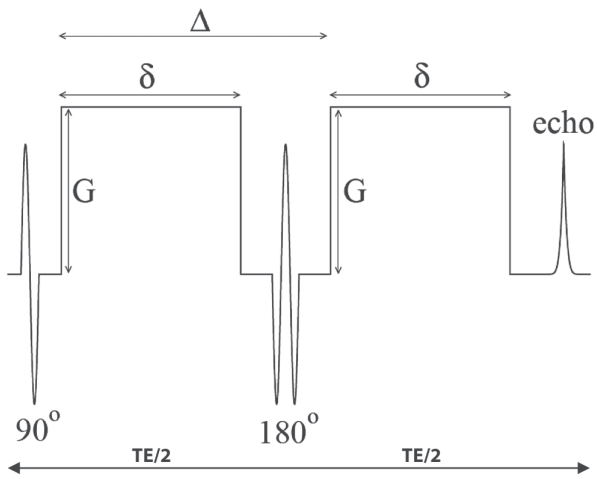

Fig. 3.1 *Schematic diagram of the PGSE sequence used to measure molecular diffusion with MRI along a single direction in space. Time is from left to right. After the 90 degree excitation RF pulse, the first diffusion weighting gradient G labels the spins with a position dependent phase shift along a single direction in space which is determined by the gradient, G(x,y,z). At TE/2, a 180 degree RF pulse inverts the phase shift of the spins before the second diffusion weighted gradient is applied to 'unlabel' or rephase the spins. Spins that have moved within a diffusion time* t_d *(*$t_d = \Delta - \delta/3$*) along the direction determined by the gradient introduce a net dephasing of the transverse magnetisation. The signal is measured as an echo that appears after TE (Courtesy of Dr. Daniel Alexander).*

Fig. 3.1 shows a schematic of the PGSE sequence. In detail: Stage I) a 90 degree excitation RF pulse rotates the spins into the transverse plane where they precess in phase at the Larmor frequency. Stage II) The first diffusion weighting gradient pulse (G) induces a phase shift $\varphi_1(x_1)$ of the spins dependent upon their location (x_1) along the gradient direction. The labelling of the spins is then expressed as

$$\phi_1 = \int_0^{\delta} \gamma \cdot G \cdot x_1 dt = q_1 \cdot x_1 \qquad (3.1)$$

where $q = \gamma\, G\, \delta$ (m^{-1}) is defined as "the wavevector", γ is the gyromagnetic ratio, G the strength of the diffusion weighting gradient pulse and δ the time period of the gradient pulse. We assume constant spin position during the short duration δ of the gradient pulse. Then in Stage III), after a 180 degree RF pulse, the phase shift of all spins are inverted ($\varphi_1 \rightarrow -\varphi_1$). Stage IV) The second diffusion-weighting gradient pulse, identical to the first one ($q_1 = q_2$), induces a phase shift $\varphi_2(x_2)$, thus rephasing the spins, (Eq. 3.2).

$$\phi_2 = \int_{\Delta}^{\Delta+\delta} \gamma \cdot G \cdot x_2 dt = q_2 \cdot x_2 \qquad (3.2)$$

Hence, the net dephasing $\upsilon(\varphi)$ of the spins between labelling (Stage II) and rephasing (Stage IV) is found by subtracting (Eq. 3.1) and (Eq. 3.2):

$$\upsilon(\phi) = \phi_1 - \phi_2 = q \cdot (x_1 - x_2) \qquad (3.3)$$

Any spins which have not moved at all ($x_1 = x_2$), or those that have only moved perpendicular to the gradient direction during spin labelling and rephasing, will experience an average dephasing of zero. However, any spins moving non-perpendicular to the gradient direction will experience an average net dephasing that will depend upon the spin history acquired during the time period between gradient pulses, and this will hence attenuate the transverse magnetisation signal measured by MRI. Hence from Eq. 3.3, the maximal displacement which can be detected over time period t_d is determined by the selected q value. When using the PGSE sequence the effective diffusion time at which the molecules can move is defined as $t_d = \Delta - \delta/3$.

The displacement probability density function has been shown to be related to the measured MRI diffusion signal A^* by a Fourier transformation (Stejskal et al., 1965). The diffusion weighted signal measured by wavevector q is then

$$A^*(q) = A_0 \int p(x) \exp\left(i \cdot q \cdot x\right) dx \qquad (3.4)$$

where $p(x)$ is the displacement probability density function of water molecules conditioned on the diffusion time t_d. A_o include an unwanted T2W signal contribution included in the measured signal and occurs because of the time the gradients are applied which prolong the TE and hence introduce the T2 weighting.

To exclude the T2 shine-through effects in the diffusion weighted measurement in Eq. 3.4, a separate spin-echo image A^*_o with no diffusion weighting $(q = 0)$ is measured and used for normalisation of $A^*(q)$. Then, after normalisation of the two MRI measurements, $p(x)$ of the cellular structure along a single direction can be derived from:

$$A(q) = \frac{A^*(q)}{A^*_0} = \int p(x) \exp(\, i \cdot q \cdot x)\, dx \tag{3.5}$$

In practice, only the magnitude of the complex MRI signal is sensitive to diffusion (the phase is sensitive to flow). However, since the phase does not provide any additional information regarding the diffusion weighted signal, it can be safely ignored. Also, we assume *p(x)* to be symmetric, i.e. *p(x) = p(-x)*. An approximation of Eq. 3.5 can then be written as:

$$A(q) = \frac{A^*(q)}{A^*(0)} \approx \int p(x) \cos(\, q \cdot x)\, dx \tag{3.6}$$

It is assumed that, similar to (Eq. 2.4), the displacement probability density function of water molecules is a Gaussian probability density function and conditioned on the diffusion time, t_d. Thus along a single diffusion weighted (DW) direction (1D) we have:

$$p(x, t_d) = \frac{1}{\sqrt{4 \cdot \pi \cdot t_d \cdot D}} \exp(\, - \frac{x^2}{4 \cdot D \cdot t_d}) \tag{3.7}$$

where *D (m²/s)* is the diffusion coefficient. Substituting of Eq. 3.7 into Eq. 3.5

$$A(q) = \frac{A^*(q)}{A^*_0} = \exp(\, -q^2 \cdot t_d \cdot D) \tag{3.8}$$

It can be seen that the normalised diffusion weighted signal *A(q)* along a single DW-direction decreases exponentially with a decay determined by *D,* as one would expect from consideration of Eq. 3.3. For simplicity, the sequence related parameters q^2 and t_d are typically merged and defined as a b-value. Substituting this b-value into Eq. 3.8 and solving for the diffusion coefficient:

$$-\log\left(\frac{A^*(b)}{A^*(0)}\right)\frac{1}{b} = D \tag{3.9}$$

In the case of MRI the image resolution is limited and to indicate the presence of partial volume effects (PVE) between different cellular structures and that the probability density function at the microscopic scale is non-Gaussian, the diffusion coefficient is defined as an *apparent* diffusion coefficient, $D_{a,}$ but still at the macroscopic level assumed to be Gaussian distributed.

3.1.2 *Sampling scheme*

A sampling scheme includes a series of angular directions, each being a unit vector defined from the centre of the unit sphere to a point on its surface. Then, simply by repeating Eq. 3.4 with DW-gradients (constant q value) applied along each direction of the sampling scheme the molecular diffusion is measured on a single shell in q-space having a radius determined by the q value (note, since the signal in DW measurements depend on q value the measurement space is denoted 'q-space' see (Callaghan, 1991)). Based on these discrete measurements different reconstruction models can be applied and the cellular structure visualised. The obtained DWI dataset then includes a series of dw images: $A^*(q^1)$, ..., $A^*(q^N)$ where N is the number of angular directions in the sampling scheme, and a single non-dw image, A^*_o, used for normalisation.

Because molecular diffusion is quadratic, the sampling scheme only includes non-collinear directions. Also, since the micro-structures to be probed are randomly orientated in space, the non-collinear directions are equally distributed on the unit sphere (Jansons et al., 2003;Jones et al., 1999;Skare et al., 2000). This ensures that the measurements are rotationally invariant. The optimal number of DW-directions needed is still a matter of debate within the diffusion community, however the minimum number of directions required is well-defined and is dependent upon the reconstruction model used. For example, at least six DW-directions are needed for a valid reconstruction using the tensor model (Basser et al., 1994;Basser et al., 1998) which is a 3D version of Eq. 3.11 (see next section). However, to ensure rotational invariance of the tensor model, Jones (2004) simulated that 20 DW-directions should be selected. In terms of tractography, the angular accuracy of the sampling scheme becomes increasingly important in regions with complex fibre compositions such as crossing fibres. In such cases so called High-Angular Resolution Diffusion Imaging (HARDI) acquisitions are preferred, but a trade off between scanning time and the signal-to-noise ratio (SNR) typically limits the number of directions to between 30 and 61 (Behrens et al., 2003;Behrens et al., 2007;Berman et al., 2008;Jones et al., 2005;Mori et al., 2005;Parker et al., 2003b;Parker et al., 2003a;Parker et al., 2005).

3.2 Reconstruction algorithms

A reconstruction algorithm accepts a DWI dataset, comprising a sampled version of the molecular diffusion in three-dimensional space, as its input. For each voxel in the brain volume, the shape of $p(x)$ given a diffusion time is then modelled to determine the dominating fibre directions, approximating the true underlying function as determined by cellular structures such as densely packed fibre bundles. After reconstruction, the dominating fibre directions are identified in each voxel thus generating a vector field of local fibre directions which can then be used for fibre tracking, as described in the following section.

3.2.1 Single fibre model

The diffusion tensor (DT) model (Basser et al., 1994) is a 3D version of Eq. 3.7 and computes the apparent diffusion tensor based on the assumption that $p(x)$ is a zero-mean trivariate Gaussian distribution:

$$p(\mathbf{x}) = G(\mathbf{x} \mid \mathbf{D}_a, t_d) \tag{3.10}$$

where

$$G(\mathbf{x} \mid \mathbf{D}_a, t_d) = \frac{1}{\sqrt{(4 \cdot \pi \cdot t_d)^3 \det(\mathbf{D}_a)}} \exp\left(-\frac{\mathbf{x}^T \mathbf{D}_a^{-1} \mathbf{x}}{4 \cdot t_d}\right) \tag{3.11}$$

D_a is the diffusion tensor (a 3x3 matrix) to be modelled after diffusion time t_d. Substituting Eq. 3.10 into Eq. 3.5 we obtain a relation to our measurements in image space:

$$A(\mathbf{q}) = \exp(-t_d \cdot \mathbf{q}^T \cdot \mathbf{D}_a \cdot \mathbf{q}) \tag{3.12}$$

where q is a vector of sampled points in space determined by the sampling scheme used.

Taking the logarithm on both sides and replacing q with the b-value ($b = q^2 \cdot t_d$)

$$-\log(A(\mathbf{b})) = \mathbf{b}^T \cdot \mathbf{D}_a \cdot \mathbf{b} \tag{3.13}$$

we have a system with linear constraints on D which can be estimated by an eigenvalue decomposition see e.g. (Mori, 2007) in which the eigenvectors ($\upsilon_1, \upsilon_2, \upsilon_3$) effectively determine the principal orientation of the tensor model relative to the laboratory frame system, and the three eigenvalues determine the apparent diffusion coefficient along each eigenvector, as illustrated in Fig. 3.2. Hence, the three ordered eigenvalues $\lambda_1 \geq \lambda_2 \geq \lambda_3$ determine the shape of the probability density function p and provide rotationally invariant statistics of the anisotropy of p. In WM fibre bundles the first eigenvector estimates the axial diffusivity along the fibre bundles and the second and third eigenvalues estimate the radial diffusivity perpendicular to the fibre bundles. From these eigenvalues the mean apparent diffusivity (MD) can then be calculated:

$$MD = (\lambda_1 + \lambda_2 + \lambda_3)/3 \tag{3.14}$$

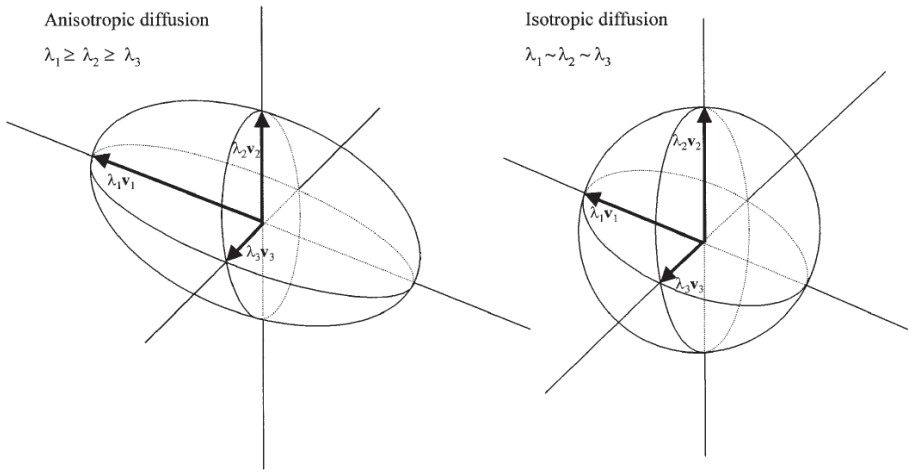

***Fig. 3.2** Shape of the displacement probability density function when reconstructed using the tensor model. The three sorted eigenvalues λ_1, λ_2 and λ_3 with the first being the largest, express the apparent diffusion coefficient along the principal directions; υ_1, υ_2 and υ_3. In voxels containing anisotropic diffusion the largest diffusivity (λ_1) is found along or axial to e.g. the WM fibres bundles in the direction determined by υ_1. Isotropic diffusion is when no dominating fibre orientation exist ($\lambda_1 \sim \lambda_2 \sim \lambda_3$) and can be found in e.g. cerebrospinal fluid (CSF) (From Wiegell et al. 2000).*

The MD does not provide information on the degree of diffusion anisotropy; therefore, approaches have been suggested to produce informative, normalised and orientation-invariant diffusion anisotropy measures (for comparison (Papadakis et al., 1999)). The most widely used is the Fractional Anisotropy (FA) measure which is a variance measure of the eigenvalues. The FA measure is defined as:

$$FA = \frac{\sqrt{3 \cdot \left((\lambda_1 - MD)^2 + (\lambda_2 - MD)^2 - (\lambda_3 - MD)^2 \right)}}{\sqrt{2 \cdot (\lambda_1^2 + \lambda_2^2 + \lambda_3^2)}} \tag{3.15}$$

An FA value of zero represents isotropic diffusion, which can, for example, be observed in CSF, and a value of one is maximal anisotropic diffusion. In brain tissue high FA values are typically found in corpus callosum and here the FA value reaches about 0.8 (Bonekamp et al., 2007;Marenco et al., 2006). For orientational visualisation, the FA map can be colour coded in (Red-Green-Blue) RGB colours in accordance with one of the principal directions. Typically υ_1, which determines the direction of axial diffusivity, is used for this purpose (Pajevic et al., 1999).

Importantly, although the MD and FA maps are extremely powerful tools in extracting quantitative measures of the cellular structures and can be used both in voxel based analysis, e.g. traumatic brain injury (Sidaros et al., 2008), brain maturation (Mukherjee et al., 2002;Zhang et al., 2005), and in examining anatomical microstructures (manuscript I, Dyrby et al 2008), they still rely on a reconstruction which is based upon a simple tensor

model. Therefore, great care must be taken to differentiate between true anatomically-related changes such as myelin loss and effects caused by crossing fibre situations where the tensor model fails. In both situations a lowered FA value is produced (see Fig. 3.3 for example). Tensors having such a resulting oblate (pancake-like) shape are an indication of intravoxel orientational heterogeneity (IVOH), something which is typically observed in regions containing crossing fibres (Tuch et al., 2002).

3.2.2 Multiple fibre models

Multiple fibre models have been designed for a more reliable reconstruction of the shape of the anisotropy, and hence also of *p*, in situations where IVOH departs from the Gaussian model, e.g. in crossing-fibre situations.

Mixture of Gaussian probability density functions: The tensor model of the displacement probability density function in Eq. 3.10 can be expanded from a single Gaussian probability density function to a mixture of them (Bishop, 1995), and when Fourier-transformed (Eq. 3.10) can be written as:

$$A(\mathbf{q}) = \sum_{k=1}^{m} \alpha_k \exp(-\mathbf{b}^T \cdot \mathbf{D}_a^k \cdot \mathbf{b}) \qquad (3.16)$$

where the mixer variable α_k controls the importance of the individual Gaussians and yields $\sum_{k=1}^{m} \alpha_k = 1$.

In contrast to the single tensor model in Eq. 3.12, an iterative optimisation method is used to ensure an optimal fit of the Gaussian mixture model to the DWI dataset. Tuch et al. (2002) used the gradient descent optimisation procedure and added different physiological constraints on the eigenvalues e.g. a volume fraction, to avoid overfitting. They noticed difficulties when fitting more than two Gaussians. Even though reliable results were obtained in regions known to contain crossing fibres, such as in the centrum semiovale where fibre bundles from the corona radiata and corpus callosum cross, a clear disagreement could be observed between the reconstructed principal directions and the actual fibre directions expected from the measurements in the DWI dataset acquired – an indication that the reconstruction method has reached a local minimum and thus a suboptimal fit. The changeling of the mixture of Gaussian probability density function model is how to identify single- and multi-fibre situations, where the single tensor and the mixture model should be used, respectively. The advantage of using the mixture of Gaussians probability density function model is that as soon as a crossing fibre situation is encountered and modelled, the exact orientation of each fibre bundle is given by the principal direction ($\upsilon_{1,k}$) of each Gaussian density function.

Spherical harmonic decomposition: We assumed for both the tensor model (Eq. 3.10) and the mixture of Gaussians probability density function model (Eq. 3.16) that the probability density function was a zero mean trivariate function. It was also assumed that a DWI dataset could contain a series of diffusion weighted measurements sampled in any number of

angular directions equally distributed on a sphere. With these constraints on our model, our aim to model anisotropy (or the shape of p) can then be expressed in terms of fitting functions on the sphere. Any function of the sphere $f(\theta, \varphi)$ can be modelled or decomposed into a series of spherical harmonic (SH) basis functions:

$$f(\theta,\varphi) = \sum_{l=}^{L} \sum_{m=-l}^{l} a_{l,m} Y_{l,m}(\theta,\varphi) \tag{3.17}$$

where $Y_{l,m}(\theta, \varphi)$ is a spherical basis function and $a_{l,m}$ is a factor indicating its importance. A spherical harmonic series containing orders up to $l = L$ is equivalent to an order L polynomial on the sphere.

Frank (2002) fitted a spherical series to the DWI dataset and found that a "two crossing fibres" situation (defined as a non-Gaussian case) was consistently reconstructed using a series of SH with $L = 4$. For comparison, with $L = 2$ the SH series equals anisotropy of a tensor model, and when $L = 0$ the SH equals isotropy. Because diffusion is bidirectional, and hence the anisotropy symmetrical, only even orders of SH should be included. Notably, Frank also demonstrated that by simple inspection of each SH component it was possible to determine the number of fibres that have been modelled. Alexander et al 2002 presented a segmentation method based on a truncation of SH and a statistical variance analysis (f-test) to classify voxels into three classes: Gaussian isotropic, Gaussian anisotropic and non-Gaussian probability density functions. The disadvantages with using SH to model multi-fibre situations is that the model does not provide any directional information on the principle fibre directions. However, combining the voxel segmentation method based upon SH and e.g. the tensor mixture Gaussian probability density function model, the principle directions of each fibre can be determined and used for tractography (Dyrby et al., 2007;Parker et al., 2003a). Alternatively, other techniques to search for dominating peaks on a sphere can be used as well.

Persistent angular structure (PAS) MRI: Janson and Alexander (2003) introduced PASMRI which is a special case of spherical deconvolution. The PAS is the function $\widehat{p}$ on the sphere that, when embedded in thee-dimensional space on a sphere of radius r has the Fourier transform that best fits the measurements. In the case of diffusion, the measurements are the DWI dataset and so the PAS function is collapsed onto a single shell in q-space by using the approximation:

$$p(\mathbf{x}) \approx \widehat{p}(\hat{\mathbf{x}}) \cdot r^{-2} \cdot \delta(|\mathbf{x}| - r) \tag{3.18}$$

where δ, in this context, is the Dirac delta function, $\hat{\mathbf{x}}$ is a unit vector parallel to x, and $\widehat{p}$ is the PAS. Substituting Eq. 3.18 into Eq. 3.6 gives:

$$A(\mathbf{q}) = \int \hat{p}(\hat{\mathbf{x}}) \cos(\ 2 \cdot \pi \cdot r \cdot \mathbf{q} \cdot \hat{\mathbf{x}}) d\hat{\mathbf{x}} \qquad \textbf{(3.19)}$$

where the integral is performed over the unit sphere.

For optimisation, the Levenberg-Marquardt algorithm was used, the objective function was a maximum-entropy parameterization of $\widehat{p}$, and the integral in Eq. 3.19 was solved by numerical approximation. The parameter r controls the smoothness of $\widehat{p}$ and was empirically determined to be $r = 1.4$ (Jansons et al., 2003).

The PAS function provides fibre orientated estimates and can model any number of symmetric peaks. Hence, the function has no relation to the radial structure of $p(x)$ as, for example, the tensor model does. As for SH, PAS-MRI does not resolve the principal directions of dominating fibres it finds. These are to be found separately afterwards using a method to search for dominating fibre directions on the PAS sphere (Jansons et al., 2003). Fig. 3.3 shows an example where the PAS has been fitted to a DWI dataset obtained on a postmortem pig brain that has been used in Manuscript I.

The PASMRI algorithm is one of the newer model-free multi-fibre reconstruction methods that are based on a Fourier transformation followed by projection onto a sphere, or in terms of diffusion, onto a shell in q-space. The widely-cited q-ball algorithm by Tuch (2004) also belongs to this category, and an example is shown in Fig. 3.3.

Compared to the q-ball model, the PASMRI algorithm is far superior at resolving crossing fibre situations where dominating fibres have a low angular separation. The reason for this is that PAS distributions are much narrower than those of q-ball as seen in Fig. 3.3. This is important in two situations: 1) to differentiate crossing fibres with low angular inclination, and 2) when extracting the information about where the peaks are located in space. Alexander (2005) also compared q-ball and PASMRI and found, on simulated data, that PASMRI was more robust to low SNR than the q-ball model. However, compared to q-ball, PASMRI is extremely time-demanding due to the non-linear optimisation procedure.

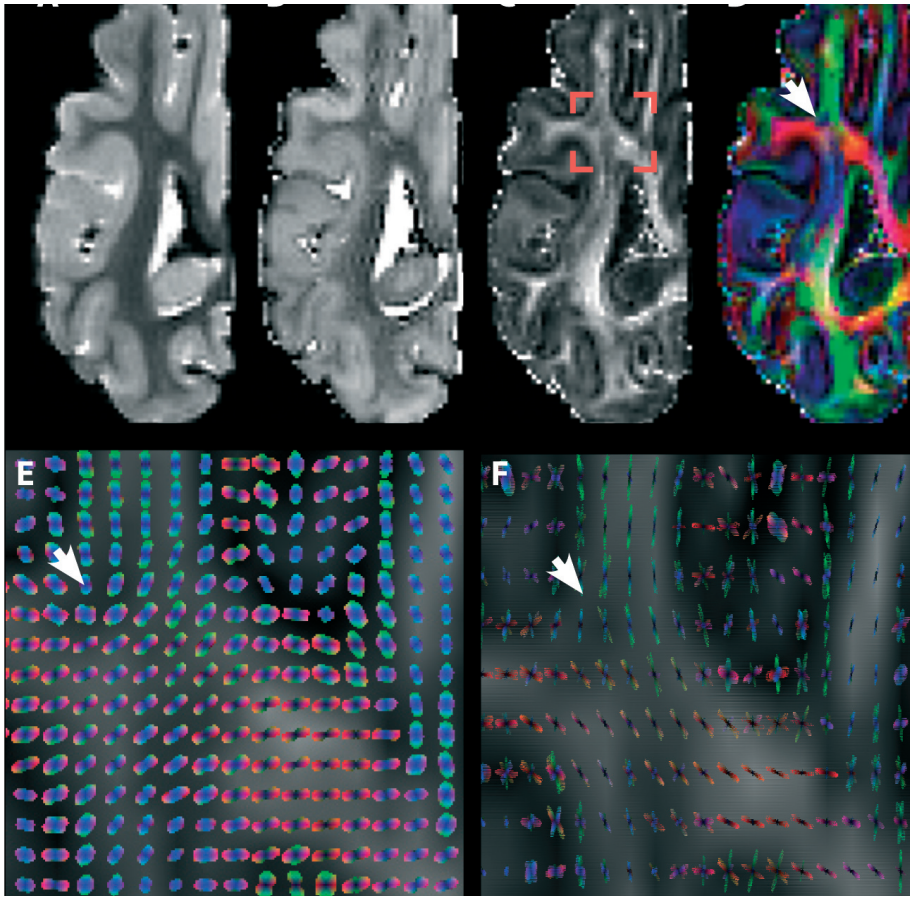

Fig. 3.3 *Three reconstruction models used to model the dominating fibre directions of a DWI dataset. The DWI dataset was obtained on a perfusion fixated pig brain using a DW-SE sequence based on the PSGE in Fig. 3.1 (δ = 27 ms; Δ = 33.5 ms; G = 56 mT/m; TE = 67.8 ms; TR = 2500 b = 4009 s/mm^2; t_d = 24.5 ms; voxel size=0.5 x 0.5 x 0.5 mm^3; NEX = 4, SNR ~ 20 see Manuscript I). The sampling scheme used contained 61 DW directions and was optimised as outlined in (Jansons and Alexander, 2003). The reconstructed fibre directions are RGB-colour coded; Red indicate a left-right direction, front-back direction is green and up-down direction is blue. (A) non-DW image used for normalisation (Eq. 3.5). Using the tensor model for reconstruction (Eq. 3.11) a MD-map (Eq. 3.14) and a FA-map (Eq. 3.15) can be calculated. In postmortem the MD in GM is 0.27 and 0.22 (x10^{-3} mm^2/s) in WM. (D) Principal direction of the dominating fibre direction (first eigenvector) can be colour coded and weighted by the FA map. Reconstruction using multi-fibre methods such as (E) the q-ball (Tuch, 2004) and (F) PASMRI (Jansons et al., 2003) visualise complex fibre regions with multiple fibres where the simple tensor model fail and indicate isotropic diffusion (arrow). In (E, F) are the FA-map in (C) used as background image. The MIPAV program was used to visualise (A - D) (McAuliffe et al., 2001). Implementation of reconstruction models used and 3D visualisation (E, F) are available in the Camino diffusion tool-kit (Cook et al., 2006).*

3.3 Tractography based on DWI

Tractography is the way to visualise neuronal fibre bundles using DWI. The advantage with this technique is that it is *non-invasive*, and can be applied in vivo as well as post-mortem. In the rest of this thesis "tractography" refers to tractography based on DWI to probe the neuroanatomical environment of brain tissue only and include all the processing stages needed (see next section).

In the following, the basic principles of the various fibre tracking stages, including both deterministic and probabilistic fibre tracking methods, are covered. However, the focus will be upon the most widely used fibre tracking methods, based on streamlining, which were also those used in Manuscript II.

3.3.1 Deterministic streamline fibre tracking

The principle of streamline fibre tracking is adopted from the physics within fluid flow. Streamlines are a family of curves that are instantaneously tangent to the velocity vector of the flow . Hence, in order to construct a streamline, one must simply follow the direction of flow from any given point. Moving a small distance along this direction and then finding out where the flow now points would draw out a streamline. This procedure is repeated until a certain stopping criteria is attained. In streamline fibre tracking, the direction of the fluid is synonymous with the vector field of local fibre directions. The point from where a streamline starts is known as a seed point (or region if more voxels are included), and the streamline propagates in steps of a given size until the end of the fibre bundle has been reached, as defined by a stopping criteria. Importantly, to make visualisations convincing and more alike a fibre bundle of densely packed axons, many streamlines are propagated from a lager same seed region including more seed points. However, such a visualisation only shows a pathway from *A -> B* which we infer to be a model/estimate of the true underlying fibre bundle. This kind of fibre tracking is *deterministic* and fibre bundles tracked and visualised have been demonstrated to be in accordance with some of the major fibre bundles visualised using histology. However, such 'accordance' does not provide any confidence that the fibre bundles are being tracked. An example of deterministic tractography is shown in Fig. 2.4.

In the early streamline fibre tracking methods, the vector field of local fibre directions was determined from the principal direction of the tensor model (single fibre) (Basser et al., 2000;Conturo et al., 1999;Mori et al., 1999). Today, the vector field of local fibre directions is expanded to also contain multiple-fibre directions utilized by multi-fibre reconstruction methods (see previous section) (Behrens et al., 2007;Berman et al., 2008;Parker et al., 2003a;Parker et al., 2005). The use of multi-fibre models is essential as long as the voxel size remains larger than a single neuronal fibre bundle, in order to model the PVE related to crossing fibre situations.

The propagation of a streamline through the discrete vector field basically utilizes two different approaches for achieving increased accuracy; non-interpolated and interpolated. Mori et al. (1999) introduced the fibre assignment by continuing tracking (FACT) method which is a non-interpolated approach. Here, tracking is initiated from the centre of a voxel and proceeds according to the vector direction. At the point where the track leaves the vox-

el and enters the next, its direction is changed to that of the neighbour. In contrast, Conture et al (1999) interpolated the DWI dataset before reconstruction in order to smooth out the vector field. A fixed step size was then used at which the direction of propagation for the next step was updated. As an alternative to interpolating before reconstruction, Basser et al. (2000) generated a continuous approximation of the already reconstructed vector field using a spline-based interpolation scheme and a fixed step size in the propagation of streamlines.

All of these methods require a means by which the streamlines can be terminated, either due to lack of sufficient information for progress to continue, or due to arrival at a suitable target. Probably due to its easier implementation, the former predicate is the most popular. Hence the stopping criteria for deterministic tractography are usually constraints upon a maximal intervoxel curvature of the streamline and encountering of low anisotropy.

3.3.2 Probabilistic streamlining fibre tracking

Probabilistic tractography methods produce, in contrast to the deterministic approach, a connection probability between two points *A* and *B* which is defined as the integral over all possible trajectories that connect the two points. Analytically, this integral is too complex to solve and instead a Monte Carlo (MC) sampling approach can be used (Parker et al., 2003b). In this approach, a limited number of all the possible trajectories between *A* and *B* is sampled by a given number of streamlines, and when these are averaged an approximation to the connection probability between the two points is achieved. Parker et al. (2003) named this approach the Probabilistic Index of Connectivity (PICo), and they called the respective possible trajectories "probabilistic streamlines" (Fig. 3.4). To generate probabilistic streamlines, a probability density function (PDF) describing the uncertainty of the fibre orientation *x* in each voxel is defined. Then, a probabilistic streamline starting from point *A* is created by randomly drawing a sample orientation *x* according to the local PDF and moving a small step along this direction. This procedure is repeated until a given stopping criteria is reached and the probabilistic streamline connects the starting point *A* to all points along its length. Behrens (2004) showed that as the step size tends toward zero, the probabilistic streamlines are samples from the integral of all the possible trajectories. In summary, to produce a PICo map of connections from point *A* to any point in the brain, a large number of probabilistic streamlines starting from point *A* are first generated, and then averaged. Today, most probabilistic tractography methods use the Monte Carlo sampling approach as described above to produce estimates of probabilistic connectivity maps, but there differ ways in which the local PDFs are produced (see next section).

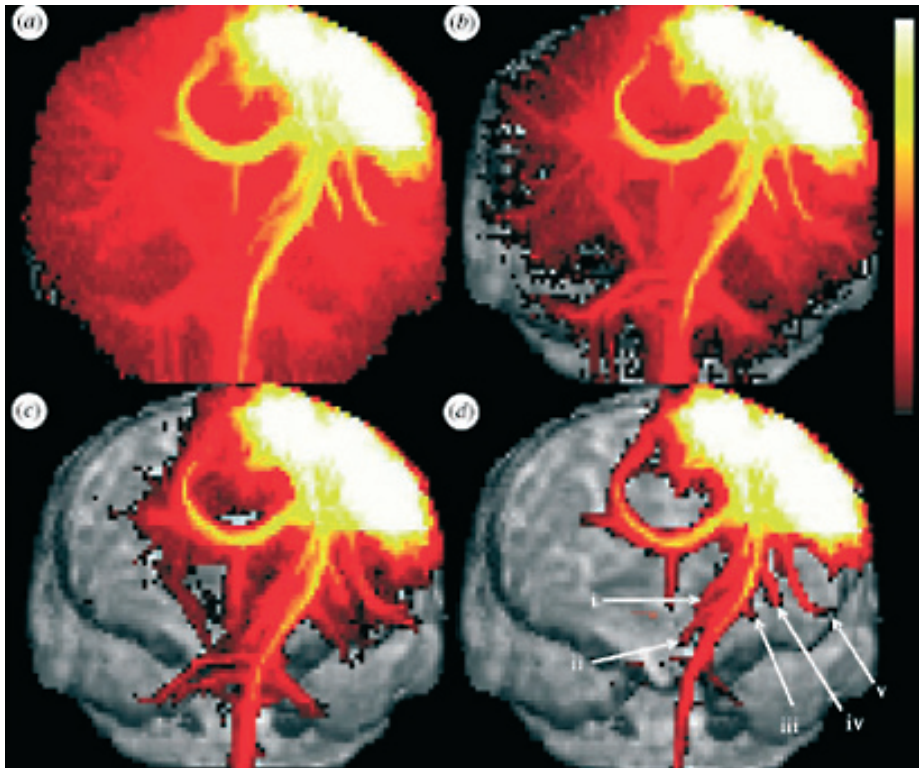

Fig. 3.4 *Probabilistic tractography. In sagittal view (on a glass brain) is shown a PICo map of all fibre projections emanating from a seed region placed in the left motor cortex of an in vivo human brain. Dominating fibre directions were reconstructed using the PASMRI multi-fibre method and the fibre tracking method uses the MC sampling approach, PICo. The connectivity, Ψ is shown at different thresholds. Logarithmic colour scale: (a) 0.0 ≤ Ψ ≤1.0, (b) 0.027 ≤ Ψ ≤ 1.0, (c) 0.074 ≤ Ψ ≤ 1.0 and (d) 0.20 ≤ Ψ ≤ 1.0. Major apparent connections identified include: (i) thalamus, (ii) subthalamic nucleus, (iii) globus pallidus, (iv) putamen and (v) Wernike's area. (From Parker and Alexander (2005)).*

Great care must be taken when interpreting such a PICo map because it is not a true connection probability, but simply a fraction of the total number of initial probabilistic streamlines entering a given voxel. Moreover, such maps include a distance-dependent bias where the probability of connection generally decreases with distance from the start point. This is due to the cumulative effect of the uncertainties in propagation direction (determined by local PDF) at each step in the streamline process. Therefore, as long as a distance-dependent bias is introduced into the probabilistic connectivity map, no statistical analysis as such can be made. However, probabilistic streamline tractography still provides important confidence measures of connections from which individual fibre bundles can be segmented and used as tract specific ROIs, e.g. in VBM analyses.

In probabilistic tractography there is no need to define stopping criteria in relation to low anisotropy, as is required for deterministic methods, because streamlines will disperse when entering areas with high uncertainty. Still, maximal curvature within a voxel must be set. Behrens et al (2003) selected 80 degrees, Parker et al (2003) 70 degrees and in Manuscript (II) a curvature of 80 degree was selected.

3.3.3 *Modelling uncertainty*

In contrast to streamlining tractography, where the vector field consists only of local fibre directions, the vector field used in probabilistic fibre tracking also includes a PDF describing the orientation uncertainty of the local fibre direction. Basically, it is the way in which these local PDFs, used for probabilistic fibre tracking, are generated that makes the difference between the probabilistic fibre tracking methods recently presented in the literature. Some of these different approaches are summarized here.

Probabilistic index of connectivity (PICo) by Parker (Parker et al., 2003b;Parker et al., 2003a;Parker et al., 2005) uses a general framework that allows the use of any PDF to describe the uncertainty in the fibre-orientation distribution in relation (as a function) to an anisotropic result obtained from the reconstruction model used. The PDF describing the uncertainty in local fibre orientation was chosen to be a symmetrical Gaussian probability density function distribution with a standard deviation expressed by an assumed relationship to the anisotropy. However, alternative and non-symmetrical PDFs can be used as well (Cook, 2006). When using the tensor model, a sigmoidal relationship was assumed between the distribution of local fibre directions and the anisotropy in order to generate the PDF (Parker et al., 2003b). Later, Parker introduced a multi-fibre model based on the mixture Gaussian probability density function model similar to Eq. 3.16, where the relationship between FA and the distribution of the local fibre orientation was described by bi-exponential functions (Parker et al., 2003a); one in a single fibre situation where a single tensor model was used, and one in a crossing fibre situation where a mixture of two-Gaussians was used. Using the algorithm by Alexander et al (2002) based on SH decomposition (as explained previously) voxels were classified into a single or a multi-fibre class. Recently Parker et al. (2005) also described a relationship between the distribution of the local fibre directions and the PAS directions in single-, two- and three-fibre situations as generated from synthetic DWI datasets, and then used this relationship to generate the PDF.

The use of relationships between the shape of the reconstruction model and the PDF enables the use of look-up tables (LUTs). Before being used in fibre tracking, the LUT has to be calibrated to the sequence parameters used and the SNR. However, once the LUT is created, the PDFs for the whole DWI dataset are created, and this also includes all DWI datasets which have the same sequence parameters and SNR. The limitation of using an LUT is that the PDF used in each voxel has no relationship to the actual DWI dataset other than via a general SNR, which is known not to be stationary within a brain volume. For example, a lowered SNR can be found in regions containing crossing fibres, such as in the centrum semiovale, when compared to other regions in WM.

Bayesian Estimation of Diffusion Parameters Obtained using Sampling Techniques (Bedpost) by Behrens et al. (2003) runs a Markov Chain Monte Carlo (MCMC) sampling scheme for fitting a parameterized model, and building up the PDF on the local fibre direction. Since MCMC is based upon a Bayesian optimisation approach, the PDF is termed a posterior distribution on the local fibre direction. Two parameterized models were suggested; a single tensor and a partial volume model (Behrens et al., 2003), and these were recently expanded to also handle multiple-fibre situations (Behrens et al., 2007).
The Bedpost method offers benefits over calibration-based methods, as used in the PICo method, in that the generated PDFs are a combination of actual data, such as the SNR

and MR scanner related parameters, and the reconstruction model. Voxel-wise MCMC is very time consuming, but easily lends itself to implementation on large computer systems with many parallel processors. Since MCMC builds up the posterior by sampling, a minimal number of samples are needed before generating stationary results of the posterior distribution on the local fibre direction - also known as the burn-in period of the MCMC sampling. Behrens et al. (2003) have empirically found that at least 5000 MCMC samples ensures a reasonable burn-in, however longer burn-ins maybe needed for noisy datasets.

The bootstrap method is a general non-parametric procedure for assessing statistical accuracy by randomly selecting individual measurements with replacement from a set of repeated measurements (Hastie et al., 2001). One such random selection is called a bootstrap sample and it provides a random estimate of the function to be statistically tested. Hence by generation of a large number of bootstrap samples, a measure of uncertainty is gained, forming the PDF directly.
One bootstrap sample is a new DWI dataset created by randomly selecting corresponding voxels from any one of the repeated DWI datasets that have been acquired. Jones (2003) fitted the tensor model to each of the bootstrap samples, the dispersion of local fibre directions was then calculated and "cones of uncertainty" showing the 95% confidence interval of fibre direction were visualised. The results showed, as expected, that in highly anisotropic regions, such as the corpus callosum, the uncertainty was low in contrast to regions containing crossing fibres. Later, instead of generating a PDF of local fibre orientation for probabilistic streamlining, both Jones et al. (2005) and Lazar et al. (2005) first applied deterministic streamlining to the vector field of fibre directions determined for each bootstrap sample and then averaged the streamlining. Notably, Jones et al. (2005) preferred to name their averaged map a "confidence map" (and not "probabilistic connectivity"), highlighting the fact that it reflected how confident a tract realisation was of not being a false-positive occurrence due to, for example, physiological noise.
One of the main strengths of the bootstrap approach is that it makes no a priori assumptions regarding the form of the PDF on fibre orientation and thus can account for variability due to non-Gaussian noise (e.g. physiological noise). However, for bootstrapping, the acquired DWI dataset has to be repeated several times (typically eight times) which increases the scanning time - an unacceptable cost for many patient groups. Also, the total amount of data produced in each bootstrap sample can be highly problematic to handle. Nevertheless, the bootstrap method is highly suitable as a tool for development and for testing the reproducibility of new tractography methods. Bootstrap methods that do not need repeated acquisitions of DWI datasets, such as residual bootstrapping, have recently been presented (Berman et al., 2008).

3.4 Sources of ambiguity

In practice, in vivo tractography consists of four processing stages, from the MR scanning through to visualization of the fibre pathways of the brain. Errors and problems introduced in each processing stage accumulate throughout leading to an increasing ambiguity that might be problematic at the later stages. The four processing stages are as follows: scanning, post-processing, reconstruction and fibre tracking.

3.4.1 The scanning stage

This is by far the most complicated of all the four processing stages. The risk of introducing bias and restricting the performance of the methods in the subsequent stages is high. However, by simply training the scanner operators to be quality-conscious, some of the problems normally introduced into the final DWI dataset can be minimised.

Head motion can introduce different amount of image distortions. Minor head motion is difficult to avoid and can be minimised retrospectively by coregistration in the post-processing stage. Severe head motion can introduce wave-shaped signal drop-out across the DW image. These artefacts typically occur when scanning elderly (dementia) subjects and young children who cannot lie still or are unable to go through a whole scanning session. For the latter, Cook et al. (2007) demonstrated a sampling scheme where the DWI directions are ordered in such a way that even if the scanning session is interrupted halfway, the partial DWI dataset thus obtained can still be used.

Eddy-currents come from the residual electrical currents induced in the coils by fast switching gradients, such as the strong diffusion weighted gradients or EPI imaging gradients. These residual electrical currents cause perturbations of the expected gradient field and can result in both an image-shift, image-scaling and image-shearing (Bammer et al., 2003;Le Bihan et al., 2006). A way to reduce the induction of eddy currents when fast DW-SE-EPI sequences are required is to use the twice-refocused spin echo sequence by Reese et al. (2003) which is available on most of today's clinical MR scanners. Compared to the traditional PGSE sequence (Fig. 3.1), two 180 degree refocusing pulses are used and at TE/2 the gradients are switched 180 degree to refocus the eddy currents induced in the first part of the sequence. The drawback is an increased TE which lowers the SNR. Alternatively, a conventional DWI SE sequence is also less sensitive to eddy-currents, but it is very slow and therefore not feasible for in vivo clinical settings where time is an issue. Finally, eddy-current artefacts related to image shift or shearing can, to some degree, also be reduced retrospectively in the post processing stage (Andersson et al., 2002;Koch et al., 2000;Maniega et al., 2007;Rohde et al., 2004).

A Ghosting artefact is an aliasing artefact where tissue outside the field-of-view (FOV) is folded back into the FOV and mixed with the tissue of interest and therefore a proper FOV have to be selected to avoid ghosting artefact.

Susceptibility artefacts are caused by the presence of a substance in the FOV with a significantly higher or lower magnetic susceptibility than the surrounding tissue, as for example air or bone, which at their interfaces introduce local inhomogeneity in the static magnetic field (B0). In the acquired images, susceptibility artefacts appear as bright and/or dark areas with spatial distortion of the surrounding anatomy. The fast DW-SE-EPI sequences used in clinical settings are sensitive to susceptibility artefacts, compared to the slow conventional DW-SE. The artefact can be reduced retrospectively, e.g. by unwarping methods in combination with a B0 map obtained just before DWI, or with phase maps (Andersson et al., 2001;Andersson et al., 2003;Voss et al., 2006).

Physiological noise is primarily related to motion caused by respiration and the cardiac pulsation cycle. Respiration introduces a slow movement of the whole head which can be

corrected retrospectively. In contrast, cardiac pulsation is highly problematic for fibre bundles placed in the neighbourhood of a large artery because of the changing arterial pressure. During systole, the arterial pressure is increased and the arteries expand, physically moving or compressing the neighbouring fibre bundles. Therefore, systolic pressure waves that appear during either focusing or refocusing of the spins might result in a signal drop out over a large region as the spins have moved erroneously over a long distance. Cardiac gating is one way to reduce the artefact with the cost of increased scanning times (Skare et al., 2001). The alternative is to manually identify and exclude DW volumes containing severe signal loss due to physiological noise or by outlier detection (Chang et al., 2005).

The sampling scheme, b-value and SNR are all factors which, if not correctly selected, can adversely affect the subsequent stages, e.g. reducing the contrast used for differentiating between single and crossing/fanning fibre populations.

3.4.2 The post-processing stage

The purpose of this stage is mainly to ensure that the data fulfils the assumptions required in the subsequent reconstruction stage, i.e. that no spatial or time dependencies exist across the series of DW images. The post-processing stage includes a pipeline of methods that retrospectively corrects the DWI dataset for the image artefacts described in the scanning stage. Even though many of the problems in the DWI dataset are minimised, sources of ambiguity are still introduced into the DWI dataset as residuals from the different methods, e.g. due to a sub-optimal coregistration aimed at minimising motion artefacts.

3.4.3 The reconstruction stage

The voxel-wise reconstruction stage determining fibre direction and composition to be used for fibre tracking methods. All the attempts to ensure the quality of the DWI dataset should pay off at this reconstruction stage. However, sources of ambiguity in the reconstruction stage are still present, as follows.

Model constraint errors occur if for example the tensor model is used to model non-Gaussian situations such as crossing/fanning fibre bundles. Even multi-fibre models are constrained to typically two fibre populations.

Suboptimal fit of the model to the DWI data occurs if a local instead of the global minima is reached in the optimisation procedure. A bias is then added to the reconstructed fibre directions and this will appear as an incorrect fibre direction or number of fibre directions modelled. Image artefacts, SNR (Alexander, 2005), sequence parameters and partial-volume-effect (PVE) are all factors that might negatively influence the optimisation procedure.
Imperfect models are mainly related to our limited knowledge of the true underlying function being modelled, i.e. the cellular structures.

3.4.4 The fibre tracking stage

In the final stage, fibre tracking methods allow us to visualise the fibre bundles in the brains emanating from a particular seed region. Sources of ambiguity identified in the fibre tracking stage are:

Model constraints such as curvature of the streamlines, the step-size and stopping criteria can result in visualisation of, for example, false-positive pathways or incorrect termination. Many of these problems are hard to prove due to the lack of validation material.

Path-length confidence is negatively dependent upon the length of the fibre projection followed, as the path-confidence decreases with increasing length of the fibre projection. This is a well-known problem in probabilistic streamlining tractography and it limits its use in inter- and intra-subject statistical analysis of the fibre projections found by tractography (Morris et al., 2006). The distance dependency is caused by the combination of using a Monte Carlo sampling framework for the streamlining with the sampling of fibre directions from a PDF representing the uncertainty of the local fibre direction (previous section).

Imperfect models are mainly related to our limited knowledge of the true underlying function to be modelled (the cellular structures). For example, currently fibre tracking methods rely only upon the discrete vector field of fibre directions and do not include any spatial information from other image modalities or anatomical atlases.

CHAPTER 4

Postmortem DWI datasets

For reliable tractography the different sources of ambiguity accumulated throughout the four processing steps, scanning, pre-processing, reconstruction and fibre tracking, have to be minimised. If we want to focus on validation of the reconstruction and fibre tracking methods, it would be optimal if the many sources of ambiguity from the scanning and pre-processing stages had a minimal impact on the variance of the downstream processing. This can be ensured by obtaining DWI datasets on postmortem brains. In this chapter, we first focus on how to ensure the fixation of postmortem tissue is as close to the in vivo situation as possible in order to be a valid model. Many environmental factors change in the transition from the in vivo to the *in vitr*o environment. Since MR is sensitive to such environmental changes, we then look into the optimisation of the sequence parameters for DWI and the stability of fixed brain tissue over time post mortem. To avoid short-term instabilities, the handling of the postmortem tissue before MR scanning must also to be taken into consideration if high image quality is to be achieved. The work in this chapter was performed on perfusion fixated animal brains and is the basis of the results Manuscript I.

4.1 Brain tissue post mortem

Fixated postmortem tissue has been used for centuries within the field of histology and allows investigation of the cells in the brain. We trust histology to visualise cells as they were in vivo and hence assume that the fixation procedure used succeeded in 'freezing' and preserving the cells in the conditions present before the start of the cell death process. In this section we will go through the process of cell death and select a fixation procedure which ensures that the tissue's behaviour is as close to that of the in vivo state as possible.

4.1.1 The dying cells

Following cardiac arrest the supply of oxygen to brain tissue is stopped - a situation which is referred as cerebral anoxia. After an extended period with cerebral anoxia, for example due to death, the brain tissue, and cells therein, begin a degeneration process due to the action of their own autogenous enzymes - a process called autolysis. The progression of autolysis is known to accelerate with increasing environmental temperature and also depends upon the chemical environment (e.g. pH) (Hukkanen et al., 1987;Srinivasan et al., 2002). Electron microscopic studies of excised human white matter samples have shown that, directly after excision (0hr), glial cells, axons, and myelin sheaths have been found well preserved. In contrast, after 25hrs at 25°C significant autolytic changes could be found in all components of WM, for example changes in glial axoplasm, disrupted myelin sheaths, and whorls of loosely packed myelin lamellae (Hukkanen et al., 1987).
Because DWI via the water molecules reflects restrictions of the cellular structures, the appearance of these ultrastructural abnormalities in the tissue due to autolysis is likely to be highly problematic. To avoid such a bias being introduced into the postmortem DWI dataset, the autolytic progression has to be stopped, preferably before its initiation. Chemi-

cal fixation stops the autolytic progression as well as the bacterial decomposition and stabilizes the cellular and tissue constituents (Srinivasan et al., 2002).

4.1.2 Fixation

Fixation of the tissue can be ensured either by the perfusion or the immersion fixation procedure.

The perfusion fixation procedure uses the cardiac blood flow typically in combination with a pump to flush the fixative through the entire body. The fixative is injected into the heart with the injection volume matching cardiac output and the procedure takes about 5 – 10 min. This has the advantages of preserving perfect morphology because the tissue does (in principle) not starts autolysis before fixation. Perfusion fixation can, for obvious ethical reasons, only be applied to animal models (deeply anesthetized).

Fixation by immersion is simply immersion of the fresh tissue (sample) within a volume of fixative at least 2/3rds greater than that of the tissue. The fixative then diffuses through the tissue, and hence tissue size and density, as well as the type of fixative, must be considered. How fast the fixative diffuses and fixates the tissue depends upon the fixative used and the temperature. At room temperature, the fixative 4% formalin about 1 mm/hr (Fox et al., 1985). Therefore, a relative rapid fixation of small and thin tissue samples is ensured, but larger samples such as whole brain volumes (especially human), risk an inhomogeneous fixation of the tissues close to the surface compared with those deep within the sample (Yong-Hing et al., 2005).

The degree to which the time delay from cardiac arrest to full immersion fixation impacts upon the quality of both the tissue and the MR image, and hence must be taken into consideration. Recently, D'Arceuil et al., (2007a) investigated the effect upon both anisotropy measures and tractography of different time delays until the completion of ex vivo brain tissue (mice) immersion fixation. They found clear evidence that the time delay post mortem affected the properties measured by DWI, thus lowering the reliability of tractography within a short time of about 24 hours. The timing of such a delay coincides with that of the appearance of severe ultrastructural abnormalities in the tissue, as reported by electron microscopic studies (Hukkanen et al., 1987). This time delay (determined by ethics) in combination with the limits of immersion fixation might be the reason that the results from DWI on postmortem human brain tissue are widely differing; from providing no signal (Pfefferbaum et al., 2004) to the opposite situation, detection of pathological changes (Englund et al., 2004;Schmierer et al., 2007), and visualisation of detailed anatomical structures, e.g. in parts of the hippocampus (Chakeres et al., 2005).

To minimise any autolytic-related bias being introduced into the MRI datasets, the perfusion fixation procedure and the fixative 4% formalin has been used throughout the thesis, with the setup as described in Manuscripts I, II and in Jelsing et al. 2006.

4.2 Postmortem MRI

By using perfusion fixation, the tissue does not (in principle) realise death. Biases introduced due to autolysis are therefore assumed negligible, and the fixated tissue is defined to be of high quality since it is assumed to be as close to the in vivo situation of the neuroanatomical environment as possible. Structurally, the neuroanatomy in vivo is assumed similar to that of the perfusion fixated. However, changes in the T1- and T2 relaxation times are observed, so in this section we first compare the in vivo and postmortem environments from the MR perspective. We then show how to optimise DWI acquisition for postmortem and how to handle postmortem tissue to obtain high quality DWI datasets.

4.2.1 In vivo versus postmortem MRI

Many of the in vivo sources that are known to add a bias to the DWI dataset are typically related to physiological noise and head motion; these do not exist when the DWI dataset is acquired postmortem. Moreover, the use of perfusion fixation minimises the neuroanatomical biases related to autolysis and thereby ensures high neuroanatomical similarity between the postmortem and the in vivo situation.

However, the MR properties of postmortem tissue differ widely from those of in vivo tissue as the T1 and T2 relaxation times change after fixation, declining gradually over a period of days postmortem (Thelwall et al., 2006;Tovi et al., 1992;Yong-Hing et al., 2005). Yong-Hing et al. 2005 included three human postmortem brains immersion fixated in 20% formaldehyde from 2 hrs post mortem to study and model the progression of fixation with MRI. Full fixation was achieved after about 770 hrs, and at that time point the T1 and T2 relaxation times had stabilised to (WM/GM) (500 ms/740 ms) and (40 ms/50 ms) and were decreased 40%/30% and 50%/38% when compared to the first measurement post mortem. An important observation on T1W MRI was that a light band from the surface of the brain gradually became thicker with time, displaying the apparent progression of formalin fixated tissue (also observed by Blamire et al. (1999)). Actually, in postmortem studies of the human brain using a T1w MRI, a GM/WM contrast reversal can be observed (Pfefferbaum et al., 2004). Tovi et al (1992) found this reversal to appear around the 4th day post mortem and it was likely caused by a greater decrease in T1 of GM than that of WM. In perfusion fixated pig brains we found a similar decrease in T1 and T2 relaxation times. A GM/WM contrast reversal was observed in the T1w MR scan of one animal that was not used in the Manuscript II; however, in contrast to the immersion fixated human brains, the contrast reversal first appeared after about 309 days (Fig. 4.1). Therefore, perfusion fixation seemingly ensures an immediate fixation of the tissue compared to immersion fixation. However, minor fixative-related changes in the tissue still seem to continue to appear on the longer time basis – probably caused by continuing chemical reactions in the cross-binding of the proteins caused by the use of the chemical fixative, formalin. Notably, these contrast reversals between GM/WM only appeared in the T1W images.

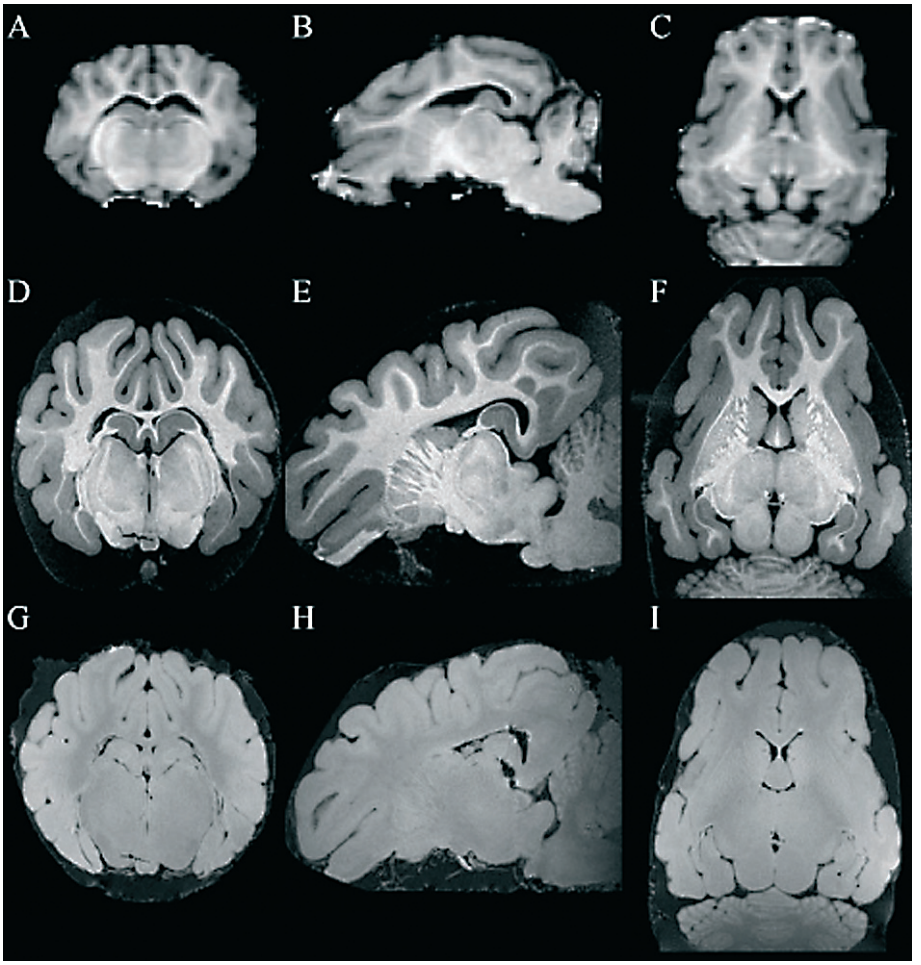

Fig. 4.1 *T1 relaxation time in perfusion fixated brain continues to change because of an immediate ongoing chemical reaction likely caused by the chemical fixative formalin used. T1W MPRAGE of a pig brain (A, B, C) in vivo with voxel size: 0.6x0.6x0.6 mm³, (D, E, F) 6 days post mortem and (G, H, I) 309 days post mortem with voxel size: 0.27x0.27x0.27mm³ (D - I is the same brain). After about 309 days the intensity between GM and WM was found interchanged indicating a change in the T1 relaxation time of GM and WM likely because of a continuous fixation process.*

Several studies have found that the diffusivity in fixated tissue compared to in vivo is decreased significantly. For example, Sun et al., (2005) found that the diffusivity in GM and WM was decreased 57% and 72%, results that were confirmed by D'Arceuil et al., (2007b) who found the diffusivity to be decreased 60% and 80%. Although the decreased diffusivity no statistical difference in anisotropy was found between in vivo and postmortem (D'Arceuil et al., 2007b; Guilfoyle et al., 2003; Sun et al., 2005). Since anisotropy does not change between in vivo and postmortem, a rotational invariant scaling factor of the diffusivities being common for all three principal directions must exist. Although assuming that perfusion fixated tissue is neuroanatomically similar to the in vivo situation, as indicated by anisotropy measures (e.g. the FA measure (Eq. 3.15)), the environmental conditions for the water molecules have changed. Firstly, a temperature difference between in vivo (37°C) and in the core of the MR scanner (18.5°C) exists, leading to a lowered activity of the molecules used to probe the environment, and thus a lower diffusivity (MD). In an unrestricted environment the diffusion coefficient of water molecules has been reported to decrease 2.4%/°C (Le Bihan, 1995). Secondly, the fixative, due to its cross-binding of the proteins, might induce an increased viscosity. An anecdotal indication of this is the observation that fixated tissue is not as flexible as non-fixated tissue. According to the Stoke-Einstein equation (Eq. 2.6), both lowered temperature and increased viscosity results in a lowered diffusion coefficient for postmortem when compared with in vivo. In WM, the neuronal environment is highly restricted and therefore the lowered temperature of postmortem may only have a minor influence on the observed lowered diffusion coefficient as compared with that of the fixation factor.

On the long-term basis (years), we have studied the stability of the diffusion coefficient across seven pig brains (Manuscript I) and find the diffusivity to be independent of time post mortem. Furthermore, no statistical difference between inter- and intra-brain variance was found. However, at the last time points 613 or 375 days post mortem for respectively P4 and P8, a decreased diffusivity (though very small) was apparent in both the WM and cerebral GM ROIs when compared to the prior time points, 166 or 42 days post mortem. Moreover, at this time point we experienced that more NEXs were needed to gain a similar SNR as that from younger postmortem brains and a weak change in the distribution of the PAS was observed after longer time post mortem (Fig. 4.2). Many different parameters impact on the SNR of the DWI image and we have as yet not performed experiments to thoroughly confirm the appearance of lowered SNR in elderly postmortem brains. Despite the difference in SNR, the fibre orientation in the DWI datasets seems to be independent of time post mortem.

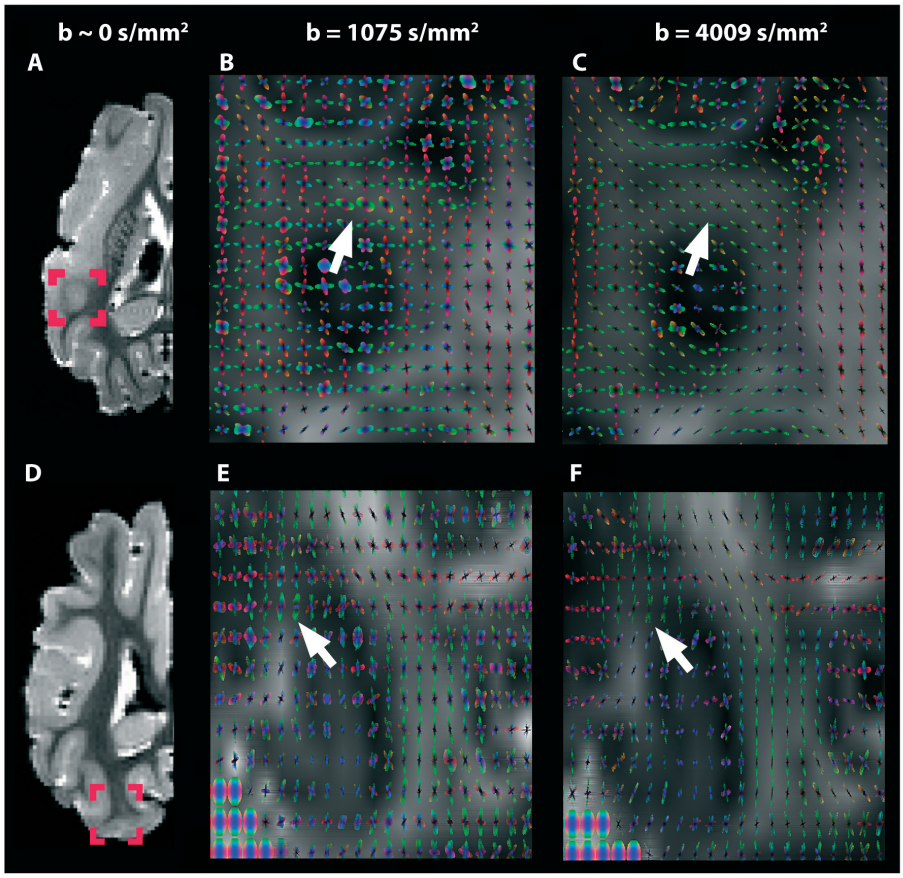

Fig. 4.2 *Continuous changes in the perfusion fixated tissue observed over longer time periods post mortem seem to influence the reconstruction at different b-values when e.g. the PASMRI reconstruction method is used. The same parameters have been used to obtain the DWI datasets and in one continuous scanning session a low b = 1075 s/mm² (B, E) and higher b-value b = 4009 s/mm² were obtained (from experiment in Manuscript I) (C, F) and voxel size was 0.5 x 0.5 x 0.5 mm³. (A, B) non-diffusion weighted DWI of the same pig brain but at different times post mortem: 166 days (NEX=2 for SNR > 21) (A - C) and 613 days post mortem (NEX=4 for SNR > 21) (D - F) (results from the latter have been used for in the selection of sequence parameters in manuscript I, fig. 3). Reconstruction using PASMRI is found in (B - C, E - F). Over a longer time period post mortem the PAS distribution that visualises the persistency of the dominating fibre directions are seemly a bit broader (B - C) than the reconstruction of the DWI dataset obtained after a longer time period post mortem (E - F). Importantly, loss of contrast in the reconstructed fibre directions and a lowered correlation with neighbouring voxels are seen in (B, E) at b = 1075 s/mm² when compared to a reconstruction where a higher b-value was used b = 4009 s/mm² (C, F) (arrows). On the longer time post mortem the contrast difference at too low b-value is less evident (E - F).*

4.2.2 *Optimising DWI sequence parameters*

Recently, Behrens et al. (2007) demonstrated that complex fibre projections such as the short association fibres could be robustly tracked by tractography, but only if reconstruction was based upon a multi-fibre model. This stresses the fact that the selection of the b-value used to obtain DWI datasets, in vivo as well as in vitro, should have maximal sensitivity to single as well as complex fibre situations within the tissue. Nevertheless, the selection of the optimal b-value in vivo has only been based upon simulations of the in vivo neuronal environment and then optimised with respect to an optimal ADC measure (Xing et al., 1997), a tensor determination (Jones et al., 1999) or single-fibre anisotropy (Alexander et al., 2005). A narrow range of b-values around 1000 s/mm^2 was found to be optimal. Despite a large percentage of the voxels in the brain consisting of complex fibre compositions, where a single fibre model such as the tensor model fails, these simulations assumed only single fibre situations. In two-fibre cases, Alexander et al. (2005) simulated that the b-value should be increased, e.g. for optimal anisotropy it should be within the range 1800 - 2400 s/mm^2.

To ensure the selection of an optimal b-value for use with postmortem tissue, an empirical approach was used (Manuscript III), for three reasons. First, simulations are, out of necessity, an oversimplification of the true neuroanatomical environment. Secondly, since reconstruction models are based upon different assumptions they have different sensitivities to the choice of scanning parameters. Thirdly, DWI datasets with various b-values are time consuming to obtain; however postmortem scanning lends itself easily to the acquisition of a series of DWI datasets with identical neuroanatomy. Such a dataset is ideal for testing and selection of an optimal b-value for reconstruction models.
In the setup, the postmortem tissue was considered as a black-box, with the b-value as input and the DWI dataset onto which three different reconstruction models were applied as the output. A range of b-values were tested (1018 – 15750 s/mm^2), producing a series of DWI datasets each with a different sensitivity to the neuroanatomical structure. Since all datasets were obtained in one continuous scanning session, no structural differences existed between datasets and a reliable direct comparison of the reconstructed fibre profiles was possible. The three reconstruction methods used were the single-tensor model (Eq. 3.11) (Basser et al. 1994), the multi-fibre model PASMRI (Eq. 3.18) (Jansons et al., 2003) and a voxel classification method based upon truncated spherical harmonics, as derived from Eq. 3.17 (Alexander et al., 2002).

Generally, for all three reconstruction methods, the b-values could be selected within a range of b-values between ~2000 and ~8000 s/mm^2. The upper bound mainly depends upon how sensitive the particular reconstruction method is to the noise floor. It is important to acknowledge that selecting too low a b-value sacrifices spatial coherence and CNR to detect e.g. crossing fibres within a voxel; this cannot be compensated for by increasing the SNR of the dataset (Fig. 4.2).
In this thesis, as a compromise between SNR, CNR and scanning time, a b-value of 4009 s/mm^2 was selected as being optimal for detection of single as well as complex fibre compositions and hence has been used for validation tractography (Manuscript II, Chapter 5).

4.2.3 Considerations when working with postmortem

Short-term instabilities – The DWI dataset consists of a series of DW-volumes that express the apparent molecular motion in different directions. For a valid reconstruction, there must be no time-dependent functions present during the scanning session. We define short-term instabilities to be an unwanted time dependency introduced into the DWI dataset.

When the brain has been taken out of the skull, there is no longer any protection or stabilization afforded to the brain tissue. Therefore, when preparing postmortem tissue for MR scanning, the physical handling and environmental temperature (heat conduction) should be taken into consideration in order to avoid short-term instabilities being introduced into the DWI dataset.

Using the setup described in Manuscript III, consistent short-term instabilities, displayed as unwanted intensity variation between slices, were noticeable in the first 15 hours of the scanning data. Two combined factors were subsequently identified as possible sources: heat conduction and mechanical changes. We identified mechanical process to be the sole contributor since no heat conduction was observed in either surrounding fluid or fluid inside the ventricles. Heat conduction relates to the time it takes the brain/coil assembly to stabilize to the temperature within the (middle of the) core of the magnet whilst acquiring DWI (Note that the heat conduction issue is not related to the environmental temperature difference between in vivo and in vitro tissue). The mechanical factor is adopted from mechanical physics, describing the recovery nature of a spring possessing a certain elastic constant after having an external force applied (Young, 1992). By analogy with postmortem tissue, the spring corresponds to the firmness of the brain tissue whilst the external forces refer to all the (physical) handling (slicing, shaking, squeezing etc.) during preparation of the tissue before placing it in the mechanically stable environment of the coil. Diffusion is highly sensitive to temperature changes, because the temperature determines how fast water molecules probe the microstructure environment, as previously described. Minor temperature variation is believed not to degrade the validity of DWI datasets, collected for use in tractography for example, since the probed environment and hence the directional information is consistent. However, for studies interpreting the microstructure of the tissue, then the heat conduction/temperature issue has to be considered. In contrast, mechanical instabilities introduce a spatial change in the microstructure, meaning that the tissue slowly deforms over time and hence the individual directional fibre orientations deform with it. The firmness of the brain tissue greatly impacts the time period of the mechanical instability factor. As an example, collecting DWI of fresh postmortem tissue, which is a jelly like substance, would incur a penalty of a considerably increased time period for the short term instabilities compared to that observed for perfusion fixated tissue. Mechanical factors also exist in in vivo DWI and are known as physiological noise covering factors such as pulsation artefacts (Skare et al., 2001). In contrast to in vivo where physiological noise is not straight forward to reduce, short term instabilities can be avoided by simply excluding DW-volumes obtained in the first time period of the scanning session. Alternatively, a constant mechanical stabilisation of the postmortem brain tissue, such as offered by a plastic box, might help to minimise the time period of the short term instabilities.

Air bubbles – These are difficult to identify and eliminate without damaging the postmortem tissue and are typically observed within the lateral ventricles and in between sulci (Fig. 4.3). The appearance of air bubbles is problematic because of susceptibility disparity at the interface with the tissue leading to severe image distortions (see previous chapter). The DWI datasets in this study were all collected using a conventional (2D) DW SE sequence with a long acquisition time compared to the fast DW-SE-EPI normally used in clinical MR scanners and which is less sensitive to susceptibility.

Blood vessels - Incoherent blood flow in vessels and arteries can be suppressed by using higher b-values and is therefore not considered as an important source of noise for in vivo DWI. In postmortem MRI, blood flow is absent. Instead the vessels contain water or a fixative, adding an isotropic signal component to the acquired DWI dataset. Because of this alteration to the PVE, DWI datasets acquired on postmortem brain tissue for use in tractography entail a risk of showing increased orientational uncertainty for fibres close to vessels or arteries. The degree of PVE is expected to vary according to the size of the vessels or arteries and the voxel size. For example, in the case of the pig brain DWI datasets used in Manuscripts III and VI, blood vessels were not visible in the MD maps (i.e. they were isotropic) but started to appear on the T1W images which had an eight times higher image resolution. In contrast to the pig brain, blood vessels were clearly visible in the MD map of the Vervet monkey brain (postmortem) (Fig. 4.3).

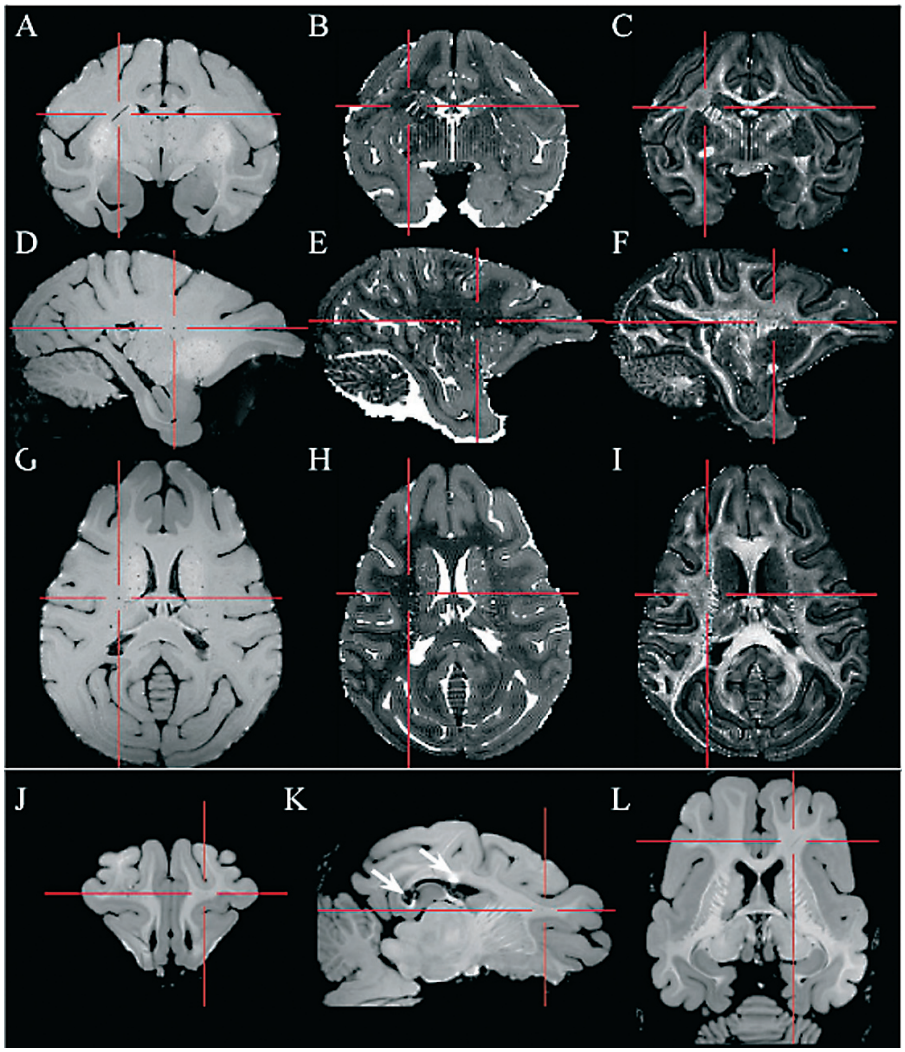

Fig. 4.3 *Demonstration of the possible vessel problem for tractography on DWI datasets acquired postmortem. Perfusion fixated Vervet monkey brain (A and I) and minipig brain (J and L). T1W MPRAGE with voxel size 0.27x0.27x0.27 mm³ of monkey brain (A, D, G) and pig brain (J, K, L). Mean diffusivity (MD) map (B, E, H) and FA maps (C, F, I) obtained on monkey brain with 61 DW directions and b=4009 s/mm²; 0.4x0.4x0.4 mm³. The Red Cross indicates in 3D (axial, coronal and sagittal view) a blood vessel in the monkey and the pig brain. In the monkey brain the blood vessels are clearly visible both in the high resolution MPRAGE as hypo-intense, in the MD maps as hyper-intense (isotropic diffusion) and in the FA maps as hypo-intense. In the pig brain, only few blood vessels can be found at the high resolution T1W image of the pig brain. Susceptibility artefact due to air bobble in the ventricles can be observed in the pig brain because fluid has been removed to increase SNR (K, arrow) (Manuscript I).*

4.3 Conclusion: Postmortem DWI datasets

Postmortem DWI is superior to in vivo for method testing purposes because most of the sources of ambiguity found in in vivo scanning, such as physiological noise, do not exist postmortem. Also, postmortem DWI datasets provide as highly a complex and realistic neuroanatomical environment as in vivo ones and are therefore suitable for validating the possibilities and limitations of tractography methods, and for studying the orientational organisation of cellular structures.

We have examined the process of cell death and found that within the first 12 hours a 'death factor' was not clearly visible by inspection of histology and did not influence on tractography. Nevertheless, changes do appear immediately after death as were indicated by a decreasing T1 and T2 relaxation when compared to in vivo. Two fixation processes were explained; fixation by immersion, and perfusion fixation. Perfusion fixation ensures an immediate fixation of the tissue and thus offers itself as a reasonable model of the in vivo situation. In this thesis, perfusion fixated brains were used for all postmortem scans.

The apparent diffusion coefficient was stable over longer time periods (years), and no significant inter- or intra-brain differences were found. However a weak tendency towards lowered diffusivity was found at the latest time points measured 613 days post mortem. An ongoing fixation process might be the explanation for this.

An empirical approach was used when selecting a b-value which ensured an optimal contrast for reconstructing fibre profiles. Results were interpreted from one single- and two multi-fibre reconstruction methods. Generally, for all methods, an optimal range of b-values was found in the range of ~2000 and ~8000 s/mm^2. As a compromise between SNR and CNR, a b-value of 4009 s/mm^2 was chosen as optimal and used in the following chapter for validating tractography.

We identified and visualised short-term instabilities in the tissue within the first ~15 hours scanning time. The subsequent artefact was related to the preparation procedure of the tissue before MR scanning. The artefacts can be avoided simply by excluding all DWI data obtained within the period susceptible to short-term instabilities. Additionally, air bubbles and (fixative-filled) blood vessels were identified as sources of, as yet unknown, factors which could affect tractography.

CHAPTER 5

Validation of Tractography

Tractography is a powerful method that is based upon DWI and that allows the non-invasive study of brain connectivity. Although probabilistic tractography currently holds great promise as a powerful connectivity-measurement tool, its accuracy and limitations remain to be evaluated. In particular, evidence of a strong correlation between the anatomical connectivity information provided by tractography methods and independent anatomical data is still lacking. Therefore, we considered it important to validate tractography against such an independent dataset. To exclude most sources of ambiguity which were unrelated to the reconstruction or the fibre tracking stages, the tractography was based upon the high quality postmortem DWI dataset as described in Chapter 4.

In this chapter we will focus upon the different underlying issues for validating tractography that were presented in Manuscript II. Firstly, the concept of independent anatomical data is defined. In order to derive a gold standard suitable for validation, we selected the use of invasive neuronal tract tracers. Principles, possibilities, and pitfalls when using such in vivo tracers are then discussed. When using invasive tracers, an experimental animal model must be chosen. Here we have used the Göttingen minipig (Lind et al., 2007) as an animal model and its use is discussed. Finally, concepts of direct and indirect validation are given, as well as the objective selection of seed regions for tractography, and how tractography is constrained to only include specific fibre projections.

5.1 Independent Anatomical Data

To *validate* a method is to "establish its validity, precision or truth using an authoritative basis". In relation to tractography, application of a particular method to a group of subjects cannot therefore classify as validation (Ciccarelli et al., 2003;Heiervang et al., 2006). Neither can repetition of experiments, nor comparison of results amongst different methods (Seunarine et al., 2007). These kinds of experiments underline the fact that the use of such measures, e.g. inter-subject correlation of a particular fibre tract, does not necessarily equate to a gold standard for the validity of tractography methodologies. Instead, they are likely to be merely an indication of the consistency by which the tractography method, in combination with the DWI dataset used, tracks fibres. The problem is the lack of a gold standard based upon an alternative method of representing the true underlying function which tractography attempts to model. Independent anatomical data is one such alternative source. Two different ways have been identified for collecting independent anatomical data to validate tractography: artificial methods, and committee methods, the latter being based upon the neuroanatomical environment.

5.1.1 Artificial validation methods

Independent anatomical data derived with artificial methods is the only gold standard upon which the ground truth, i.e. the information which is to be modelled via tractog-

raphy, can be explicitly defined. Such approaches include synthetic data and the use of phantoms. Generally, artificial validation methods are based on assumptions of the true neuroanatomical environment and typically only single and isolated cases of the neuroanatomical environment can be validated.

Synthetic data are typically based upon tensor-fields which either represent the piecewise reality situations that require validation, e.g. the kissing or crossing of two fibre bundles, or the impact on SNR in the dataset (Lazar et al., 2003;Leemans et al., 2005). Synthetic data are suitable for the initial validation of tractography methods during the development phase, but they lack complexity because the data is only based upon the tensor model.

A phantom basically includes a plastic/glass container with fluid surrounding the actual phantom of a WM fibre bundle, embodying the diffusivity of densely packed myelinated axons. Phantoms have been based on textiles such as polyester (Watanabe et al., 2006) and rayon fibres (Perrin et al., 2005), and hollow glass capillaries (Yanasak et al., 2006). Similar to synthetic data, datasets obtained from phantoms only represent piece wise reality situations where tractography can be validated, e.g. crossing fibre situations. However, in contrast to synthetic data, phantom-based DWI datasets are obtained on MR scanners and probe 'real' molecular diffusion.

5.1.2 The committee method

Independent anatomical data based on the 'committee' approach uses the consensus obtained from many different methods to derive a gold standard for a given problem. Then, in contrast to artificial validation methods that are based upon assumptions and an artificial environment, the committee method provides validation of tractography in the true neuroanatomical environment. Possible members of a committee afforded with the task of deriving a gold standard of fibre projections for validation of DWI tractography are:

Manual histological dissection of fibre bundles in postmortem brains; currently the only technique to precisely visualise major WM fibre bundles of the human brain (Burgel et al., 2006;Lawes et al., 2008). Because it is problematic to do manual dissection and to produce an in vivo DWI dataset on the same human brain (sufficiently high quality human postmortem DWI is yet not possible, see previous chapter), the manual dissection technique is not suitable as a committee member for direct validation of tractography methods, but only for indirect validation (direct versus indirect validation see section 5.4.1).

Invasive *in vivo* neuronal tract tracers allow identification of specific fibre projections in the brain. Due to the invasive nature of these tracers, the human brain is excluded for ethical reasons, and instead animal models such as the rat (Lin et al., 2001), monkey (Dauguet et al., 2007;Saleem et al., 2002;Schmahmann et al., 2006;Schmahmann et al., 2007) or the pig ((Dyrby et al., 2007) (Manuscript II)) brain are used. The benefit of animal models are that DWI datasets can be obtained in vivo (Dauguet et al., 2007) as well as in vitro (Dyrby et al., 2007 (Manuscript I), Schmahmann et al., 2007) (see Chapter 4) on the very same animal brain that received the invasive in vivo tracer. Then, a direction comparison of fibre projections revealed by the in vivo tracers and tractography can be realised. Moreover, different invasive in vivo tracers which are injected simultaneously do not interfere, even though the same fibre projections are targeted, and hence they can all be individual

members of a committee convened to derive a gold standard for tractography validation. As such, the invasive in vivo tracers were a natural choice for inclusion in the committee method approach used in this thesis. Fig. 5.1 illustrates the multiple injection site problem.

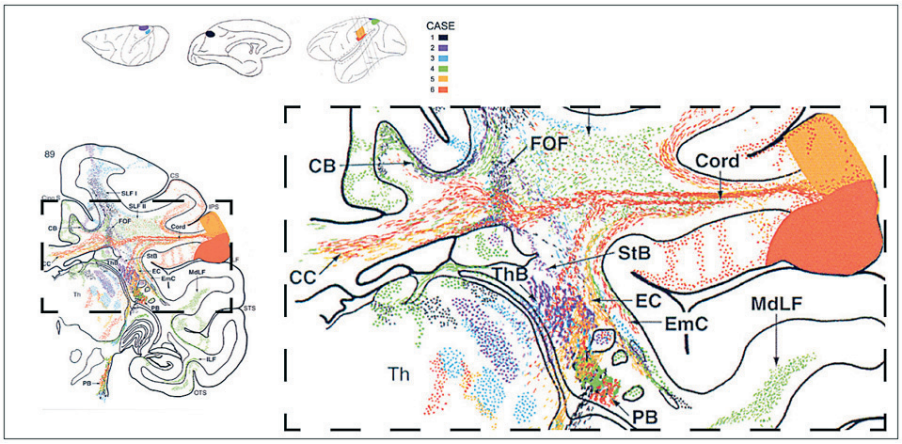

Figure 5.1 *Illustration of the multi-site injection problem if the same in vivo tracer is used. Schmamhann et al 2006 collected and colour coded on standard brain fibre projections that were found emanating from each of six different injection sites shown in the top of the figure and each animal received only a single injection. In coronal view (left) the fibre pathways from the different injection sites (solid colour) are highly complex (From Schmamhann et al 2006). Even the two very close injection sites (solid orange and red) show different projections as seen in the zoomed figure (right). Now, if the six injection sites were made in the same animal brain, all the fibre projections would have the same colour and thus indistinguishable and not optimally for validation of tractography methods.*

5.2 Invasive neuronal tract tracers

The invasive neuronal tract tracers utilise the axonal transportation system where proteins synthesised in the cell body are transported along the microtubules to/from the synaptic terminals. In principle, the proteins are packed into the membranes of transport vesicles and pulled along the microtubule by moveable bridges of kinesin, for anterograde transport, or dynein, for retrograde transport (Oztas E., 2003).

5.2.1 Retrograde and anterograde tracers

For retrograde tracing, material is applied to a fibre tract or terminal, incorporated into the axons by the process of endocytosis, and then carried back to the cell body. One of the first retrograde tracers used/discovered was the plant enzyme horseradish peroxidase (HRP) (for review, see (Mesulam, 1982)).

For anterograde tracing, the uptake mechanisms involve the cell body and/or its dendrites. In the cell body, the tracer material is synthesized into proteins and transported along the axonal transportation system to the cell's synaptic terminals (for review, see (Kobbert et al., 2000)). Examples of histological anterograde tracers include plant lectins conjugated to horseradish peroxidase (WGA-HRP) (Gerfen et al., 1984) and biotinylated dextran amines (BDA) (Glover et al., 1986) which also can be used as a retrograde tracer (e.g. see Fig. 1 in Manuscript II). These latter tracers are simple to use, easily detectable and preserved for several years in the tissue.

Recently, an MRI-detectable neuronal tract tracing method in living animals has been introduced that exploits the anterograde transport of manganese (Mn2+) (Pautler et al., 1998). Since manganese is paramagnetic it shortens the T1 relaxation constant which yields a positive contrast enhancement in T1W images (meMRI) and it has been used in a number of studies for tracking connectivity in vivo (Leergaard et al., 2003;Lin et al., 2001;Murayama et al., 2006;Pautler, 2004;Saleem et al., 2002).

In this thesis (Manuscript II), two anterograde tracers were used to derive a gold standard for direct validation of tractography; the histological tracer BDA and the MRI-detectable tracer manganese.

5.2.2 Limitations and possibilities

Although the two in vivo tracers BDA and manganese are used to derive a gold standard for validating tractography, each of them does have some limitations that must be considered.

The histological in vivo tracers are visualised by first cutting the brain into thin (coronal) slices (in 100 μm as was used in Manuscript II, but normally the slices are thinner), and hereafter the tracers are visualised histochemically. Whereas the BDA tracer permits easy identification of the injection site, the fibre pathways are generally not visualised and so small termination regions or termination regions not known beforehand incur a risk of not being discovered during the inspection of the histological slices under the microscope.

In contrast to the histological tracers, the manganese visualised on T1w MRI displays the injection site, the fibre pathways and the termination region. Moreover, meMRI provides a 3D whole brain volume. However, when compared to the histological tracers (provided in micrometer image resolution), the image resolution of MRI is quite low at only about 0.6x0.6x0.6 mm^3 (as used in this thesis). The image resolution is limited by the requirement of using a clinical MR scanner and by the scanning time. The low image resolution introduces PVE which can complicate interpretation in regions where fibre bundles both split and terminate, e.g. the internal capsule. In such regions the manganese signal can, at first glance, appear broad and dispersed (Manuscript II, Fig. 2 (H)).

In this thesis, the simultaneous cortical injection of two tracers, BDA and the manganese tracer, was performed. We used the manganese tracer, which exists in the same 3D image space as the postmortem DWI dataset postmortem, for a direct validation of tractography's pathways and terminations. The histological tracer, embedded in a different (2D) image space, was used to verify both the injection and termination sites found by the man-

ganese, and also to provide detailed anatomical knowledge. Only projections identified by both in vivo tracers were used to validate tractography. For example, the corticonigral projection from the motor cortex was not clearly identified (very noisy data) by either of the in vivo tracers and therefore not included in the validation of tractography.

The projection pattern from a single injection site can be highly complex and include ipsilateral and well as contralateral projections, terminating in cortical and well as in subcortical regions (Fig. 5.1, 5.3). A previously mentioned, the same tracer can only be injected once in the same brain, or alternatively different independent tracers must be used. Nevertheless, Dauguet et al. (2007) made two different cortical injections of the same anterograde in vivo tracer in the same monkey brain. Their histological tracer, WGA-HRP, is superior to BDA for visualising pathways. However, the projection pattern of their gold standard is mixed up by the two injections and so it cannot be established whether tractography correctly follows the gold standard or not.

5.3 Experimental animal models

Due to the invasive nature of the in vivo tracers used for validating tractography, an alternative brain model to the human brain has to be selected. The selection of a suitable animal model for the highly gyrated human brain depends to a great extent upon the experimental requirements, and especially upon the ethics issues.

Animal models have been widely used within the field of MRI and DWI and both the rat and monkey are commonly used as animal models. The rat brain has recently been used to validate tractography (Lin et al., 2001) and to study brain development reflected in DWI (Zhang et al., 2005). For example, the monkey brain has been used for in vivo validation of the q-ball reconstruction (Tuch et al., 2005) and for in vivo as well as in vitro tractography (D'Arceuil et al., 2007b;Dauguet et al., 2007;Schmahmann et al., 2007;Zhang et al., 2005).

5.3.1 The pig as an experimental animal model

The aim of validating tractography methods is generally to draw conclusions on the expected performance/confidence of the tractography method when applied to the human neuroanatomical environment. Therefore, the animal model to be used should be gyrated as the human brain and include the neuroanatomical complexity when fibre bundles (U-fibres, long association and the cord fibres) are entering/leaving a gyrus (Chapter 2). Secondly, the animal should fit into the MR scanner both alive for in vivo MRI to visualise the manganese in vivo tracer, and for collecting DWI datasets after perfusion fixation (as described in Chapter 4). Finally, ethical requirements must be meet.

As an animal brain model for the human brain in the case of fibre tracking, the rat brain is too simple in its neuroanatomy, e.g. it is not gyrated, low WM volume and it is small compared to the other possible animal models (Fig. 5.2). In contrast, both the monkey and pig brain are highly gyrated and are similar in size. As a primate, the homology of the monkey is closer to that of the human when compared to that of the pig. However, the pig brain's general anatomy is more similar to the primate brain than the brains of rodents (review Lind et al. 2007).

Ethical concerns when using the pig model are negligible compared to those for primates, likely due to the commercial use of pigs. Moreover, colonies of research monkeys have recently been closing in Denmark, Sweden and other European countries due to political/ethical and economic factors. The monkey as a living experimental model is therefore in principle not an option in Denmark.

The pig was used as an experimental animal model throughout this thesis (Manuscript I and II). For the validation study, the Göttingen minipig was used. The Göttingen minipig is an out breed race designed as an experimental animal model. In contrast to the mature landrace pig with a large body mass up till 300 kg, the Göttingen minipig has a final adult body weight of 35 - 55 kg. Because of the low body weight and size of the head, the minipig can fit into the human head coil and can easily be scanned in vivo in a clinical 3T Siemens TRIO MR scanner. Additionally, once perfusion fixated, the pig brain fits optimally into the coil used in the experimental 4.7T Varian Inova MR scanner. (The experimental MR scanner is used for postmortem MRI.)

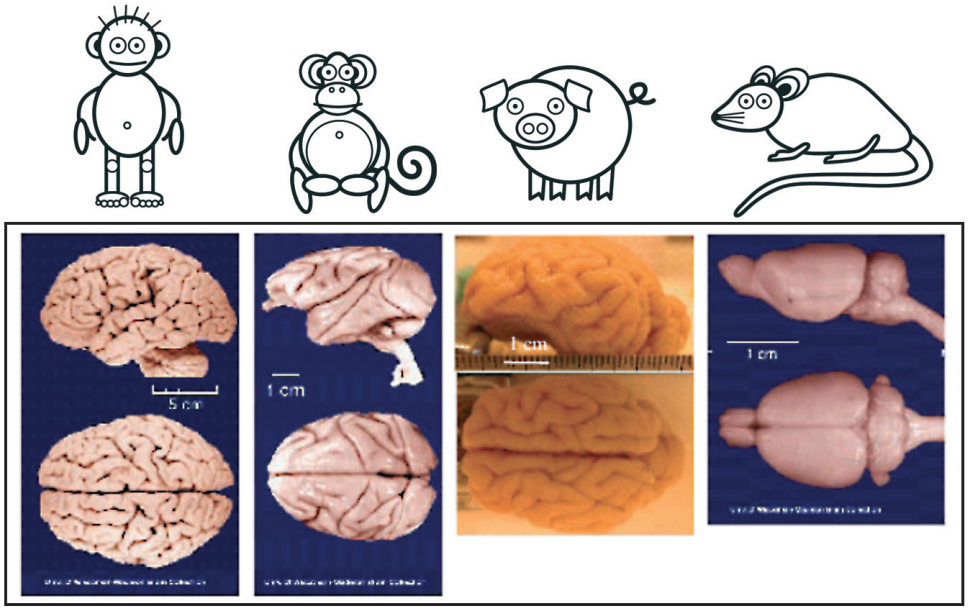

Fig. 5.2 *Different animal brain models to be used for validation of tractography (Monkey, Pig, rat and human) All animals have two hemispheres, but the cerebellum in the human and monkey is placed behind the cerebrum. Both the monkey and the pig brains are highly convolved as the human brain and the pig brain being the most convolved of the two animal models. In contrast, the monkey and human brain have relative more WM volume than the pig brain. The brain size of the pig brain and monkey is similar having a typical weight of 40g and 70g. The weight of the rat brain is 1g and the human brain (adult) weight about 1200g (The human, monkey and rat images are from Univ. of Wisconsin-Madison Brain Collection).*

5.3.2 Considerations when using the pig

Consistent sterotaxy in the pig brain is technically complicated by the presence of a well-developed frontal sinus in the adult pig skull and by the lack of stereotaxic atlases (e.g. (Felix et al., 1999)). The technical difficulties related to the frontal sinus can be solved by using younger mini pigs, such as the 3 month old pigs used in Manuscript II.
The cortical regions within the pig brain are placed differently as compared to primates. For example, the somatosensory cortex is placed frontally in the brain compared to a more medial placement observed in primates (see Manuscript II, Fig. 6 A-C). Generally, the different cortical regions in the pig brain have not yet been fully elucidated and so within the field there exists some naming confusion (Lind et al., 2007).

5.3.3 Extrapolating the animal model to the human brain

In order to draw comparative conclusions of the tractography validation from an animal brain model to what could be expected in the human brain, the image resolution of the animal DWI dataset has to be selected correctly. First we assume that the density of fibres in the animal and the human brain is the same. Both brains have a similar weight:weight and volume:volume ratio. The weight ratio between human and pig brain is (1200g / 40g) 30 and when selecting the image resolution of the pig brain to 0.5 x 0.5 x 0.5 mm^3, the corresponding image resolution in the human brain is 1.5 x 1.5 x 1.5mm^3. Typically, the image resolution of the in vivo human DWI datasets is in the range of cubic 2.5 to 2.1 mm^3. So comparing the image resolutions, PVE is expected to be less in the pig brain DWI dataset. However, in practice the anatomical resolution are alike because of the relatively lower WM volume in the pig brain compared to the human brain.

5.4 Validation setup

Results from validation are highly dependent upon the experimental setup used. In the following, the setup used in Manuscript II is reviewed. First we defined direct and indirect validation, and their uses. Then we considered how seed regions for tractography can be objectively defined. The waypoint regions used to constrain tractography are then introduced. Finally, comments on how waypoints regions have been used, and the on potential pitfalls are given.

In this section tractography is synonymous with probabilistic tractography and the tractography method used here is based on a multi-fibre reconstruction model and the PICo fibre tracking method (Parker et al., 2003a). All the methods used were included in the Camino diffusion tool-kit (Cook et al., 2006). The DWI datasets are obtained on perfusion fixated pig brains as described in Chapter 4.

5.4.1 Direct and indirect validation

The strongest kind of validation is direct validation. Here, the tractography method to be validated is applied to the same brain from which the independent anatomical dataset, which represents the gold standard, is collected. Direct validation allows quantification of

the spatial accuracy of the tractography results on a voxel-by-voxel basis, stating possible false-positive and false-negatives fibre projections, and importantly, identification of possible limitations of the tractography method.

Indirect validation is more weakly defined, and uses validation datasets which rely upon a fibre projection, such as function (e.g. fMRI) or cyto-architecture (e.g. Brodmann regions). Using indirect validation, it need not be a major concern to know the exact route that tractography traced a seed point to the target point, although an anatomical fibre projection in correspondence with the validation dataset should exist. These kind of independent anatomical data are a lot easier to obtain when compared to the direct validation methods, and are possible to apply on multiple-brain datasets to test whether the validity of one pathway generalises to another.

In the validation study (Manuscript II) both direct and indirect validation were used. Direct validation was realised since both tractography and in vivo tracers were applied to the same brain, and tractography was seeded in the same region as where the *in vivo* tracers were simultaneously injected.
Indirect validation was accomplished when tractography was used to reproduce the same pathways as visualised by the in vivo tracers, but in different brains e.g. Fig. 6 in Manuscript II.

5.4.2 Objective selection of seed region

For validation it is essential that the different tracer techniques are initiated in the same anatomical region otherwise there is no guarantee that the same fibre projections are visualised.

All animals received a simultaneous injection of the two in vivo tracers to ensure optimal conditions for visualisation of similar fibre projections. When simultaneously injected into three separate cortical regions, both tracers identified the same fibre projections. The injections sites were the somatosensory cortex (SC), the prefrontal cortex (PFC) and the motor cortex (MC). However, minor differences were found, e.g. those projections emanating from MC towards the caudate and from PFC toward the contralateral substantia nigra could not clearly be identified on BDA (Fig. 5.3).

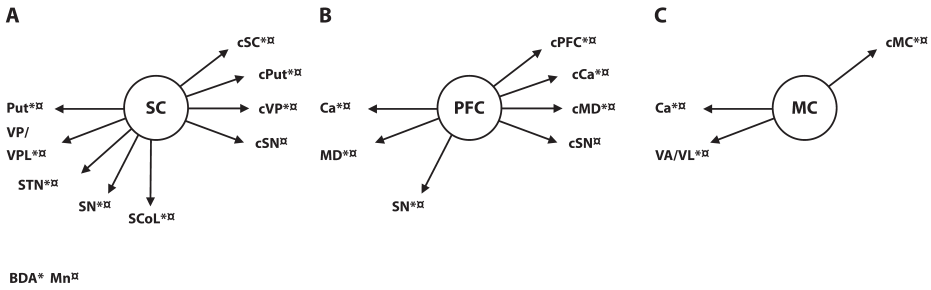

Fig. 5.3 *Schematic illustration of the projection sites that could be detected by the two in vivo tracers, BDA (*) and manganese, when injected into the right SC, the right PFC or the left MC. Contralateral projection sites are abbreviated with the prefix "c". (A) Injection into the SC revealed ipsilateral projections towards: putamen (Put), ventral posterior (VP) and ventral posterior lateral (VPL) nucleus of thalamus, subthalamic nuclei (STN), substantia nigra (SN) and the superior colliculus (SCol). Contralateral projections were observed towards: cSC, cPut, cVP and cSN. (B) Injection into the PFC revealed ipsilateral projections towards: caudate (Ca), medial dorsal (MD) nucleus of thalamus and SN, whereas the contralateral projections were observed towards: cPFC, cCa, cMD and cSN. (C) Injection into the MC revealed ipsilateral projections towards: Ca, and the ventral anterior (VA) and the ventral lateral (VL) nucleus of thalamus. The only contralateral projection observed was that towards the MC (From Dyrby et al. 2007, Manuscript II).*

In contrast to the in vivo tracers, a seed region from where tractography is initiated in the brain volume has to be hand-drawn. The seed region can be drawn subjectively (i.e. "we think that this area is a good seed region") or *objectively*, where specific anatomically-related knowledge has been identified and used as guidance in drawing the seed region.

We have used the objective approach. The seed region was drawn with the guidance of the visualised manganese tracer. The tracer was first thresholded in order to identify the injection site, and this was verified via the histological tracer (Fig. 5.4)

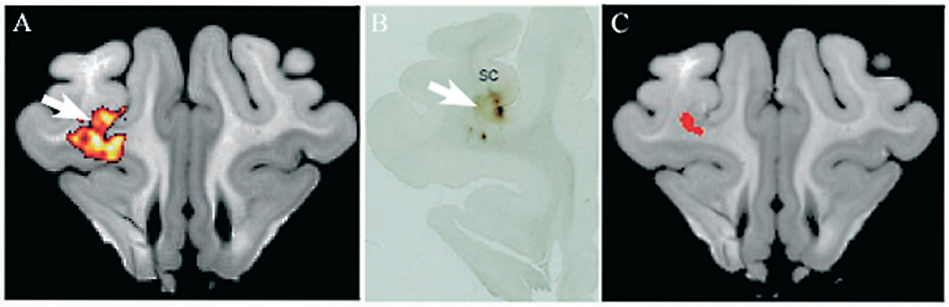

Fig. 5.4 *Objective selection of the seed region used to initiate tractography was found by identifying the injection site of the two in vivo tracers. Here manganese (A) and BDA (B) was injected into the SC. Injection site of the manganese tracer was found by thresholding (A) and used to guide the drawing of the seed regions for tractography (C). The injection site of the manganese tracer could be verified when compared to the injection site of the histological tracer BDA (B).*

Indeed, functionally-related regions, e.g. those visualised by fMRI, can also be used for objectively identifying seed regions. Segmentation of neurodegenerative diseases in WM, e.g. multiple sclerosis (Anbeek et al., 2004;Zijdenbos et al., 2002), or age-related WM changes (Manuscript III, Dyrby et al. 2008, (Admiraal-Behloul et al., 2005)), are interesting and promising new ways to objectively draw seed regions for visualising those fibre projections that are likely to be affected by such a disease.
One problem for the objective approaches is that a user-defined (i.e. subjective) threshold has to be selected. Different interpretation when selecting a threshold might introduce a bias if fibre projections across studies are compared.

5.4.3 Constraining tractography

In contrast to the in vivo tracers, tractography can be constrained in the sense that one or more fibre projections of interest emanating from a particular seed region can be individually identified amongst all the rest, simply by application of knowledge about the route it takes. Most tractography methods available in the literature allow the use of waypoints as the BedpostX/probtracX (Behrens et al., 2007) implementation in FDT (FMRIB Diffusion Toolbox) (FMRIB, 2007) and the PICo implementation in Camino diffusion tool-kit (Cook et al., 2006). Contour et al (1999) were the first to demonstrate the use of so-called "waypoint regions" and today they are used in the majority of studies. The tractography is constrained by drawing such a waypoint region within the brain volume. Streamlines that emanate from a seed region and do not enter the waypoint region are then excluded from the final fibre bundle.

We used waypoint regions to identify three major fibre projections: the contralateral corticocortical, corticothalamic and corticonigral tracts. These were then combined into a single (probabilistic) fibre projection for direct validation against the results of the in vivo tracers. Each of the fibre projections was also classified and coloured for an indirect validation of the reproducibility of the tractography method (Manuscript II, Fig. 6).

The utilization of waypoint regions also poses a risk of introducing a bias if a waypoint region includes only parts of the fibre bundle targeted (e.g. half the diameter of the actual fibre bundle to be investigated). Generally, waypoint regions should be broad, in contrast to the highly specific seed regions (Fig. 5.4).

5.5 Conclusion: Validation of Tractography

We have focused on the considerations and selections made to ensure an as reliable and yet practical and realistic validation of tractography as possible. The validation results of tractography are described in Manuscript II.

The possible datasets which can be used for validation tractography have been reviewed. As a gold standard, either artificial or independent anatomical data can be used. Though the ground truth is only really known when using artificial data, it lacks the complexity of the true neuronal environment. Using independent anatomical data preserves the neuronal complexity, but the ground truth is, in general, unknown. Therefore, the committee method was used to derive a gold standard and the members of the committee charged with deriving and visualising the fibre projections that were then used for validation were two invasive in vivo neuronal tracers; the histological tracer BDA, and the MRI detectable tracer manganese. Individually, the in vivo tracers have limitations in the context of validation, but when combined they provide a strong gold standard. For example, the pathways of the fibre projections are visualised in the same 3D image space as tractography, and as a result quantitative measures of spatial agreement can be obtained.

For ethical reasons, an experimental animal model must be used for these invasive tracers. Requirements for an animal brain model were listed and both the monkey and pig brain fulfilled these, both in the amount of gyration and the size. The Göttingen mini pig was selected as an experimental animal model. The DWI dataset used for tractography was obtained on perfusion-fixated pig brains (Chapter 4) and, in order to do a realistic comparison with the tractography applied to in vivo human brains, the image resolution was selected via use of the approximated weight ratio between the human and the animal brain.

In the study both direct and indirect validation were used. Direct validation is the most powerful type, validated against independent anatomical data collected on the same brain. In contrast, the same brains need not to be used for indirect validation, and this allows studying of, for example, the reproducibility of the tractography method.

The in vivo tracers were simultaneously injected to ensure optimal visualisation of the same projections. The seed region for tractography was objectively selected by thresholding the signal of the manganese tracer to identify the injection site. If not constrained tractography visualises a highly complex fibre projection pattern that will emanate from the seed region. Three large fibre projections identified by both the in vivo tracers were used in the validation study only. Waypoint regions were used to constrain tractography to the individual extraction of the three fibre projections that were used in the validation study.

CHAPTER 6

Conclusion and future perspectives

This thesis has been focused on perfusion-fixated animal brains that were proven to act as a complex model of the in vivo human brain, and were also used in the validation of DWI-based tractography (Chapter 4, Manuscript I and Chapter 5, Manuscript II). It was found that DWI on the postmortem brain was able to visualise orientationally-structured organisation, e.g. in the cerebral cortical layers, that is as yet impossible to visualise in the in vivo human brain. Combining histology and postmortem DWI might support and relate pathological changes found at the neuronal level with histology identified on postmortem MRI at the macroscopic level, and hence improve our understanding of the pathological structural changes observed non-invasively by clinical MRI of the in vivo human. Of course, the need for valid animal models of disease, for example Alzheimer disease, is a prerequisite in such cases.

Tractography allows the non-invasive study of fibre bundles in the brain and holds great potential in the investigation of neurodegenerative disease progression, of attacked fibre bundles and their corresponding termination regions in GM. We have validated probabilistic tractography in an in vitro environment against independent anatomical data. Here, two in vivo tracers were used within the framework concept of a committee method to derive a gold standard. Indeed, constrained tractography was found eminently applicable to the visualisation of the striatal fibre bundles and the cord fibres. However, three problem areas were identified: I) correct termination at subcortical GM, II) tracking through crossing fibre regions, e.g. centrum semiovale, and III) lack of path-length inconsistency for probabilistic streamlining. Basically, these are the limitations of current tractography methods, and are most probably related to the limited image resolution used in vivo (I & II), and too simple models (II & III). Increased image resolution will, of course, minimise some of the difficulties, e.g. in reconstructing crossing fibres and deciding when to terminate. However, the path-length inconsistency is a limitation of the basic idea of MC streamlining and its severity is likely related to how the fibre orientated pdf's are generated. Because of this path-inconsistency, tractography results as such can not be used in statistical measures, only as simple fibre bundle segmentation methods. The first future perspective of the current tractography methods must therefore be "solutions to the path-inconsistently". Next, "to find alternative quantitative measures to MD or tensor based anisotropy that describe the anatomical status along a fibre bundle", for example relative permeability or fibre density measures. Such measurements are likely to increase the sensitivity to the detection of pathological changes in fibre bundles. For realisation, HARDI acquisitions containing multiple DWI datasets obtained with different b-values are needed, as well as the design and implementation of new reconstruction methods.

Another part of the PhD project, but one not described in this thesis, was the automatic segmentation of age-related WM changes (WMC) in an elderly cohort of subjects (Manuscripts III and IV). It is believed that the WMC might be used as an early biological marker

for the development of dementia and therefore none of the subjects were diagnosed with dementia at baseline. The cohort was a part of the LADIS study, a clinical multi-centre study which included a total of 639 subjects at baseline, from 11 different centres within the EU. A 3 year follow-up MRI scanning, finished in 2007, has not yet been investigated. Semi-manually drawn WMC ROI's, to be used for validation of the automatic segmentation method, were available for all subjects. We optimised the generalizability of six artificial neural networks, each with a different set of input features combined from three structural MRI modalities (MPRAGE, FLAIR and T2W), and two kinds of spatial information (neighbouring voxel and relative distances). Although the FLAIR modality is highly sensitive to WMC, input features which contained at least all three MRI modalities showed the best generalisation abilities for WMC segmentation. The image quality of the FLAIR was found to vary across centres. Although a pipeline of pre-processing methods was used to standardise the image quality, only the MRIs of 362 subjects could be used in the study, typically due to degraded image quality. Obviously, segmentation results can only be as good as the image quality provided. It can be expected that in the future high-resolution 3D FLAIR and T2W MRI sequences (already available on some clinical MR scanners) will allow supervised segmentation methods to reach their full potential. Reduced agreement between the semi-manual and the network-segmented WMCs was found both at a low and a high WMC volume. Although it was assumed that the semi-manual WMC ROI was the gold standard, large variation between human raters has been reported. Therefore, a future perspective could be that human experts carefully inspected the network-segmented WMC in order to explain if the differences observed are in fact related to pathological changes or simply limitations of the segmentation method.

Potentially, automatic segmentation of WMC can be used to objectively constrain tractography and hence it might be possible to produce a connectivity map related to the progression of neurodegenerative diseases such as dementia.

References

Aboitiz, F., Scheibel, A.B., Fisher, R.S., Zaidel, E., 1992. Fiber composition of the human corpus callosum. Brain Res. 598, 143-153

Admiraal-Behloul, F., van den Heuvel, D.M., Olofsen, H., van Osch, M.J., van der, G.J., van Buchem, M.A., Reiber, J.H., 2005. Fully automatic segmentation of white matter hyperintensities in MR images of the elderly. Neuroimage. 28, 607-617

Alexander, D.C., 2005. Multiple-fiber reconstruction algorithms for diffusion MRI. Ann.N.Y.Acad.Sci. 1064, 113-133

Alexander, D.C., Barker, G.J., 2005. Optimal imaging parameters for fiber-orientation estimation in diffusion MRI. Neuroimage. 27, 357-367

Alexander, D.C., Barker, G.J., Arridge, S.R., 2002. Detection and modeling of non-Gaussian apparent diffusion coefficient profiles in human brain data. Magn Reson.Med. 48, 331-340

Anbeek, P., Vincken, K.L., van Osch, M.J., Bisschops, R.H., van der Grond, J., 2004. Probabilistic segmentation of white matter lesions in MR imaging. Neuroimage. 21, 1037-1044

Andersson, J.L., Hutton, C., Ashburner, J., Turner, R., Friston, K., 2001. Modeling geometric deformations in EPI time series. Neuroimage. 13, 903-919

Andersson, J.L., Skare, S., 2002. A model-based method for retrospective correction of geometric distortions in diffusion-weighted EPI. Neuroimage. 16, 177-199

Andersson, J.L., Skare, S., Ashburner, J., 2003. How to correct susceptibility distortions in spin-echo echo-planar images: application to diffusion tensor imaging. Neuroimage. 20, 870-888

Bammer, R., Markl, M., Barnett, A., Acar, B., Alley, M.T., Pelc, N.J., Glover, G.H., Moseley, M.E., 2003. Analysis and generalized correction of the effect of spatial gradient field distortions in diffusion-weighted imaging. Magn Reson.Med. 50, 560-569

Basser, P.J., Mattiello, J., LeBihan, D., 1994. Estimation of the effective self-diffusion tensor from the NMR spin echo. J Magn Reson.B 103, 247-254

Basser, P.J., Pajevic, S., Pierpaoli, C., Duda, J., Aldroubi, A., 2000. *In vivo* fiber tractography using DT-MRI data. Magn Reson.Med. 44, 625-632

Basser, P.J., Pierpaoli, C., 1998. A simplified method to measure the diffusion tensor from seven MR images. Magn Reson.Med. 39, 928-934

Bear,M.F., Connors,B.W., and Paradiso,M.A. (2001). Neuroscience exploring the brain. Lippincott Willimas & Wilkings).

Beaulieu, C., 2002. The basis of anisotropic water diffusion in the nervous system - a technical review. NMR Biomed. 15, 435-455

Behrens,T.E. MR Diffusion Tractography: Methods and Applications. 69-70. 2004. University of Oxford. Thesis

Behrens, T.E., Berg, H.J., Jbabdi, S., Rushworth, M.F., Woolrich, M.W., 2007. Probabilistic diffusion tractography with multiple fibre orientations: What can we gain? Neuroimage. 34, 144-155

Behrens, T.E., Woolrich, M.W., Jenkinson, M., Johansen-Berg, H., Nunes, R.G., Clare, S., Matthews, P.M., Brady, J.M., Smith, S.M., 2003. Characterization and propagation of uncertainty in diffusion-weighted MR imaging. Magn Reson.Med. 50, 1077-1088

Berman, J.I., Chung, S., Mukherjee, P., Hess, C.P., Han, E.T., Henry, R.G., 2008. Probabilistic streamline q-ball tractography using the residual bootstrap. Neuroimage. 39, 215-222

Bishop,C. (1995). Neural Networks for Pattern Recognition. Oxford University Press.

Blamire, A.M., Rowe, J.G., Styles, P., McDonald, B., 1999. Optimising imaging parameters for post mortem MR imaging of the human brain. Acta Radiol. 40, 593-597

Bonekamp, D., Nagae, L.M., Degaonkar, M., Matson, M., Abdalla, W.M., Barker, P.B., Mori, S., Horska, A., 2007. Diffusion tensor imaging in children and adolescents: reproducibility, hemispheric, and age-related differences. Neuroimage. 34, 733-742

Burgel, U., Amunts, K., Hoemke, L., Mohlberg, H., Gilsbach, J.M., Zilles, K., 2006. White matter fiber tracts of the human brain: three-dimensional mapping at microscopic resolution, topography and intersubject variability. Neuroimage. 29, 1092-1105

Callaghan,P.T. (1991). Principles of Nuclear Magnetic Resonance Microscopy. Oxford University Press), pp. 340.

Chakeres, D.W., Whitaker, C.D., Dashner, R.A., Scharre, D.W., Beversdorf, D.Q., Raychaudhury, A., Schmalbrock, P., 2005. High-resolution 8 Tesla imaging of the formalin-fixed normal human hippocampus. Clin.Anat 18, 88-91

Chang, L.C., Jones, D.K., Pierpaoli, C., 2005. RESTORE: robust estimation of tensors by outlier rejection. Magn Reson.Med. 53, 1088-1095

Ciccarelli, O., Parker, G.J., Toosy, A.T., Wheeler-Kingshott, C.A., Barker, G.J., Boulby, P.A., Miller, D.H., Thompson, A.J., 2003. From diffusion tractography to quantitative white matter tract measures: a reproducibility study. Neuroimage. 18, 348-359

Conturo, T.E., Lori, N.F., Cull, T.S., Akbudak, E., Snyder, A.Z., Shimony, J.S., McKinstry, R.C., Burton, H., Raichle, M.E., 1999. Tracking neuronal fiber pathways in the living human brain. Proc.Natl.Acad.Sci.U.S.A 96, 10422-10427

Cook,P.A. Modelling uncertainty in brain fibre orientation from diffusion-weighted magnetic resonance imaging. 2006. Department of computer Science, University College London. Thesis

Cook,P.A., Bai,Y., Nedjati-Gilani,Y., Seunarine,K.K., lexander,D.C. Camino: Open-Source Diffusion-MRI Reconstruction and Processing. 14th Scientific Meeting of the International Society for Magnetic Resonance in Medicine , 2759. 2006.

Cook, P.A., Symms, M., Boulby, P.A., Alexander, D.C., 2007. Optimal acquisition orders of diffusion-weighted MRI measurements. J Magn Reson.Imaging 25, 1051-1058

D'Arceuil, H., de Crespigny, A., 2007a. The effects of brain tissue decomposition on diffusion tensor imaging and tractography. Neuroimage. 36, 64-68

D'Arceuil, H.E., Westmoreland, S., de Crespigny, A.J., 2007b. An approach to high resolution diffusion tensor imaging in fixed primate brain. Neuroimage. 35, 553-565

Dauguet, J., Peled, S., Berezovskii, V., Delzescaux, T., Warfield, S.K., Born, R., Westin, C.F., 2007. Comparison of fiber tracts derived from in-vivo DTI tractography with 3D histological neural tract tracer reconstruction on a macaque brain. Neuroimage. 37, 530-538

Dyrby, T.B., Sogaard, L.V., Parker, G.J., Alexander, D.C., Lind, N.M., Baare, W.F., Hay-Schmidt, A., Eriksen, N., Pakkenberg, B., Paulson, O.B., Jelsing, J., 2007. Validation of in vitro probabilistic tractography. Neuroimage. 37, 1267-1277

Einstein, A., 1905. Über die von der molekularkinetischen Theorie der Wärme geforderte Bewegung von in ruhenden Flüssigkeiten suspendierten Teilchen. Annalen der Physik 17, 549-560

Englund, E., Sjobeck, M., Brockstedt, S., Latt, J., Larsson, E.M., 2004. Diffusion tensor MRI post mortem demonstrated cerebral white matter pathology. J Neurol. 251, 350-352

Felix, B., Leger, M.E., Albe-Fessard, D., Marcilloux, J.C., Rampin, O., Laplace, J.P., 1999. Stereotaxic atlas of the pig brain. Brain Res.Bull. 49, 1-137

FMRIB. FDT (FMRIB's Diffusion Toolbox). http://www.fmrib.ox.ac.uk/analysis/research/fdt/ . 2007.

Fox,C.H., Johnson,F.B., Whiting,J., Roller,P.P. Formaldehyde fixation. J Histochem Cytochem. 33[8], 845-853. 1985.

Frank, L.R., 2002. Characterization of anisotropy in high angular resolution diffusion-weighted MRI. Magn Reson.Med. 47, 1083-1099

Gerfen, C.R., Sawchenko, P.E., 1984. An anterograde neuroanatomical tracing method that shows the detailed morphology of neurons, their axons and terminals: immunohistochemical localization of an axonally transported plant lectin, Phaseolus vulgaris leucoagglutinin (PHA-L). Brain Res. 290, 219-238

Glover, J.C., Petursdottir, G., Jansen, J.K., 1986. Fluorescent dextran-amines used as axonal tracers in the nervous system of the chicken embryo. J Neurosci.Methods 18, 243-254

Graf, v.K., Schramm, U., 1984. Diameter of axons and thickness of myelin sheaths of the pyramidal tract fibres in the adult human medullary pyramid. Anat Anz. 157, 97-111

Guilfoyle, D.N., Helpern, J.A., Lim, K.O., 2003. Diffusion tensor imaging in fixed brain tissue at 7.0 T. NMR Biomed. 16, 77-81

Hastie,T., Tibshirani,R., and Friedman,J. (2001). The elements of statistical learning. Springer), chap. 7.

Heiervang, E., Behrens, T.E., Mackay, C.E., Robson, M.D., Johansen-Berg, H., 2006. Between session reproducibility and between subject variability of diffusion MR and tractography measures. Neuroimage. 33, 867-877

Hornak,J.P. The Basics of MRI. http://www.cis.rit.edu/htbooks/mri/ . 2007.

Hukkanen, V., Roytta, M., 1987. Autolytic changes of human white matter: an electron microscopic and electrophoretic study. Exp.Mol.Pathol. 46, 31-39

Jansons, K.M., Alexander, D.C., 2003. Persistent Angular Structure: new insights from diffusion magnetic resonance imaging data. Inverse Problems 19, 1031-1046

Jelsing, J., Hay-Schmidt, A., Dyrby, T., Hemmingsen, R., Uylings, H.B., Pakkenberg, B., 2006. The prefrontal cortex in the Gottingen minipig brain defined by neural projection criteria and cytoarchitecture. Brain Res.Bull. 70, 322-336

Jones, D.K., 2003. Determining and visualizing uncertainty in estimates of fiber orientation from diffusion tensor MRI. Magn Reson.Med. 49, 7-12

Jones, D.K., 2004. The effect of gradient sampling schemes on measures derived from diffusion tensor MRI: a Monte Carlo study. Magn Reson.Med. 51, 807-815

Jones, D.K., Horsfield, M.A., Simmons, A., 1999. Optimal strategies for measuring diffusion in anisotropic systems by magnetic resonance imaging. Magn Reson.Med. 42, 515-525

Jones, D.K., Pierpaoli, C., 2005. Confidence mapping in diffusion tensor magnetic resonance imaging tractography using a bootstrap approach. Magn Reson.Med. 53, 1143-1149

Kobbert, C., Apps, R., Bechmann, I., Lanciego, J.L., Mey, J., Thanos, S., 2000. Current concepts in neuroanatomical tracing. Prog.Neurobiol. 62, 327-351

Koch, M., Norris, D.G., 2000. An assessment of eddy current sensitivity and correction in single-shot diffusion-weighted imaging. Phys.Med.Biol. 45, 3821-3832

Lawes, I.N., Barrick, T.R., Murugam, V., Spierings, N., Evans, D.R., Song, M., Clark, C.A., 2008. Atlas-based segmentation of white matter tracts of the human brain using diffusion tensor tractography and comparison with classical dissection. Neuroimage. 39, 62-79

Lazar, M., Alexander, A.L., 2003. An error analysis of white matter tractography methods: synthetic diffusion tensor field simulations. Neuroimage. 20, 1140-1153

Lazar, M., Alexander, A.L., 2005. Bootstrap white matter tractography (BOOT-TRAC). Neuroimage. 24, 524-532

Le Bihan,D. (1995). Diffusion and Perfusion Magnetic Resonance Imaging. Raven Press), pp. 183-185.

Le Bihan, D., Poupon, C., Amadon, A., Lethimonnier, F., 2006. Artifacts and pitfalls in diffusion MRI. J.Magn Reson.Imaging 24, 478-488

Leemans, A., Sijbers, J., Verhoye, M., Van der Linden A., Van Dyck, D., 2005. Mathematical framework for simulating diffusion tensor MR neural fiber bundles. Magn Reson.Med. 53, 944-953

Leergaard, T.B., Bjaalie, J.G., Devor, A., Wald, L.L., Dale, A.M., 2003. *In vivo* tracing of major rat brain pathways using manganese-enhanced magnetic resonance imaging and three-dimensional digital atlasing. Neuroimage. 20, 1591-1600

Lin, C.P., Tseng, W.Y., Cheng, H.C., Chen, J.H., 2001. Validation of diffusion tensor magnetic resonance axonal fiber imaging with registered manganese-enhanced optic tracts. Neuroimage. 14, 1035-1047

Lind, N.M., Moustgaard, A., Jelsing, J., Vajta, G., Cumming, P., Hansen, A.K., 2007. The use of pigs in neuroscience: modeling brain disorders. Neurosci.Biobehav.Rev. 31, 728-751

Maniega, S.M., Bastin, M.E., Armitage, P.A., 2007. A quantitative comparison of two methods to correct eddy current-induced distortions in DT-MRI. Magn Reson.Imaging 25, 341-349

Marenco, S., Rawlings, R., Rohde, G.K., Barnett, A.S., Honea, R.A., Pierpaoli, C., Weinberger, D.R., 2006. Regional distribution of measurement error in diffusion tensor imaging. Psychiatry Res. 147, 69-78

McAuliffe, M. J., Lalonde, F. M, McGarry, D., Gandler, W., Csaky, K., Trus, B. L., 2001. Medical Image Processing, Analysis & Visualization in Clinical Research. 381-386

Mesulam,M.M. (1982). Principles of horseradish peroxidase neurochemistry and their applications for tracing neural pathways-axonal transport, enzyme histochemistry and light microscopic analysis. In: Mesulam MM (ed.). Tracing Neural Connections with Horseradish Peroxidase. IBRO Handbook Series: Methods in the Neurosciences. Wiley, New York), 1-551.

Mori,S. (2007). Introduction to Diffusion Tensor Imaging. Elsevier), Chap. 5.

Mori, S., Crain, B.J., Chacko, V.P., van Zijl, P.C., 1999. Three-dimensional tracking of axonal projections in the brain by magnetic resonance imaging. Ann.Neurol. 45, 265-269

Mori,S., Wakana,S., Nagae-Poetscher,L.M., and van Zijl,P.C. (2005). MRI Atlas of the Human White Matter. Elsevier B.V..

Morris,D.M., Embleton,K.V., Parker,G.J. Definition of Connection Significance Using Probabilistic Tractography. Proc.Intl.Soc.Magn.Reson.Med. 434. 2006.

Mukherjee, P., Miller, J.H., Shimony, J.S., Philip, J.V., Nehra, D., Snyder, A.Z., Conturo, T.E., Neil, J.J., McKinstry, R.C., 2002. Diffusion-tensor MR imaging of gray and white matter development during normal human brain maturation. AJNR Am J Neuroradiol. 23, 1445-1456

Murayama, Y., Weber, B., Saleem, K.S., Augath, M., Logothetis, N.K., 2006. Tracing neural circuits in vivo with Mn-enhanced MRI. Magn Reson.Imaging 24, 349-358

Oztas E., 2003. Neuronal Tracing. Neuroanatomy 2, 2-5

Pajevic, S., Pierpaoli, C., 1999. Color schemes to represent the orientation of anisotropic tissues from diffusion tensor data: application to white matter fiber tract mapping in the human brain. Magn Reson.Med. 42, 526-540

Papadakis, N.G., Xing, D., Houston, G.C., Smith, J.M., Smith, M.I., James, M.F., Parsons, A.A., Huang, C.L., Hall, L.D., Carpenter, T.A., 1999. A study of rotationally invariant and symmetric indices of diffusion anisotropy. Magn Reson.Imaging 17, 881-892

Parker, G.J., Alexander, D.C., 2003a. Probabilistic Monte Carlo based mapping of cerebral connections utilising whole-brain crossing fibre information. Lecture Notes in Computer Science 2732, 684-695

Parker, G.J., Alexander, D.C., 2005. Probabilistic anatomical connectivity derived from the microscopic persistent angular structure of cerebral tissue. Philos.Trans.R.Soc.Lond B Biol.Sci. 360, 893-902

Parker, G.J., Haroon, H.A., Wheeler-Kingshott, C.A., 2003b. A framework for a streamline-based probabilistic index of connectivity (PICo) using a structural interpretation of MRI diffusion measurements. J.Magn Reson.Imaging 18, 242-254

Pautler, R.G., 2004. In vivo, trans-synaptic tract-tracing utilizing manganese-enhanced magnetic resonance imaging (MEMRI). NMR Biomed. 17, 595-601

Pautler, R.G., Silva, A.C., Koretsky, A.P., 1998. In vivo neuronal tract tracing using manganese-enhanced magnetic resonance imaging. Magn Reson.Med. 40, 740-748

Perrin, M., Poupon, C., Rieul, B., Leroux, P., Constantinesco, A., Mangin, J.F., LeBihan, D., 2005. Validation of q-ball imaging with a diffusion fibre-crossing phantom on a clinical scanner. Philos.Trans.R.Soc.Lond B Biol.Sci. 360, 881-891

Pfefferbaum, A., Sullivan, E.V., Adalsteinsson, E., Garrick, T., Harper, C., 2004. Postmortem MR imaging of formalin-fixed human brain. Neuroimage. 21, 1585-1595

Pierpaoli, C., Jezzard, P., Basser, P.J., Barnett, A., Di Chiro, G., 1996. Diffusion tensor MR imaging of the human brain. Radiology 201, 637-648

Reese, T.G., Heid, O., Weisskoff, R.M., Wedeen, V.J., 2003. Reduction of eddy-current-induced distortion in diffusion MRI using a twice-refocused spin echo. Magn Reson.Med. 49, 177-182

Rohde, G.K., Barnett, A.S., Basser, P.J., Marenco, S., Pierpaoli, C., 2004. Comprehensive approach for correction of motion and distortion in diffusion-weighted MRI. Magn Reson. Med. 51, 103-114

Saleem, K.S., Pauls, J.M., Augath, M., Trinath, T., Prause, B.A., Hashikawa, T., Logothetis, N.K., 2002. Magnetic resonance imaging of neuronal connections in the macaque monkey. Neuron 34, 685-700

Schmahmann,J.D. and Pandy,D.N. (2006). Fiber pathways of the brain.

Schmahmann, J.D., Pandya, D.N., Wang, R., Dai, G., D'Arceuil, H.E., de Crespigny, A.J., Wedeen, V.J., 2007. Association fibre pathways of the brain: parallel observations from diffusion spectrum imaging and autoradiography. Brain 130, 630-653

Schmierer, K., Wheeler-Kingshott, C.A., Boulby, P.A., Scaravilli, F., Altmann, D.R., Barker, G.J., Tofts, P.S., Miller, D.H., 2007. Diffusion tensor imaging of post mortem multiple sclerosis brain. Neuroimage. 35, 467-477

Seunarine,K.K., Cook,P.A., Hall,M.G., Embleton,K., Parker,G.J., Alexander,D.C. Exploiting peak anisotropy for tracking through fanning structures. Proc.Intl.Soc.Magn.Reson.Med. 2007.

Shimony, J.S., McKinstry, R.C., Akbudak, E., Aronovitz, J.A., Snyder, A.Z., Lori, N.F., Cull, T.S., Conturo, T.E., 1999. Quantitative diffusion-tensor anisotropy brain MR imaging: normative human data and anatomic analysis. Radiology 212, 770-784

Sidaros, A., Engberg, A.W., Sidaros, K., Liptrot, M.G., Herning, M., Petersen, P., Paulson, O.B., Jernigan, T.L., Rostrup, E., 2008. Diffusion tensor imaging during recovery from severe traumatic brain injury and relation to clinical outcome: a longitudinal study. Brain 131, 559-572

Skare, S., Andersson, J.L., 2001. On the effects of gating in diffusion imaging of the brain using single shot EPI. Magn Reson.Imaging 19, 1125-1128

Skare, S., Hedehus, M., Moseley, M.E., Li, T.Q., 2000. Condition number as a measure of noise performance of diffusion tensor data acquisition schemes with MRI. J Magn Reson. 147, 340-352

Srinivasan, M., Sedmak, D., Jewell, S., 2002. Effect of fixatives and tissue processing on the content and integrity of nucleic acids. Am J Pathol. 161, 1961-1971

Stejskal, E.O., Tanner, J.E., 1965. Spin Diffusion Measurements: Spin Echoes in the Presence of a Time-Dependent Field Gradient. J.Chem.Phys. 42, 288

Sun, S.W., Neil, J.J., Liang, H.F., He, Y.Y., Schmidt, R.E., Hsu, C.Y., Song, S.K., 2005. Formalin fixation alters water diffusion coefficient magnitude but not anisotropy in infarcted brain. Magn Reson.Med. 53, 1447-1451

Thelwall, P.E., Shepherd, T.M., Stanisz, G.J., Blackband, S.J., 2006. Effects of temperature and aldehyde fixation on tissue water diffusion properties, studied in an erythrocyte ghost tissue model. Magn Reson.Med. 56, 282-289

Tovi, M., Ericsson, A., 1992. Measurements of T1 and T2 over time in formalin-fixed human whole-brain specimens. Acta Radiol. 33, 400-404

Tuch, D.S., 2004. Q-ball imaging. Magn Reson.Med. 52, 1358-1372

Tuch, D.S., Reese, T.G., Wiegell, M.R., Makris, N., Belliveau, J.W., Wedeen, V.J., 2002. High angular resolution diffusion imaging reveals intravoxel white matter fiber heterogeneity. Magn Reson.Med. 48, 577-582

Tuch, D.S., Wisco, J.J., Khachaturian, M.H., Ekstrom, L.B., Kotter, R., Vanduffel, W., 2005. Q-ball imaging of macaque white matter architecture. Philos.Trans.R.Soc.Lond B Biol.Sci. 360, 869-879

Voss, H.U., Watts, R., Ulug, A.M., Ballon, D., 2006. Fiber tracking in the cervical spine and inferior brain regions with reversed gradient diffusion tensor imaging. Magn Reson.Imaging 24, 231-239

Watanabe, M., Aoki, S., Masutani, Y., Abe, O., Hayashi, N., Masumoto, T., Mori, H., Kabasawa, H., Ohtomo, K., 2006. Flexible ex vivo phantoms for validation of diffusion tensor tractography on a clinical scanner. Radiat.Med. 24, 605-609

Westbrook,C., Roth,C.K., and Talbot,J. (2005). MRI in pratice. Blackwell Publiching).

Xing, D., Papadakis, N.G., Huang, C.L., Lee, V.M., Carpenter, T.A., Hall, L.D., 1997. Optimised diffusion-weighting for measurement of apparent diffusion coefficient (ADC) in human brain. Magn Reson.Imaging 15, 771-784

Yanasak, N., Allison, J., 2006. Use of capillaries in the construction of an MRI phantom for the assessment of diffusion tensor imaging: demonstration of performance. Magn Reson. Imaging 24, 1349-1361

Yong-Hing, C.J., Obenaus, A., Stryker, R., Tong, K., Sarty, G.E., 2005. Magnetic resonance imaging and mathematical modeling of progressive formalin fixation of the human brain. Magn Reson.Med. 54, 324-332

Young,H.D. (1992). University Physics. Addison-Wesley Publishing Company.

Zhang, J., Miller, M.I., Plachez, C., Richards, L.J., Yarowsky, P., van Zijl, P., Mori, S., 2005. Mapping postnatal mouse brain development with diffusion tensor microimaging. Neuroimage. 26, 1042-1051

Zijdenbos, A.P., Forghani, R., Evans, A.C., 2002. Automatic „pipeline“ analysis of 3-D MRI data for clinical trials: application to multiple sclerosis. IEEE Transaction in Medical Imaging 21, 1280-1291

Appendix

Magnetic Resonance Imaging

In the following is a brief introduction to the basic principle of MRI given. For additional introduction it can be recommended to read (Westbrook et al., 2005) or visit the illustrative homepage by (Hornak, 2007).

MRI is based on the principles of nuclear magnetic resonance, which is a spectroscopic technique used to obtain information about the chemical and physical properties of molecules. As such, MRI started out as a so-called tomographic imaging technique - a method for obtaining pictures of the interior of the body. Today, MRI has advanced far beyond this and now represents a battery of different approaches that can measure the structure, function, connectivity, and chemistry of any part of the body. MRI is based on the absorption and emission of energy in the radio frequency range of the electromagnetic spectrum. The human body is mostly made of fat and water - body tissues that have many hydrogen atoms. As such, the human body consists of about 65% hydrogen atoms. These hydrogen nuclei form the very basis for the signal in MRI.

In a magnetic field such as the MR scanner, the magnetic orientation of hydrogen proton is aligned to the magnetic field and spins around this orientation (see Illustration 1b and 1c), also called the Larmor frequency. If a brief electromagnetic (radio-frequency) pulse is applied, it temporarily distorts the proton spin (Illustration 1d). When the radiofrequency pulse ends, the spins return to equilibrium, a process called relaxation (Illustration 1e). The relaxation can be described with two time constants: Time-1 and Time-2. The regrowth of the magnetization along the magnetic field is termed longitudinal relaxation, and the time in milliseconds required for a certain percentage of the tissue nuclei to realign is termed "Time 1" or T1. Both relaxation processes follow an exponential time course. When returning to equilibrium, radio waves at the Larmor frequency are emitted from the tissue and sampled by a receiver. This is the basis of so-called T1-weighted imaging, which produces the most well-known structural images in MRI such as MPRAGE. T2-weighted imaging relies upon local dephasing of spins following the application of a transverse energy pulse; this transverse relaxation time is termed "Time 2" or T2. The T1 and T2 constants provide the basis for most medical imaging. In different parts of the body, such as the brain, different tissues alter the speed in which T1 and T2 relaxation occurs. The three most typical tissues of the brain are grey matter (GM), white matter (WM) and cerebrospinal fluid (CSF). The influence of these tissues produces different signal intensities (contrast) that makes it easier to distinguish between them. By varying different parameters during scanning, such as the rate and amplitude of the radiofrequency pulse, or the time from excitation to recording, it is possible to highlight different properties of the tissues and their differences.

Acquisition of an MR image requires spatial encoding in three dimensions. To obtain slice selection, a radiofrequency pulse with a narrow frequency range is applied in the presence of a spatial magnetic field gradient along the slice direction. Spatial encoding in the read-

out direction is obtained by applying a field gradient across the excited space, and spatial encoding in the second in-plane dimension is created by applying a gradient in the phase-encoding direction before each readout line. The reconstruction of images then occurs through Fourier-transformation of the raw data.

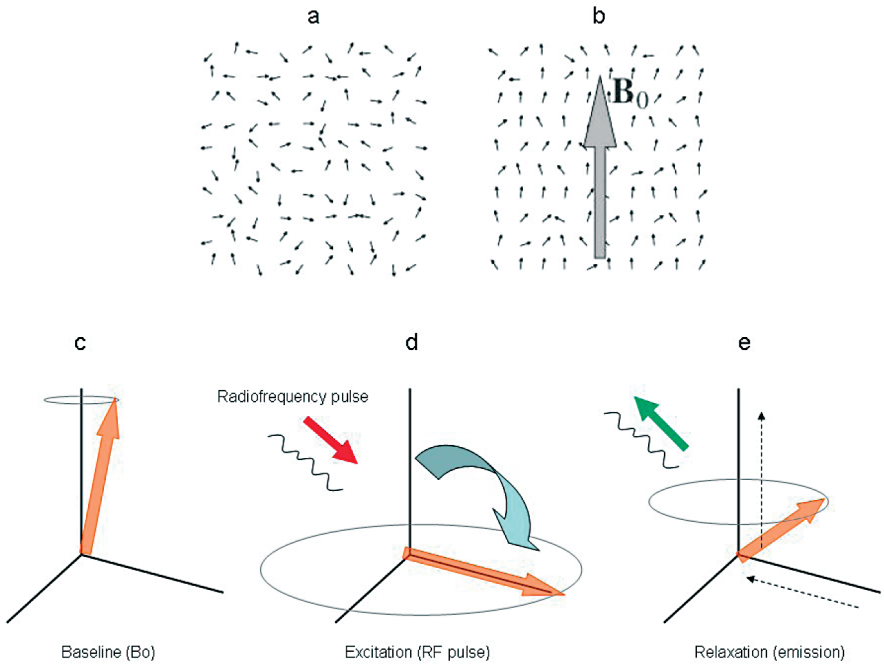

Illustration A.1: *The signal that makes up the MRI. Outside the scanner the atoms are oriented at random in the brain (a). When a subject is put into the scanner, the spins align to the magnetic field of the scanner (Bo). However, the alignment is not perfect, since neighbouring spins influence each other (b). At such baseline, the spins circles along the y axis (vertical axis in figure), i.e. the Bo field (c). When a radiofrequency (RF) pulse is applied the spin is influenced, and rotated down (d). This is a state of disequilibrium, and during equilibration towards the Bo field the spin releases energy that it received from the RF pulse. The local milieu of the atom - i.e. whether it is in grey matter, white matter, bone or cerebrospinal fluid - determines the speed of this relaxation. This is the basis of contrast in the MR image, and thus what makes it possible to visualize the different tissues of the body.*

The contrast in an MR image is determined by the sequence and the parameters of the sequence, among others the echo time (TE) and the repetition time (TR). TE is the time from excitation of the nuclei to sampling of the centre of each readout line, and TR is the time elapsed between two excitations. With a short TR and a short TE the T1 contrast is maximized, and with a long TR and a long TE the T2 contrast is maximized. T1 and T2 change with the strength of the applied field. With increasing magnetic strength T1 increases, although not proportionally for white matter and grey matter, which leads to a decreased T1- contrast between white and grey matter at high field. With increasing field strength T2 decreases and, due to disproportionate changes in T2 between grey and white matter,

the T2 contrast between the two tissue types increases. Due to the changes in T1 and T2 with increasing field strength, some adjustments of sequence parameters are required to obtain the same or better image contrast in structural imaging when advancing from low field to high field. In addition, different strategies to obtain good image contrast at high field are often employed, e.g., in T1-weighted sequences at high field, an inversion pulse can be added to improve T1 contrast (this also applies to low field). One of the advantages of high field strength is an increased SNR, which is calculated as the ratio between signal from the tissue and the standard deviation of the noise image. As the signal is proportional to the square of the applied field, (B_0), and the noise is proportional to the applied field, (B_0), SNR increases linearly with field strength. The higher SNR at high field strength also allows sampling of thinner sections and higher image resolution within similar imaging times.

Manuscripts

Manuscript I

Dyrby TB., Jelsing J., Alexander D. C., Baaré W.F.C., Søgaard LV., Optimisation of post mortem diffusion-weighted imaging
Submitted

Manuscript II

Dyrby TB., Søgaard LV., Parker GJM., Alexander DC., Lind NM., Hay-Schmidt A., Eriksen N., *Pakkenberg B., Paulson OB., Jelsing J. Validation of in vitro probabilistic tractography. Neuroimage. 2007 Oct 1;37(4):1267-1277. Epub 2007 Jul 10.

Manuscript III

Dyrby TB., Rostrup E., Baaré WFC., van Straaten ECW., Barkhof F., Vrenken H., Ropele S., Schmidt R., Erkinjuntti T., Wahlund L-O., Pantoni L., Inzitari D., Paulson OB., Hansen LK., Waldemar G. on behalf of the LADIS study group, Segmentation of Age-related White Matter Changes in a Clinical Multi-centre Study. Neuroimage. 2008, doi:10.1016/j.neuroimage.2008.02.024

Manuscript IV

Dyrby T. Liptrot M.G., Standardizing MR image Intensity In Multi-Center Studies. (Oral presentation) Proc Intl Soc Magn Reson Med 2005. (Miami, USA)

Manuscript I

Dyrby TB., Jelsing J., Alexander D. C., Baaré W.F.C., Søgaard LV., Optimisation of post mortem diffusion-weighted imaging
Submitted

Optimisation of post mortem diffusion-weighted imaging

Tim B Dyrby[1,2,3], Jacob Jelsing[4,5], Daniel C Alexander[6], William FC Baaré[1], Lise V Søgaard[1]

[1]Danish Research Centre for Magnetic Resonance, Copenhagen University Hospital, Hvidovre, Denmark. [2]Memory Disorders Research Group, Department of Neurology, Rigshospitalet, Copenhagen University Hospital, Copenhagen, Denmark. [3]Intelligent Signal Processing Group, Informatics and Mathematical Modelling, Technical University of Denmark, Lyngby, Denmark. [4]Research Laboratory for Stereology and Neuroscience, Copenhagen University Hospital, Bispebjerg, Denmark. [5]Rheoscience A/S, Denmark. [6]Centre for Medical Image Computing, Department of Computer Science, University College London, London, United Kingdom.

Corresponding author:
Tim B. Dyrby
Danish Research Centre for Magnetic Resonance
Copenhagen University Hospital, Hvidovre
Phone: +45 3645 6203
Fax: +45 3647 0302
Email: timd@drcmr.dk

ABSTRACT

High quality diffusion-weighted imaging (DWI) data is essential for testing and validating fibre reconstruction and tracking algorithms. Postmortem DWI is potentially superior to in vivo DWI, as it benefits from high-field MR scanners and long scanning times, thereby improving signal-to-noise ratio and spatial resolution. Moreover, degrading effects observed in vivo such as physiological noise are absent.

The present study investigated the short and long-term stability of perfusion-fixated tissue and the selection of sequence parameters in order to obtain a high quality postmortem DWI dataset. Eight porcine brains were fixated using transcardial perfusion and used as a highly gyrated animal model. Our initial experiment indicated that short-term instabilities were apparent for up to 15 hours after placing a brain in the scanner. After ensuring a stable scanning environment, crossing fibres were determined consistently using persistent angular structure (PAS) MRI and a voxel classification method based on spherical harmonics, at b-values between 2475 and 8181 s/mm^2. Inter- and intra-brain variations in diffusivity in cortical grey and white matter regions were insignificant throughout the 24 months period of investigation.

Using a b-value of 4009 s/mm^2 and continuous scanning over a ten-day period we obtained a single high-quality whole brain DWI dataset that allows for testing and developing fibre reconstruction methods. Resulting FA maps showed highly structured rims in cortical GM and hippocampus. Although it is tempting to interpret these rims as reflecting different cortical layers, more detailed investigations are necessary before such claims can be made.

KEYWORDS

Animal model; Brain; Cortex; Cortical layers; Crossing fibres; DTI; diffusion; ex vivo; in vitro; Hippocampus; Porcine; Postmortem; Testing; Tractography; Fixation; Validating

INTRODUCTION

Diffusion-weighted magnetic resonance imaging (DWI) provides a unique method for probing the micro structural diffusion properties of water in the brain. Diffusion tensor imaging (DTI) (Basser et al., 1994) and related mathematical fibre reconstruction models such as q-ball imaging (Tuch, 2004), tensor-mixture models (Alexander, 2005; Assaf et al., 2004; Tuch et al., 2002), PASMRI (Jansons et al., 2003) and spherical deconvolution (Frank, 2002; Tournier et al., 2004) reconstruct water-diffusion anisotropy as well as the directionality of the true underlying microstructure probed by DWI. Brain connectivity can then be modelled and visualised using fibre-tracking algorithms based on the reconstructed anisotropic directionality (Basser et al., 2000; Behrens et al., 2003; Jiang et al., 2006; Parker et al., 2003b; Parker et al., 2003a; Parker et al., 2005).

In order to validate mathematical reconstruction models, different approaches have been pursued. Artificial datasets (Alexander, 2005; Lazar et al., 2003; Leemans et al., 2005) or phantoms (Perrin et al., 2005; Watanabe et al., 2006) which have been used for initial validation of a reconstruction model obviously do not represent the neural complexity found in vivo. The acquisition of high-quality in vivo DWI datasets, however, is difficult as scanning time is limited for ethical and practical reasons, thereby compromising image resolution, signal-to-noise ratio (SNR), choice of b-value and the number of diffusion weighting directions (Jones, 2004; Skare et al., 2000). Moreover, the quality of in vivo DWI datasets suffers from (head) motion, physiological noise and geometric distortion artefacts (Skare et al., 2001) (for review Le Bihan et al., (2006)). To overcome these problems researchers have recently started to explore the use of postmortem DWI data for

validation purposes (Dyrby et al., 2007;Schmahmann et al., 2007). Indeed, postmortem DWI allows for prolonged scanning sessions and the use of high-field experimental MR scanners with stronger gradients to increase the b-value, SNR and image resolution of datasets. Moreover, postmortem data is not distorted by motion or physiological noise artefacts. Finally, sequences such as conventional diffusion weighted spin-echo (DW-SE), that benefit from minor image distortions as compared to the fast echo-planar imaging (EPI) sequences, can readily be applied since scanning time is less of an issue.

Despite its great potential, postmortem DWI is challenging. Electron microscopic studies of excised human white matter samples indicate that, directly after excision (0 hr), glial cells, axons, and myelin sheaths are well preserved, but that after 25 hrs at 25 °C significant autolytic changes can be observed in all WM components (Hukkanen et al., 1987). In agreement with the latter, D'Arceuil et al. (2007a) showed that by increasing time between time of death and (immersion) fixation of ex vivo (mice) brain tissue anisotropy measures and tractography results significantly degraded after already about 24 hours. Clearly, the autolytic progression needs to be stopped, preferably before its initiation.

Limiting autolytic changes and stabilizing the cellular and tissue constituents can be accomplished by means of chemical fixation of the tissue (Srinivasan et al., 2002). Generally, T1 and T2 relaxation times in postmortem tissue gradually decline over a period of days following fixation (Tovi et al., 1992; Yong-Hing et al., 2005). The exact mechanisms responsible for these changes are not fully understood. However, the used fixative (Thelwall et al., 2006) and employed fixation procedure (immersion- versus perfusion-fixation) (Adickes et al., 1997; Monfils et al., 2005) play essential roles.

Results from DWI studies on postmortem human brain tissue, fixated using the immersion method, have been inconsistent and differ from detecting no signal (Pfefferbaum et al., 2004), to detecting minor pathological changes (Larsson et al., 2004; Schmierer et al., 2007), to visualisation of detailed anatomical structures in parts of the hippocampus (Shepherd et al., 2007). In contrast to immersion fixation, the use of transcardial perfusion fixation procedures in animal studies allows preserving tissue in a state close to the in vivo situation and allows for collecting of high quality DWI datasets reflecting the almost true in vivo microstructure. Until now little attention has been given on how to optimize sequence parameters for postmortem DWI. Moreover, studies often do not provide information on how possible sources of noise such as (brain) tissue preparation and fixation time, might have influenced the quality of postmortem DWI data.

The present study aimed to create a high quality postmortem DWI dataset to allow for testing and developing fibre reconstruction methods, without known limitations of in vivo DWI. The porcine brain was chosen as a model because it closely resembles the complex neuroanatomy of the human brain (for review Lind et al., (2007)), and through its size allows for good anatomical resolution in an experimental MR scanner. Porcine brains were fixated using transcardial perfusion. We empirically explored the effects of different b-values on our ability to identify fibre directions using three different fibre reconstruction methods. Moreover, we visualised brain preparation effects as a short-term instability artefact introduced in the DWI dataset and investigated the stability of diffusion coefficients over time.

METHODS

Animals

In total, eight normal pig brains were used in this study; seven young Göttingen minipigs (P1 – P7; 3 months of age, 5 - 6 kg in body weight; Ellegaard Göttingen Minipigs A/S, Dalmose, Denmark) and one (P8) fully-grown landrace pig (> 12 months, body weight 40 kg). The animals were sedated using a Zoletile® mixture and perfusion-fixated transcardially in 4% paraformaldehyde (PFA) (Dyrby et al., 2007). Their brains were removed, post-fixated for at least 12 hours in 1% PFA and then transferred to phosphate-buffered saline (PBS – 0.1 mol/l, pH 7.4) at 5^{o}C. All procedures followed guidelines for the care and use of experimental animals approved by the Danish Animal Experiments Inspectorate. Postmortem scanning was performed using an experimental 4.7 tesla Varian Inova scanner with a single channel volume RF coil. DWI was acquired using a diffusion-weighted 2D single spin echo sequence (DW-SE), which compared to the DW-SE-EPI, has minimal image distortions since it does not suffer from the well-known EPI problems of eddy-current distortions and susceptibility artefacts e.g. at tissue-air interfaces (for review Le Bihan et al., 2006). The latter is an important issue in postmortem MRI since air bubbles are difficult to identify and to eliminate without damaging the tissue. Air bubbles are typically observed in the lateral ventricles and between sulci.

Preparation for MR scanning

Prior to scanning, brains were kept at room temperature for at least six hours to allow for temperature stabilisation. Unless otherwise stated, the brain was placed in a sealed plastic bag with a minimum of fluid surrounding it. This reduced the strong unwanted water proton signal as well as the noise contribution produced outside the tissue of interest to be introduced in the DWI dataset. Before being placed in the coil, soft foam was gently wrapped around the prepared brain to stabilize it during the scanning session. Finally, since DWI datasets were used for validating tractography of specific fibre projections emanating from the cerebral cortex (Dyrby et al., 2007) the brains were placed in the coil in such a way that the signal loss due to RF inhomogeneity only affected the cerebellum.

Data post-processing

No retrospective processing of the data was needed since the magnet system was very stable with a drift of about 0.1 Hz/hr. This means that DWI datasets could be obtained non-stop over very long time periods (days) with a minimal B0 drift introduced. Motion and physiological artefacts do not exist and geometric distortions due to eddy currents and susceptibility artefacts are low when using the DW-SE sequence. To separate background and brain, a brain mask was generated by summing up all the volumes within a dataset, and selecting an optimal intensity threshold.

Experiments

Firstly, we investigated short-term "tissue" instability over a time period of 22 hours. Secondly, we empirically explored the effects of different b-values on our ability to identify fibre directions using three different reconstruction methods. Using an "optimal" b-value we then acquired a single high-quality whole brain DWI dataset over a ten-day continuous scanning period with a final SNR > 60. Finally, repeated scanning sessions allowed us to investigate the consistency and stability of diffusivity across brains and over time.

Experiment 1: Short-term stability

Three pig brains (P1 - P3) were used to explore "tissue" instabilities appearing within a time period of 22 hrs from when a brain was placed in the scanner. In this experiment fluid surrounded the tissue. Whole brain DWI datasets were obtained in an interleaved manner. First all odd numbered slices were acquired four times (number of excitations (NEX) = 4). Next, even numbered slices were obtained (NEX = 4). One DWI dataset consisted of two non-DW image volumes and 42 DW-volumes with different gradient directions and a b-value of 865 s/mm^2. The b-value was somewhat arbitrary selected, however, to ensure a diffusion weighted signal from surrounding fluid the b-value was chosen not to be too high. It took 7.5 min to acquire one volume (half the slices; TR = 3500 ms, matrix = 128 x 128 and 28 slices; image resolution = 0.5 x 0.5 x 0.5 mm^3. Thus, the time lag between even and odd slices constituting a complete (whole brain) volume was 22 hours (4 x (2+42) x 7.5 min). Short-term instabilities were visualised as a time series of mean intensity changes over a period of 22 hours with a time resolution of 7.5 min by subtracting the mean intensity of even and uneven slice volumes (e.g. even

volume 1 minus uneven volume 1, etc). The mean of the 10 last time points were subtracted from each time point to ensure a common baseline. Three regions-of-interest (ROI) were used to study the short-term instabilities, one including brain tissue, one including surrounding fluid and a small ROI including fluid in the ventricles.

Experiment 2: b-value selection

Eight DWI datasets with differing b-values were acquired in one continuous scanning session on brain P4 613 days post mortem**.** In pilot experiments we observed an "optimal" b-value to lie around the 4000 s/mm^2. Therefore, in the final experiment we tested a pseudo logarithmic distribution of b-values around 4000 (acquisition schemes I – VIII, Table 1). Each DWI dataset consisted of 4 repetitions of three non-diffusion-weighted image volumes and 61 volumes with different gradient directions optimized as outlined by Jansons and Alexander (2003). Sequence parameters: TE = 67.8 ms; TR = 2500 ms; diffusion sensitization gradient duration δ = 27 ms; time between gradient pulse onset Δ = 33.5 ms; matrix = 128 x 64; 5 axial slices; slice gap= 3.5 mm; 0.5 x 0.5 x 0.5 mm^3 voxels. For each b-value, after averaging the four repeated DWI datasets, the SNR ratio was > 21.

The SNR was calculated as follows: two regions of interest (ROI) were placed on a non-diffusion weighted image - one ROI in white matter (WM) representing the mean signal, and one ROI in the background representing the noise level. Since the MR images are magnitude representations, the WM signal tends towards a Gaussian distribution whilst the background (BG) signal is Rician distributed (Sijbers et al., 1998). The SNR for a single channel coil can then be expressed as:

$$SNR = \frac{mean(WM_{ROI})}{\sqrt{\frac{mean(BG_{ROI}^2)}{2}}} \cdot \sqrt{NEX} \quad (1)$$

where the nominator is the 'signal' of the SNR represented by the mean intensity of the ROI in the WM, the denominator is the 'noise' represented by the standard deviation of the background ROI in the image. NEX is the number of averages.

To find an optimal b-value range we qualitatively evaluated how the different b-values affected three different established fibre reconstruction methods implemented in the Camino MRI toolkit (http://www.cs.ucl.ac.uk/research/medic/camino/). *Method 1*: The (single) tensor model (Basser et al., 1994) was used to reconstruct fibre directions in each DWI dataset with different b-value. To qualitatively express how b-values influence the reconstructed fibre direction the mean angular deflection was calculated using a leave-one-out type of analysis (Hastie et al., 2001). The mean deflection is a generalisation error that expresses how fibre directions reconstructed in a DWI dataset obtained at one b-value deflects to corresponding fibre directions reconstructed from a range of related b-values. First, we calculated for each b-value the angular deflection (e.g. dot product between two unit vectors) for reconstructed fibre directions over all voxels in an axial slice though the internal capsule, with all other b-values. Angular deflections were calculated for the first principal eigenvector only. Finally, for each b-value angular deflections were averaged over all voxels and subsequently plotted as a function of b-value. Only voxels within three ROIs were included in the analysis (Fig. 2): One ROI contained voxels with FA values larger than 0.3 (based on the DWI dataset with b = 4009 s/mm^2), another ROI was placed in the corpus callosum (CC) containing

voxels with high anisotropy and the third ROI covered a more complex region in the rostral semiovale and internal capsule. *Method 2*: The persistent angular structure (PAS) MRI is a non-parametric q-space method that reconstructs a function of a sphere where the PAS indicates the relative mobility of water molecules in each direction. The peaks of the PAS provide estimates of orientations of one or more fibres crossing within a voxel (Jansons et al., 2003). *Method 3*: The spherical harmonics (SH) decomposition method. Here voxels likely to include crossing fibres were identified by the voxel classification algorithm of Alexander et al. (2002). This method fits even series of spherical harmonics up to 0^{th}, 2^{nd} and 4^{th} order. Truncation at each order represents (a) isotropic diffusion, (b) anisotropic Gaussian diffusion or (c) non-Gaussian diffusion, respectively. The non-Gaussian class may arise from crossing fibres as well as other configurations such as fanning and bending. An F-test is used to classify voxels into one of the three categories. An F-test threshold of 10^{-13} was used to separate isotropic diffusion from anisotropic Gaussian diffusion and an F-test threshold of 10^{-8} separated anisotropic Gaussian diffusion from non-Gaussian diffusion (see Alexander et al., 2002).

Experiment 3: Diffusivity stability

DWI data of brains P4 through P8 scanned at 613, 65, 18, 35 and 392 days postmortem respectively, were used to evaluate the consistency and stability of diffusivity across brains. Furthermore, DWI data consisting of 4 acquisitions between postmortem day 24 and 65 in P5, and 5 acquisitions between postmortem day 6 and 375 in P8, were used to investigate long term effects. For P4 - P7 DWI scan parameters were as described under experiment 2, using a b-value of 4009 s/mm^2. For P8 the following settings were used: b-value = 4090

s/mm^2; TE = 80.1 ms; G = 63 mT/m; δ = 16.5 ms; Δ = 58.4 ms; voxel dimensions = 0.63 x 0.63 x 0.63 mm^3. The mean (apparent) diffusivity (MD) and the (ordered) eigenvalues along the three principal directions derived from a single tensor model were calculated in 2 regions of interest (ROI), one in white matter (WM) and one in cerebral grey matter (GM). ROIs were delineated on a slab of axial slices extending from below the inferior part of the corpus callosum to above the centrum semiovale by means of intensity thresholding and subsequent manual editing. Since the WM ROI covered a heterogeneous region of crossing fibres not correctly reconstructed by the single tensor model, voxels with a FA value less then 0.3 were excluded. ROIs were drawn using the MIPAV program (http://mipav.cit.nih.gov). Datasets included in the long-term experiment generally covered the whole brain. Some datasets, however, contained half the number of slices since a gap of one slice thickness was used. Nevertheless, since both the GM and the WM ROI covered a large region, this difference in number of slices is unlikely to influence our results.

RESULTS

Experiment 1: Short-term instabilities

Short-terms instabilities over time are shown figure 1. Major intensity discrepancies observed in the brain tissue ROI within the first five hours of scanning gradually levelled out and were almost completely absent after 15 hours. Mean intensity differences in the ROI containing surrounding fluid and fluid in the ventricles were absent at all time points. We did not observe a correlation between DW-directions and mean intensity differences. Both the MD and FA maps were sensitive (most pronounced in the MD maps) to short-term instabilities with discontinuities being visible in the slice direction (results not shown).

Based on the above results, only DWI datasets obtained at least 15 hours after a brain was placed in the scanner were included in the rest of the study.

Experiment 2: b-value selection

Mean angular deflection error in the principal direction plotted as a function of b-value is shown in figure 2. For all thee ROIs the mean angular deflection error was minimal for b-values in the 3 to 4 thousand range (Fig. 2). For the two ROIs containing anisotropic voxels (CC ROI and FA > 0.3), the change in the mean deflection error was observed to be most pronounced between the two lowest b-values (1018 and 2475 s/mm^2).

In contrast to the tensor model, PASMRI modelled complex fibres with both crossing and branching fibre profiles. In PASMRI reconstructions, PAS directions at the lowest b-value (1018 s/mm^2) were less well defined than at the other b-values (Fig. 3 A). Indeed, PAS directions at higher b-values were spikier, less broad, more consistent in the number of fibre directions found, and spatially more coherent (Fig. A - C). These differences were most obvious when going from the lowest b-value at 1018 s/mm^2 to 2475 s/mm^2 (Fig. 3 A-B).

The SH classification method started to identify clusters containing non-Gaussian voxels at b-value 3069 s/mm^2 in brain areas containing complex fibres e.g. in the internal capsule. These clusters became more circumscribed with increasing b-values (Fig. 3 F - J). Clusters seemed most robust for b-values between 3069 s/mm^2 and 8181 s/mm^2. For b-values larger than 8181 s/mm^2 the extent of the clusters with non-Gaussian fibre were highly dependent on the F-test threshold (not shown). For b-values lower than 4009 s/mm^2, voxels expected to be isotropic (e.g. in the ventricles where some fluid was preserved) were classified as being anisotropic.

High-quality whole brain DWI dataset

Brain P5 (65 days post mortem) was scanned continuously over a ten-day period to obtain a single high-quality whole brain DWI dataset. Based on the results of experiment 2 we used a b-value of 4009 s/mm^2. The final SNR was > 60 with NEX = 8. Reconstruction was based on the single tensor model and PASMRI that was applied directly to the DWI dataset without any further retrospective processing (Fig. 4). In

general, the FA map contained detailed structural information and high contrast within both GM and WM. In cortical GM two parallel and continuous highly structured rims were observed on the FA map; one rim close to WM containing low FA values (< 0.1) (1 - 1½ voxels wide) and an outer rim with higher FA values (0.23 ± 0.05). In the rim containing low FA values, two crossing fibres were consistently found by PASMRI, whereas a single fibre direction was found in the outer rim. Similar rims in the FA map were observed separating the layers of the hippocampus. No obviously rims were observed in the MD map (results not shown). No structured anisotropic diffusivity was observed in any of the deep GM nuclei such as putamen, caudate or thalamus.

Experiment 3: Diffusivity stability across brain and ROIs

Across brains no significant differences were observed in MD or in diffusivity along the three principal directions, in either the WM or the cortical GM ROI (Tables 2 and 3).

Diffusivity in cortical GM, as compared to WM, tended to be higher along the 2^{nd} principal direction and was significantly higher along the 3^{rd} principal direction (Tables 2 and 3).

Experiment 3: Diffusivity stability over time

With increased time post mortem, we did not observe significant differences in MD between P5 and P8, or between WM or cortical GM. When averaged over time, the mean and standard deviation (SD) of MD in WM and cortical GM were respectively 0.23 (± 0.03) and 0.25 (± 0.01) x 10^{-3} mm^2/s for P5, and 0.21 (± 0.02) and 0.25 (± 0.02) x 10^{-3}

mm^2/s for P8. The observed change in MD over a longer period of time for the same brain was less than the difference found between brains at different times postmortem (Tables 2 and 3). When comparing repeated investigations across brains P5 to P8 versus time post mortem, the diffusion coefficients were generally stable throughout (Fig. 5). However, at day 6 post mortem the diffusivities of P8 tended to be lower than at the following time points. At the last time points 613 or 375 days post mortem for respectively P4 and P8, a decreased diffusivity (though very small) was apparent in both the WM and cerebral GM ROIs when compared to the prior time points, 166 or 42 days post mortem.

DISCUSSION

In the present study we investigated the short and the long-term stability of perfusion-fixated tissue and the selection of sequence parameters to obtain a DWI dataset suitable for testing/developing reconstruction and tractography methods as well as validation of the latter against independent anatomical data such as in vivo tracers (Dyrby et al., 2007). The porcine brain was used as a highly gyrated animal model for the human brain but the results presented pertain to other animal models as well.

Preparation for MR-scanning

Unwanted short-term instabilities were evident within the first 15 hours of scanning. Instabilities in brain tissue were most pronounced in the beginning of a scanning session and subsequently faded out. Temperature conduction and mechanical processes most likely underlie the observed instabilities. The temperature factor relates to the time it takes for the brain/coil assembly to equalize to the temperature inside the magnet whilst acquiring DWI. The tissue temperature determines how fast water molecules probe the micro-structural environment (assuming mechanical stability). The lower temperature in postmortem tissue (in this study approximately 18.5 $^{\circ}$C) compared to in vivo (37 $^{\circ}$C) slows down the molecular motion and hence the diffusivity decreases. Apart from the absolute temperature in the scanner, minor temperature variations during scanning, are not believed to degrade the validity of DWI datasets for example for tractography, since the probed environment and hence the directional information is consistent. The mechanical factor relates to the time it takes for brain tissue to “stop moving” after physical handling (shaking, squeezing

positioning in the coil etc.). Mechanical instabilities may introduce a spatial change in the microstructure (assuming temperature stability), meaning that the tissue slowly deforms over time, and hence the directional information deforms with it.

The influence of temperature conduction in our study was believed not to be present by the fact that instabilities in the fluid surrounding brain tissue and within the ventricles, which does not suffer from mechanical processes, were absent at all time points.

To ensure a stable scan environment, only DWI datasets obtained at least 15 hours after a brain was placed in the scanner were included in the study. Please note that this time is idiosyncratic for the current setup as many different preparation strategies/procedures can be envisioned. The bottom-line is that a stable environment is essential to obtain robust postmortem DWI data.

Sequence parameters

A main prerequisite for modelling 'true' single, crossing, fanning or alike fibre structures in a DWI dataset, is a suitable b-value. For perfusion fixated brain tissue, our results suggest that in our setup an "optimal" b-value would lie somewhere between ~2000 and ~8000 s/mm^2. For the single tensor model the optimal range was between ~2000 and ~4000 s/mm^2. The "optimal" b-value for PASMRI was at least higher than ~1000 s/mm^2. For the SH classification method the optimal b-value lay between ~3000 and ~8000 s/mm^2. The upper bound mainly depends upon how sensitive a particular reconstruction method is to the noise floor. It is important to note that selecting too low a

b-value diminishes the ability to robustly discriminate crossing fibres within a voxel and lowers the spatial coherence of reconstructed fibres.

Our results are in agreement with those of D'Arceuil et al. (2007b). In the latter study, using (immersion) fixated monkey brains, the b-value was initially increased to 4025 s/mm^2 in proportion to the observed 25% decrease in MD in vitro as compared to in vivo. However, following final analyses the optimal b-value for WM was determined to be 5200 s/mm^2. In contrast, Zhang et al. (2005) selected a b-value of 1000-1200 s/mm^2 for fixated mice brains, but failed to report on which criteria his choice was based and the fixation procedure used. Sun et al. (2005) used perfusion fixated mice and increased the b-value by 44% to 1813 s/mm^2 to ensure that the signal attenuation in postmortem diffusion was comparable to what they observed in vivo. Guilfoyle et al., (2003) selected a b-value of 900 s/mm^2 to be used in vivo, as well as in vitro on perfusion fixated mice brains. The b-value reported in the latter three studies lie in the lower end of the range of "optimal" b-values observed in the present study.

Using a b-value of 4009 s/mm^2 and continuous scanning over a ten-day period we obtained a single high-quality whole brain DWI dataset (SNR was > 60). Interestingly, in resulting (colour code) FA maps two parallel and continuous highly structured rims became apparent in GM indicating. A high anisotropy was found in the outer rim with a main diffusion direction perpendicular to the surface of the cortex. This rim may represent the relatively wide supragranular layers II - III known to harbour corticocortical interconnecting neurons. The inner rim has an almost isotropic diffusivity when using the tensor model however, PASMRI consistently detected two crossing fibres; one perpendicular and one parallel to the surface of WM. This might reflect the

rich interconnection between cortical layer IV – VI, and especially in the multiform layer (layer VI) which is known from histology to contain crossing fibres.

Similar rims were observed separating the layers of the hippocampus. More detailed investigations are necessary to determine how much are related to I) a partial volume effect (PVE) between lower cerebral cortical layers and the short association fibres (U-fibres) in WM and II) the exact cytological characteristics, in terms of fibre directionality and neuron density, responsible for the different patterns of diffusivity.

Diffusivity and anisotropy

The MD and FA values observed in the present study are comparable to those reported from other postmortem animal brain studies (D'Arceuil et al., 2007b; Guilfoyle et al., 2003; Sun et al., 2005). Additionally, we found that the inter- and intra-brain variability in diffusivity and anisotropy was stable over the time period of investigation (613 days), as no statistical differences were observed within or across brains in either the GM or WM ROI. We did, however, observe a weak tendency of decreased diffusivity on the latest measurement time points. Ongoing chemical reactions caused by remaining fixative might explain this observation. More measurements after 12 months post mortem are needed to confirm this weak trend. Until then we can only speculate how this change might influence the quality of DWI datasets obtained at these late time points post mortem.

Several studies have found that the diffusivity in fixated tissue compared to in vivo is decreased significantly. For example, Sun et al., (2005) found that the diffusivity in GM

and WM was decreased 57 % and 72 %, results that were confirmed by D'Arceuil et al., (2007b) who found the diffusivity to be decreased 60 % and 80 %. Despite the decreased diffusivity no statistical difference in anisotropy was found between in vivo and postmortem (D'Arceuil et al., 2007b; Guilfoyle et al., 2003; Sun et al., 2005). The latter emphasizes that the structural information in fixated postmortem tissue is/can be preserved and, as indicated by our results, is likely stable over longer time periods post mortem. Since anisotropy does not change between in vivo and postmortem, a rotational invariant scaling factor of the diffusivities, common for all three principal directions, must exist. Two factors come to mind to explain such as a common scaling factor: a) the lower post mortem tissue temperature reduces the Brownian motion (a rotationally invariant process), and b) the fixative chemically stabilises or 'freezes' tissue by cross-linking proteins, leading to increased viscosity of the tissue and again slowing down molecular motion (probably a rotationally invariant process). Note that both factors are parameters in the Stoke-Einstein equation that will lead to decreased diffusivity.

Considerations/limitations

The approach employed in the current study was largely qualitative/empirical in nature. The short term-instabilities are probably mainly due to mechanical processes. Temperature conduction effects were not observed, probably because the tissue have been placed in room temperature that is close to the temperature inside the coil several hours before the scanning is started. However, a more detailed analysis would be necessary to elucidate underlying mechanisms more fully. Such an analysis was outside the scope of the current study.

The selection of a range of "optimal" b-values can be considered somewhat coarse. However, it is not clear whether a finer grained sampling of b-values would have given more insights. Indeed, our study suggests that there is a relatively broad range of b-values (2000 - 8000 s/mm^2) that allow for acquiring robust DWI data postmortem. Additional, it should be pointed out that the mean fibre deflection error between principal directions of the tensor model at different b-values does not really come from comparison with ground truth. However, it reveals the b-value that agrees most with the consensus from all b-values investigated, which should be a reasonable measure of integrity. Nevertheless, one should keep in mind that several other parameters may affect post mortem DWI. For example, incoherent blood flow in vessels and arteries in vivo can be suppressed by using higher b-values and is therefore not considered an important source of noise. In postmortem MRI, blood flow is absent, but instead vessels contain water or fixative, adding an isotropic signal component to the acquired DWI dataset. Because of this PVE, DWI datasets acquired on postmortem brain tissue for use in tractography entail a risk of showing increased directional uncertainty for fibres close to vessels or arteries.

In the present study, the amount of free water molecules surrounding the postmortem brain tissue was minimised in order to avoid its global contribution to the noise component and decrease of the overall SNR. However, when DW-EPI sequences are used, it is a necessity that some liquid surrounds the tissue in order to avoid severe susceptibility artefacts. One possible solution is the use of synthetic oils, such as Flourinert (FC-77) (Assaf et al., 2000; Ellegood et al., 2007; Kovacevic et al., 2005; Shinar et al., 2002). Another alternative to maximize SNR is to increase the temperature of the environment (D'Arceuil et al., 2007b;

Thelwall et al., 2006). However, short-term instabilities during the achievement of a homogeneous temperature within the brain should always be considered.

We successfully acquired a high resolution post mortem data set in the high gyrated porcine brain that allows for testing and developing fibre reconstruction methods, without many of the known limitations when obtaining in vivo DWI (e.g. physiological noise and geometric distortion artefacts). Nevertheless, postmortem DWI is still in its early stages. The present study addressed/identified only few of the issues that need consideration when doing post mortem DWI.

REFERENCES

Adickes, E.D., Folkerth, R.D., Sims, K.L., 1997. Use of perfusion fixation for improved neuropathologic examination. Arch.Pathol.Lab Med. 121, 1199-1206

Alexander, D.C., 2005. Multiple-fiber reconstruction algorithms for diffusion MRI. Ann.N.Y.Acad.Sci. 1064, 113-133

Alexander, D.C., Barker, G.J., Arridge, S.R., 2002. Detection and modeling of non-Gaussian apparent diffusion coefficient profiles in human brain data. Magn Reson.Med. 48, 331-340

Assaf, Y., Cohen, Y., 2000. Assignment of the water slow-diffusing component in the central nervous system using q-space diffusion MRS: implications for fiber tract imaging. Magn Reson.Med. 43, 191-199

Assaf, Y., Freidlin, R.Z., Rohde, G.K., Basser, P.J., 2004. New modeling and experimental framework to characterize hindered and restricted water diffusion in brain white matter. Magn Reson.Med. 52, 965-978

Basser, P.J., Mattiello, J., LeBihan, D., 1994. Estimation of the effective self-diffusion tensor from the NMR spin echo. J Magn Reson.B 103, 247-254

Basser, P.J., Pajevic, S., Pierpaoli, C., Duda, J., Aldroubi, A., 2000. In vivo fiber tractography using DT-MRI data. Magn Reson.Med. 44, 625-632

Behrens, T.E., Woolrich, M.W., Jenkinson, M., Johansen-Berg, H., Nunes, R.G., Clare, S., Matthews, P.M., Brady, J.M., Smith, S.M., 2003. Characterization and propagation of uncertainty in diffusion-weighted MR imaging. Magn Reson.Med. 50, 1077-1088

D'Arceuil, H., de Crespigny, A., 2007a. The effects of brain tissue decomposition on diffusion tensor imaging and tractography. Neuroimage. 36, 64-68

D'Arceuil, H.E., Westmoreland, S., de Crespigny, A.J., 2007b. An approach to high resolution diffusion tensor imaging in fixed primate brain. Neuroimage. 35, 553-565

Dyrby, T.B., Sogaard, L.V., Parker, G.J., Alexander, D.C., Lind, N.M., Baare, W.F., Hay-Schmidt, A., Eriksen, N., Pakkenberg, B., Paulson, O.B., Jelsing, J., 2007. Validation of in vitro probabilistic tractography. Neuroimage. 37, 1267-1277

Ellegood, J., McKay, R.T., Hanstock, C.C., Beaulieu, C., 2007. Anisotropic diffusion of metabolites in peripheral nerve using diffusion weighted magnetic resonance spectroscopy at ultra-high field. J Magn Reson. 184, 20-28

Frank, L.R., 2002. Characterization of anisotropy in high angular resolution diffusion-weighted MRI. Magn Reson.Med. 47, 1083-1099

Guilfoyle, D.N., Helpern, J.A., Lim, K.O., 2003. Diffusion tensor imaging in fixed brain tissue at 7.0 T. NMR Biomed. 16, 77-81

Hastie,T., Tibshirani,R., and Friedman,J. (2001). The elements of statistical learning. Springer), pp. chap. 7.

Hukkanen, V., Roytta, M., 1987. Autolytic changes of human white matter: an electron microscopic and electrophoretic study. Exp.Mol.Pathol. 46, 31-39

Jansons, K.M., Alexander, D.C., 2003. Persistent Angular Structure: new insights from diffusion magnetic resonance imaging data. Inverse Problems 19, 1031-1046

Jiang, H., van Zijl, P.C., Kim, J., Pearlson, G.D., Mori, S., 2006. DtiStudio: resource program for diffusion tensor computation and fiber bundle tracking. Comput.Methods Programs Biomed. 81, 106-116

Jones, D.K., 2004. The effect of gradient sampling schemes on measures derived from diffusion tensor MRI: a Monte Carlo study. Magn Reson.Med. 51, 807-815

Kovacevic, N., Henderson, J.T., Chan, E., Lifshitz, N., Bishop, J., Evans, A.C., Henkelman, R.M., Chen, X.J., 2005. A three-dimensional MRI atlas of the mouse brain with estimates of the average and variability. Cereb.Cortex 15, 639-645

Larsson, E.M., Englund, E., Sjobeck, M., Latt, J., Brockstedt, S., 2004. MRI with diffusion tensor imaging post-mortem at 3.0 T in a patient with frontotemporal dementia. Dement.Geriatr.Cogn Disord. 17, 316-319

Lazar, M., Alexander, A.L., 2003. An error analysis of white matter tractography methods: synthetic diffusion tensor field simulations. Neuroimage. 20, 1140-1153

Le Bihan, D., Poupon, C., Amadon, A., Lethimonnier, F., 2006. Artifacts and pitfalls in diffusion MRI. J.Magn Reson.Imaging 24, 478-488

Leemans, A., Sijbers, J., Verhoye, M., Van der Linden A., Van Dyck, D., 2005. Mathematical framework for simulating diffusion tensor MR neural fiber bundles. Magn Reson.Med. 53, 944-953

Lind, N.M., Moustgaard, A., Jelsing, J., Vajta, G., Cumming, P., Hansen, A.K., 2007. The use of pigs in neuroscience: modeling brain disorders. Neurosci.Biobehav.Rev. 31, 728-751

Monfils, M.H., Bray, D.F., Driscoll, I., Kleim, J.A., Kolb, B., 2005. A quantitative comparison of synaptic density following perfusion versus immersion fixation in the rat cerebral cortex. Microsc.Res.Tech. 67, 300-304

Parker, G.J., Alexander, D.C., 2003a. Probabilistic Monte Carlo based mapping of cerebral connections utilising whole-brain crossing fibre information. Lecture Notes in Computer Science 2732, 684-695

Parker, G.J., Alexander, D.C., 2005. Probabilistic anatomical connectivity derived from the microscopic persistent angular structure of cerebral tissue. Philos.Trans.R.Soc.Lond B Biol.Sci. 360, 893-902

Parker, G.J., Haroon, H.A., Wheeler-Kingshott, C.A., 2003b. A framework for a streamline-based probabilistic index of connectivity (PICo) using a structural interpretation of MRI diffusion measurements. J.Magn Reson.Imaging 18, 242-254

Perrin, M., Poupon, C., Rieul, B., Leroux, P., Constantinesco, A., Mangin, J.F., LeBihan, D., 2005. Validation of q-ball imaging with a diffusion fibre-crossing phantom on a clinical scanner. Philos.Trans.R.Soc.Lond B Biol.Sci. 360, 881-891

Pfefferbaum, A., Sullivan, E.V., Adalsteinsson, E., Garrick, T., Harper, C., 2004. Postmortem MR imaging of formalin-fixed human brain. Neuroimage. 21, 1585-1595

Schmahmann, J.D., Pandya, D.N., Wang, R., Dai, G., D'Arceuil, H.E., de Crespigny, A.J., Wedeen, V.J., 2007. Association fibre pathways of the brain: parallel observations from diffusion spectrum imaging and autoradiography. Brain 130, 630-653

Schmierer, K., Wheeler-Kingshott, C.A., Boulby, P.A., Scaravilli, F., Altmann, D.R., Barker, G.J., Tofts, P.S., Miller, D.H., 2007. Diffusion tensor imaging of post mortem multiple sclerosis brain. Neuroimage. 35, 467-477

Shepherd, T.M., Ozarslan, E., Yachnis, A.T., King, M.A., Blackband, S.J., 2007. Diffusion tensor microscopy indicates the cytoarchitectural basis for diffusion anisotropy in the human hippocampus. AJNR Am J Neuroradiol. 28, 958-964

Shinar, H., Seo, Y., Ikoma, K., Kusaka, Y., Eliav, U., Navon, G., 2002. Mapping the fiber orientation in articular cartilage at rest and under pressure studied by 2H double quantum filtered MRI. Magn Reson.Med. 48, 322-330

Sijbers, J., den Dekker, A.J., Van Audekerke, J., Verhoye, M., Van Dyck, D., 1998. Estimation of the noise in magnitude MR images. Magn Reson.Imaging 16, 87-90

Skare, S., Andersson, J.L., 2001. On the effects of gating in diffusion imaging of the brain using single shot EPI. Magn Reson.Imaging 19, 1125-1128

Skare, S., Hedehus, M., Moseley, M.E., Li, T.Q., 2000. Condition number as a measure of noise performance of diffusion tensor data acquisition schemes with MRI. J Magn Reson. 147, 340-352

Srinivasan, M., Sedmak, D., Jewell, S., 2002. Effect of fixatives and tissue processing on the content and integrity of nucleic acids. Am J Pathol. 161, 1961-1971

Sun, S.W., Neil, J.J., Liang, H.F., He, Y.Y., Schmidt, R.E., Hsu, C.Y., Song, S.K., 2005. Formalin fixation alters water diffusion coefficient magnitude but not anisotropy in infarcted brain. Magn Reson.Med. 53, 1447-1451

Thelwall, P.E., Shepherd, T.M., Stanisz, G.J., Blackband, S.J., 2006. Effects of temperature and aldehyde fixation on tissue water diffusion properties, studied in an erythrocyte ghost tissue model. Magn Reson.Med. 56, 282-289

Tournier, J.D., Calamante, F., Gadian, D.G., Connelly, A., 2004. Direct estimation of the fiber orientation density function from diffusion-weighted MRI data using spherical deconvolution. Neuroimage. 23, 1176-1185

Tovi, M., Ericsson, A., 1992. Measurements of T1 and T2 over time in formalin-fixed human whole-brain specimens. Acta Radiol. 33, 400-404

Tuch, D.S., 2004. Q-ball imaging. Magn Reson.Med. 52, 1358-1372

Tuch, D.S., Reese, T.G., Wiegell, M.R., Makris, N., Belliveau, J.W., Wedeen, V.J., 2002. High angular resolution diffusion imaging reveals intravoxel white matter fiber heterogeneity. Magn Reson.Med. 48, 577-582

Watanabe, M., Aoki, S., Masutani, Y., Abe, O., Hayashi, N., Masumoto, T., Mori, H., Kabasawa, H., Ohtomo, K., 2006. Flexible ex vivo phantoms for validation of diffusion tensor tractography on a clinical scanner. Radiat.Med. 24, 605-609

Yong-Hing, C.J., Obenaus, A., Stryker, R., Tong, K., Sarty, G.E., 2005. Magnetic resonance imaging and mathematical modeling of progressive formalin fixation of the human brain. Magn Reson.Med. 54, 324-332

Zhang, J., Miller, M.I., Plachez, C., Richards, L.J., Yarowsky, P., van Zijl, P., Mori, S., 2005. Mapping postnatal mouse brain development with diffusion tensor microimaging. Neuroimage. 26, 1042-1051

ACKNOWLEDGEMENT

We thank Geoffrey J.M. Parker, PhD from the ISBE, University of Manchester, and Matthew G. Liptrot, MSc and Annette Sidaros, MD, from the DRCMR, Copenhagen University Hospital Hvidovre for critical technical input on the aspects of in vitro versus in vivo DWI. Thanks to DVM Nanna Grand and Lars Ellegaard at Ellegaard Minipigs Aps for donating experimental animals. We would like to express our gratitude for the financial support from the Lundbeck Foundation, the Gangsted Foundation, the Danish Centre for Scientific Computing grant no. HDW-1104-08 and the Velux Foundation.

FIGURE LEGENDS

Fig. 1

Short-term instabilities in the tissue can appear in DWI datasets that are obtained immediately after tissue preparation. Two non-diffusion weighted and 42 diffusion weighted images were collected in an interleaved manner, and with a NEX of 4 the total scanning session was 44 hours. First, all the even and then all the odd slices were obtained. The time lag between odd and even slices was 22 hours thus having a 7.5 minute time resolution. Short-term instabilities were visualised in each time point as the mean intensity difference between the even and odd slices (for details see methods for experiment 1). Results are for P1 (black), P2 (red) and P3 (green). Mean intensity difference within brain tissue (solid), surrounding fluid (dashed) and fluid in ventricles (dot). Tissue is placed in the scanner at time equal 0. The delay before start of the DWI session is mainly the time it took to setup the scanning session.

Fig. 2

Between b-values, the mean angular deflection error of the principal direction. Eight identical anatomical DWI datasets were acquired in one continuous scanning session on pig brain P4 613 days post mortem. The b-values ranged from 1018 to 15750 s/mm^2 (acquisition scheme I – VIII, Table 1). (Left) The FA map of the axial slice used. The colour bar indicates the range of FA values from zero to one. (Right) Mean angular deflection was calculated between the principal directions reconstructed using the tensor model and for each b-value shown as a generalised error for the CC ROI (red), the mixed anisotropy ROI (blue) and for voxels with a FA > 0.3 (black).

Fig. 3

The impact of b-values on different reconstruction methods. The same DWI dataset as in Fig. 2 was used. Results are shown for b = 1018 (A, D), 2475 (B, E), 3069 (F), 4009 (G), 5911 (H), 8181 (I) and 15750 s/mm^2 (C, J) (Table 1) on the same axial slice as in Fig. 2. Reconstruction of fibre directions based on PASMRI (zoomed region indicated in (D)) (A - C). Fibre directions are RGB colour coded; Red =LR, green = AP and blue = SI. An immediate change in PAS directions are found from a b-value of 1018 to 2475 s/mm^2 where improved spatial coherence in fibre directions is observed (A - B). Based on a SH decomposition voxels are classified into three classes of diffusion (D - J); isotropic (black), anisotropic (grey) or non-Gaussian (white) diffusion. At low b-values some fluid left back in the ventricles are being classified as anisotropic (E - F, arrow). At higher b-values, clusters of non-Gaussian voxels were found consistently in WM regions

containing complex fibre compositions in rostral semiovale (F, G, arrow) and internal capsule (G, double arrow). Further increasing the b-value, clusters of isotropic voxels typical in GM starts to appear (I, J, arrow).

Fig. 4

Whole brain postmortem DWI dataset with high SNR. The DWI dataset was obtained in one continuous scanning session lasting 10 days on pig brain P5 with b-value 4009 s/mm^2. The voxel size was 0.5 x 0.5 x 0.5 mm^3, NEX = 8 and SNR > 60. Colour coded FA map (A, B) in coronal (A) and axial (C) view. The two regions in (B) are zoomed in (C, D) and shows reconstructed fibre directions using PASMRI overlaid onto FA values. The scale bar equal 10 mm. Detailed information on fibre orientation is seen in deep WM and WM in the gyri (C, double arrow). A rim of low FA values was consistent in cortical GM close to WM (A, B, arrow). This rim was found to contain crossing fibres (yellow overlay, C, D). Several similar rims of low FA values were observed in hippocampus (B, arrow).

Fig. 5

Inter- and intra brain variation in diffusivity with time post mortem. Mean diffusivity within cortical GM (red) and WM ROI (black) is shown for P4 – P8. Repeated measurements at different times post mortem are shown connected (line). For P4 – P7 the b-value was 4009 s/mm^2 and 4090 s/mm^2 for P8. In (A), (B), (C) and (D) are MD, the first-, second- and the third eigenvalue ($\lambda_{1\text{-}3}$) shown with time post mortem. No

statistical difference between brains and time post mortem is observed. Maximal contrast between GM and WM is clearly found for λ_3 (D) and the lowest for λ_1 (B).

TABLE LEGENDS

Table 1

Acquisition schemes. The b-value and used gradient strength (G).

Acquisition schemes	G (mT/m)	b-value (s/mm^2)
I	29	1018
II	44	2475
III	49	3069
IV	56	4009
V	68	5911
VI	80	8181
VII	84	11295
VIII	111	15750

Table 2

Inter-brain diffusivity and anisotropy (± SD) among five brains within the WM ROI. For brains P4 – P8 DWI datasets were acquired 613, 65, 18, 35 and 392 days post mortem respectively with b = 4009 s/mm^2 (Table 1). Diffusivity results are in (10^{-3} mm^2/s) and anisotropy was expressed by the FA measure. Only voxels with FA > 0.3 were included in the analysis.

Brains	*Diffusivity*				
	λ_1	λ_2	λ_3	***MD***	***FA***
P4	0.32 ±0.05	0.20 ±0.04	0.14 ±0.03	0.22 ±0.03	0.44 ±0.02
P5	0.35 ±0.07	0.20 ±0.05	0.14 ±0.04	0.23 ±0.04	0.45 ±0.13
P6	0.28 ±0.04	0.16 ±0.04	0.11 ±0.03	0.18 ±0.03	0.44 ±0.11
P7	0.24 ±0.08	0.13 ±0.05	0.09 ±0.04	0.16 ±0.05	0.47 ±0.12
P8	0.28 ±0.06	0.16 ±0.05	0.10 ±0.04	0.18 ±0.04	0.49 ±0.02
All brains	**0.29 ±0.04**	**0.17 ±0.03**	**0.12 ±0.02**	**0.19±0.03**	**0.46 ±0.02**

Table 3

Inter-brain diffusivity and anisotropy (± SD) among five brains within the cortical GM ROI. For brains P4 – P8 DWI datasets were acquired 613, 65, 18, 35 and 392 days post mortem respectively with b = 4009 s/mm^2 (Table 1). Diffusivity results are in (10^{-3} mm^2/s) and anisotropy was expressed by the FA measure. All voxels were included in the analysis.

Brains	*Diffusivity*				
	λ_1	λ_2	λ_3	***MD***	***FA***
P4	0.32 ±0.04	0.26 ±0.04	0.22 ±0.03	0.27 ±0.03	0.20±0.07
P5	0.31 ±0.04	0.25 ±0.03	0.21 ±0.03	0.26 ±0.03	0.18±0.07
P6	0.26 ±0.05	0.22 ±0.04	0.19 ±0.04	0.22 ±0.04	0.16±0.07
P7	0.26 ±0.06	0.21 ±0.05	0.17 ±0.05	0.21 ±0.05	0.21±0.08
P8	0.28 ±0.05	0.22 ±0.04	0.18 ±0.04	0.23 ±0.04	0.21±0.08
All brains	**0.29 ±0.03**	**0.23 ±0.03**	**0.20 ±0.02**	**0.24 ±0.02**	**0.19±0.02**

5. R1_Dyrby_Figure_1
Click here to download 5. Figure: R1_Dyrby_Figure_1.pdf

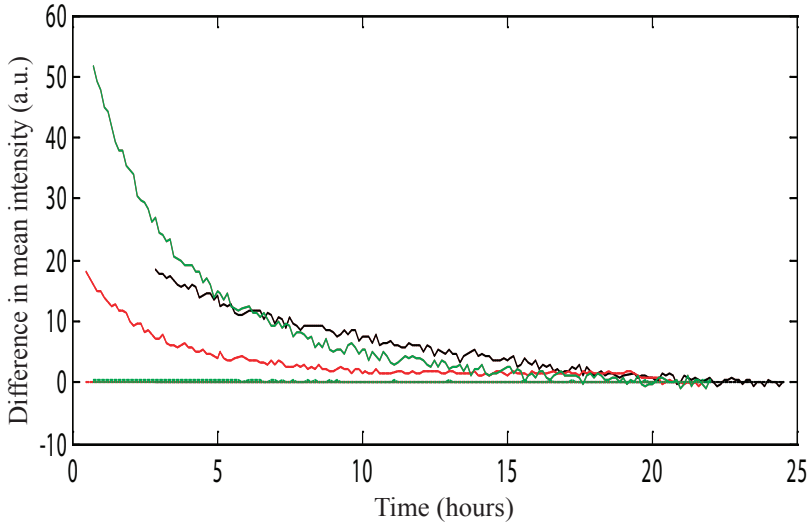

Figure 1 *Dyrby et al.*

5. R1_Dyrby_Figure_2
Click here to download 5. Figure: R1_Dyrby_Figure_2.pdf

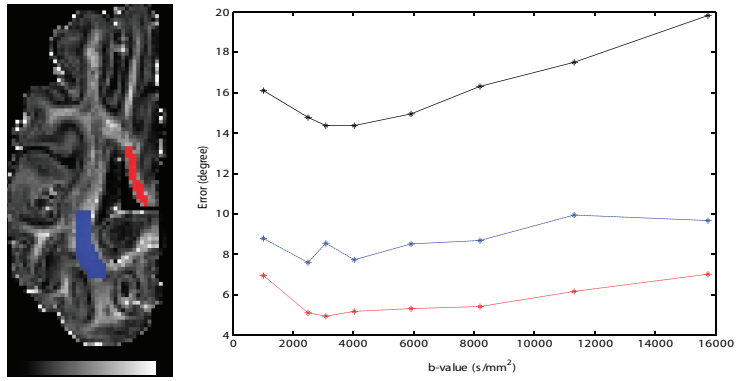

Figure 2 *Dyrby et al.*

5. R1_Dyrby_Figure_3
Click here to download 5. Figure: R1_Dyrby_Figure_3.pdf

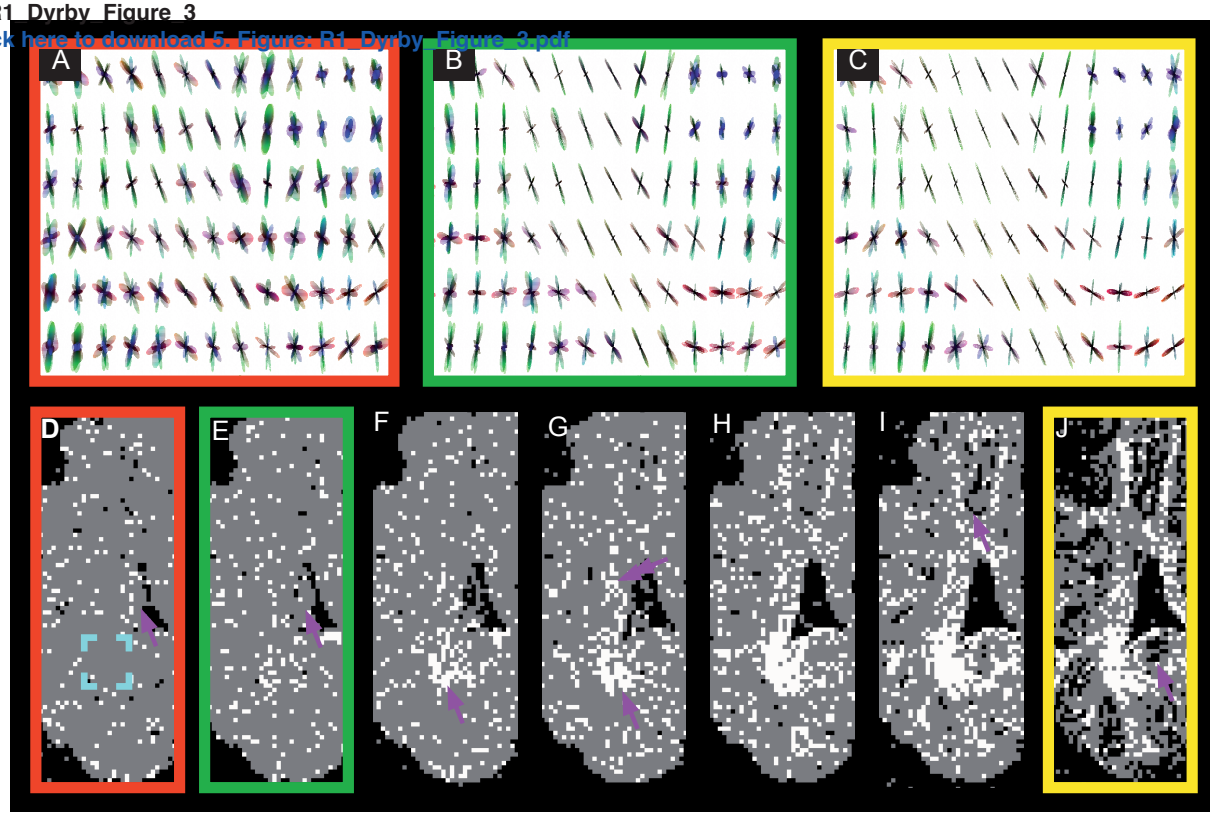

Figure 3 *Dyrby et al.*

5. R1_Dyrby_Figure_4
Click here to download 5. Figure: R1_Dyrby_Figure_4.pdf

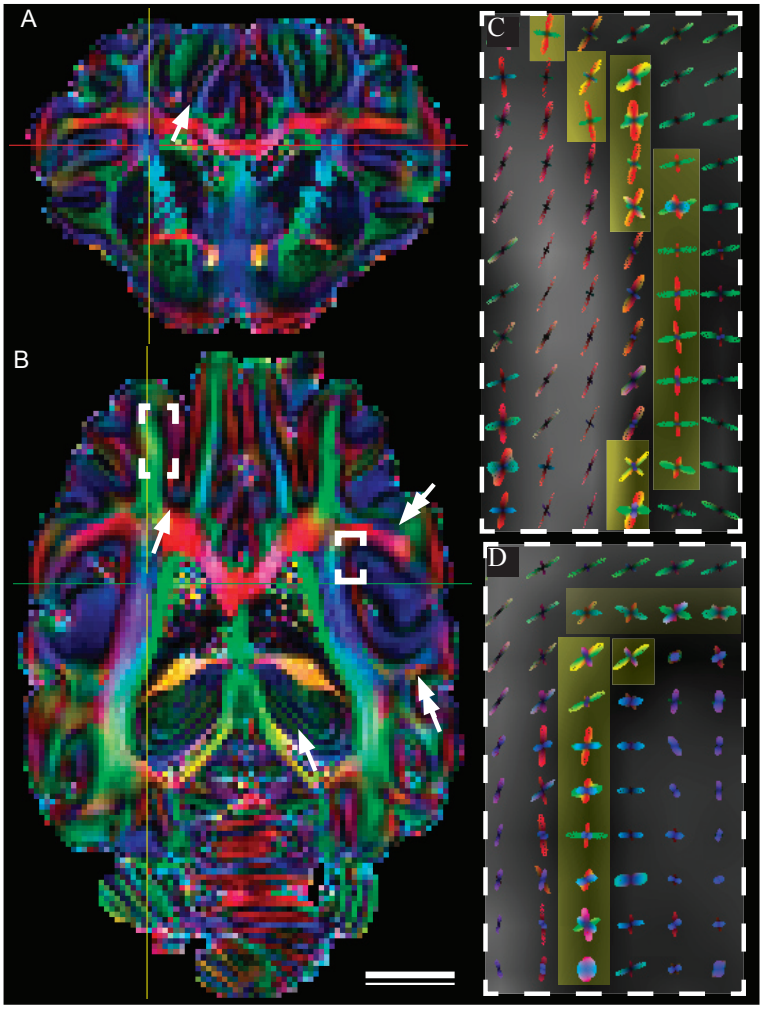

Figure 4 *Dyrby et al.*

5. R1_Dyrby_Figure_5
Click here to download 5. Figure: R1_Dyrby_Figure_5.pdf

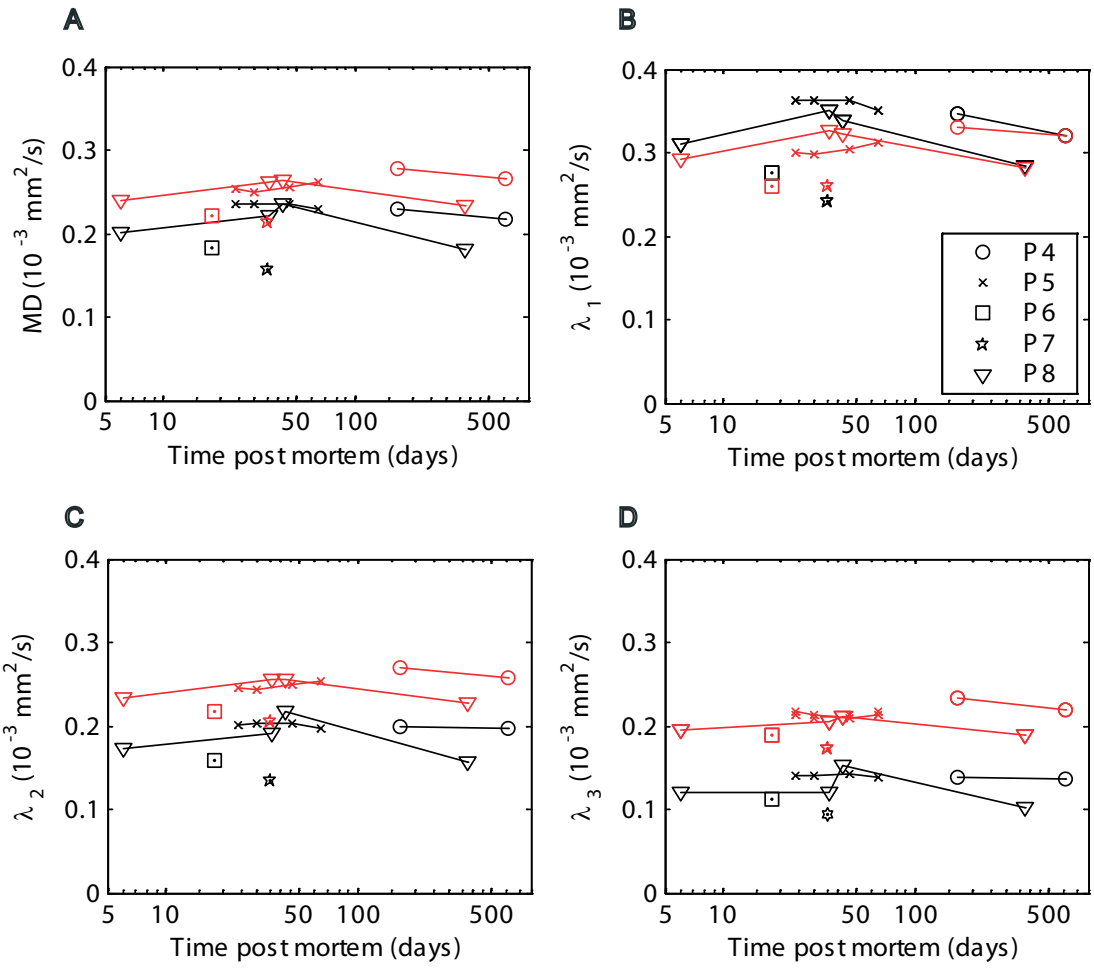

Figure 5 *Dyrby et al.*

Manuscript II

Dyrby TB., Søgaard LV., Parker GJM., Alexander DC., Lind NM., Hay-Schmidt A., Eriksen N., *Pakkenberg B., Paulson OB., Jelsing J. Validation of in vitro probabilistic tractography. Neuroimage. 2007 Oct 1;37(4):1267-1277. Epub 2007 Jul 10.

ELSEVIER

NeuroImage

www.elsevier.com/locate/ynimg
NeuroImage 37 (2007) 1267–1277

Validation of in vitro probabilistic tractography

Tim B. Dyrby,[a,b,j,*] Lise V. Søgaard,[a] Geoffrey J. Parker,[c] Daniel C. Alexander,[d] Nanna M. Lind,[e] William F.C. Baaré,[a] Anders Hay-Schmidt,[f] Nina Eriksen,[g] Bente Pakkenberg,[g] Olaf B. Paulson,[a,h] and Jacob Jelsing[g,i]

[a]*Danish Research Centre for Magnetic Resonance, Copenhagen University Hospital, Hvidovre, Denmark*
[b]*Intelligent Signal Processing Group, Informatics and Mathematical Modelling, Technical University of Denmark, Lyngby, Denmark*
[c]*Imaging Science and Biomedical Engineering, University of Manchester, Manchester, UK*
[d]*Centre for Medical Image Computing, Department of Computer Science, University College London, London, UK*
[e]*Department of Experimental Medicine, University of Copenhagen, Copenhagen, Denmark*
[f]*Department of Neuroscience and Pharmacology, University of Copenhagen, Copenhagen, Denmark*
[g]*Research Laboratory for Stereology and Neuroscience, Copenhagen University Hospital, Bispebjerg, Denmark*
[h]*Neurobiology Research Unit, Rigshospitalet, Copenhagen University Hospital, Copenhagen, Denmark*
[i]*Rheoscience, Rødovre, Denmark*
[j]*Memory Disorders Research Group, Department of Neurology, Rigshospitalet, Copenhagen University Hospital, Copenhagen, Denmark*

Received 1 May 2007; revised 21 June 2007; accepted 26 June 2007
Available online 10 July 2007

Diffusion weighted imaging (DWI) and tractography allow the non-invasive study of anatomical brain connectivity. However, a gold standard for validating tractography of complex connections is lacking. Using the porcine brain as a highly gyrated brain model, we quantitatively and qualitatively assessed the anatomical validity and reproducibility of in vitro multi-fiber probabilistic tractography against two invasive tracers: the histochemically detectable biotinylated dextran amine and manganese enhanced magnetic resonance imaging. Post mortem DWI was used to ensure that most of the sources known to degrade the anatomical accuracy of in vivo DWI did not influence the tracking results. We demonstrate that probabilistic tractography reliably detected specific pathways. Moreover, the applied model allowed identification of the limitations that are likely to appear in many of the current tractography methods. Nevertheless, we conclude that DWI tractography can be a precise tool in studying anatomical brain connectivity.

Keywords: Brain; Diffusion weighted imaging; Göttingen minipig; Manganese; Multi-fiber; Neuron tracing; Post mortem

Introduction

Detailed knowledge of the complex anatomical connections in the human central nervous system is pivotal in elucidating and understanding normal and pathological brain function. Our current understanding of the architecture of neuronal circuitry is mainly based upon histological visualization of fiber tracts or neuronal tracing techniques using fluorescent or histochemically detectable tracers (for a review see Kobbert et al., 2000; Oztas, 2003; Zaborszky et al., 2006). Additionally, a new magnetic resonance imaging (MRI) detectable neuronal tracing method has recently been introduced in animal models (Leergaard et al., 2003; Lin et al., 2001; Murayama et al., 2006; Pautler et al., 1998; Saleem et al., 2002). Manganese enhanced MRI (meMRI) exploits the anterograde transport of paramagnetic manganese (Mn^{2+}) and visualizes projection pathways in vivo (Pautler et al., 1998). However, although considered gold standards for assessing brain connectivity, the invasive nature of these techniques restricts their application to experimental animals or post mortem human brain research.

Recently, it has become possible to evaluate anatomical brain connectivity non-invasively by taking advantage of the restricted self-diffusion of water molecules within tissue using diffusion MRI, or diffusion weighted imaging (DWI). Diffusion tensor imaging (DTI) (Basser et al., 1994) and related methods such as q-ball imaging (Tuch, 2004), tensor-mixture models (Alexander, 2005; Assaf et al., 2004; Tuch et al., 2002), PASMRI (Jansons and Alexander, 2003) and spherical deconvolution (Frank, 2002; Tournier et al., 2004) quantify water-diffusion anisotropy in the intra and extra-cellular spaces of the neural environment. Fiber tracking algorithms then use the directions of greatest diffusion as estimates of white matter fiber orientation. Several fiber tracking algorithms have emerged in the last few years that provide reproducible visualizations of three-dimensional fiber tracts (Basser et al., 2000; Jiang et al., 2006; Parker et al., 2002, 2003). One class of these algorithms is probabilistic tractography (Behrens

* Corresponding author. Danish Research Centre for Magnetic Resonance, Copenhagen University Hospital, Hvidovre, Kettegaard Allé 30, DK-2650 Hvidovre, Denmark. Fax: +45 3647 0302.
E-mail address: timd@drcmr.dk (T.B. Dyrby).
Available online on ScienceDirect (www.sciencedirect.com).

1053-8119/$ - see front matter © 2007 Elsevier Inc. All rights reserved.
doi:10.1016/j.neuroimage.2007.06.022

et al., 2003; Parker et al., 2003; Parker and Alexander, 2003, 2005).

Although probabilistic tractography currently holds great promise as a powerful non-invasive connectivity-measurement tool, its accuracy and limitations remain to be evaluated. In particular, a strong correlation between the information about the anatomical connectivity provided by tractgraphy methods and independent anatomical data is still lacking (Behrens et al., 2007; Ciccarelli et al., 2003; Heiervang et al., 2006; Jones et al., 2005). Additionally, the accuracy and precision of tractography results are restricted by limitations on spatial resolution, thermal and physiological noise (for example cardiac pulsation (Skare and Andersson, 2001), respiration-induced signal fluctuations), brain motion and image artefacts (for a review see Le Bihan et al., 2006).

The present study aims to validate the anatomical accuracy of tractography by overcoming most of the known limitations. To this end probabilistic tractography was assessed post mortem in an in vitro environment. Post mortem imaging benefits from high-field (>3 T) MR scanners and long scanning times, thereby significantly improving the signal-to-noise ratio (SNR) and spatial resolution. Moreover, many of the degrading effects observed in vivo are not present post mortem. Specifically, we evaluated the ability of probabilistic tractography to reconstruct functionally specific pathways detected by invasive neuron tract tracing in the gyrated Göttingen minipig brain.

Materials and methods

Tracer injections

Three young male Göttingen minipigs (Ellegaard Göttingen Minipigs A/S, Dalmose, Denmark) were used in the study (age 3 months, weight between 5 and 6 kg). Each pig received a single simultaneous injection of 0.5 μl $MnCl_2$ (0.8 M $MnCl_2$ Tetrahydratem, Sigma-Aldrich, Denmark) and 4.5 μl biotinylated dextran amine (BDA, 10,000 molecular weight, Molecular Probes, Eugene, OR) aimed at the right somatosensory cortex (SC), the right prefrontal cortex (PFC), or the left motor cortex (MC) based on previously published anatomical findings (for a review see Lind et al. (2007)) The Göttingen minipigs were sacrificed at 2 weeks post-surgery. Brains were perfusion fixated in 4% paraformaldehyde (PFA), removed and post fixed in 1% PFA for at least 3 weeks. Following MR imaging protocols (see below) the brains were frozen on dry ice and cut into 100 μm coronal sections for histochemical analysis. Procedures for stereotaxic injections, anesthesia and immunohistochemical procedures have been described in detail elsewhere (Jelsing et al., 2006). All procedures followed guidelines for the care and use of experimental animals and were approved by the Danish Animal Experiments Inspectorate.

MRI and DWI scanning protocols

In vivo scanning was performed 2 days before and 2 days after injection of the tracers. The anesthetized pigs were placed in prone position in a Magnetom Trio (3 T) scanner (Siemens Medical Systems) with their head fixed in an 8 channel head coil. Structural images were acquired using a T_1-weighted magnetization prepared gradient echo (MPRAGE) sequence, which was sensitive to the paramagnetic tracer, manganese (TR=1580 ms, TE=3.93 ms, TI=800 ms, flip angle=9°, image matrix=256×256×256, voxel size=0.6×0.6×0.6 mm^3 and number of excitations (NEX)=3). At each session 16 MPRAGE scans were acquired.

In vitro scanning was performed using an experimental 4.7 T Varian Inova scanner. Two high resolution T_1-weighted structural images were obtained from the perfusion-fixed brains using an MPRAGE sequence (echo spacing=5.6 ms, TE=3 ms, TI=800 ms, flip angle=9°, image matrix=256×256×256, with a voxel size of 0.27×0.27×0.27 mm^3, NEX=12). DWI was performed using a diffusion weighted 2D single spin echo sequence (dwSE). Full brain coverage was achieved by acquiring two spatially interleaved data sets of 35 slices. Sequence parameters for each data set were: TR=6500 ms, TE=67.1 ms, slice thickness=0.5 mm, gap=0.5 mm, matrix=128×128, in-plane resolution=0.51×0.51 mm^2, diffusion sensitization gradient duration δ=27 ms, time between gradient-pulse onsets Δ=33.5 ms, gradient strength 56 mT/m, resulting in b=4009 s/mm^2. To avoid short-term instability of the brain tissue and for temperature equilibration, brains were placed in the scanner for a resting period of 15 h. The high b value was selected after testing several b values in their ability to detect crossing fibers using the method by Alexander et al. (2002). One full brain coverage DWI data set consisted of 3 non-diffusion weighted image volumes and 61 volumes with different gradient directions optimized as outlined in Jansons and Alexander (2003). Two full DWI data sets were acquired, generating a signal-to-noise ratio (SNR) of 27.

MRI post-processing

The mean (average of NEX=2) in vitro MPRAGE was co-registered to the non-diffusion weighted DWI volume using 6 degrees of freedom (*df*) with normalized mutual information. Next the mean in vitro MPRAGE image was re-sampled into two images, using a 6th order B-spline interpolation: one with the same resolution as the DWI image volumes and another with the original high resolution for visualization purposes. Co-registration and re-sampling for both in vivo and in vitro data were achieved using the routines implemented in SPM2 (Wellcome Department of Imaging Neuroscience www.fil.ion.ucl.ac.uk/spm).

The in vivo baseline MRI and meMRI images were co-registered and intensity normalized using the WM intensity of the cerebellum as mean reference (a region unaffected by manganese). For each injection site the significance of the manganese labeling was expressed as a *t*-map based on a voxel-wise Bonferroni-corrected Student's *t*-test between the intensity normalized co-registered baseline and the meMRI images. In order to calculate an overlap fraction (see below) across the three brains, the *t*-maps were warped into the in vitro DWI image space of each brain giving a total of 9 *t*-maps. The mean in vivo baseline MPRAGE image was co-registered, using a 12 *df* affine transformation and mutual information, to a mean in vitro MPRAGE image (that was co-registered into DWI image space). Subsequently, high dimensional warping, as implemented in the deformation toolbox in SPM2, was used to calculate a deformation field describing the non-linear warping from the in vivo MR image space to the in vitro DWI image space. *t*-maps were finally re-sampled into in vitro DWI image space by applying the affine (12 *df* co-registration) and non-linear (high dimensional deformation field) transformations.

Probabilistic tractography

A multi-tensor model was fitted in each voxel in the DWI data set modeling the anisotropy of either a single or a crossing fiber

situation defined by the voxel classification algorithm by Alexander et al. (2002). Next, the probabilistic index of connectivity (PICo) algorithm (Parker et al., 2003; Parker and Alexander, 2003; Parker and Alexander, 2005) as implemented in the Camino diffusion MRI toolkit (http://www.cs.ucl.ac.uk/research/medic/camino/) (Cook, 2006) was used for tracing fibers originating from the different projection sites (e.g. seed regions). Waypoint regions were used to constrain the probabilistic tractography method to include only fiber tracts entering/passing such a waypoint region. Default setup parameters were used (non-interpolated tracking using a modified FACT method (Mori et al., 1999)) with the exception that 64,000 streamline processes were applied for identifying connection routes from each voxel in a seed region. Stopping criteria prevented biologically implausible curvature of streamlines (>80° within a single voxel) or attempts to transit non-brain voxels. The number of occasions within the 64,000 repetitions at which each voxel was crossed by a streamline was used to define a map of the probability connection to the seed voxel. A probabilistic connectivity index (Pc) map representing fiber tracts emanating from a seed region was then created by averaging all the individual maps within the seed region.

Seed and waypoint regions were drawn manually on the non-diffusion weighted MRI scan with guidance from the mean in vitro MPRAGE image and the thresholded (warped) *t*-maps. Regions were drawn using the MIPAV program (http://www.mipav.cit.nih.gov) and included both white matter (WM) and cortical gray matter (GM) voxels. Waypoint regions were used to constrain the probabilistic tractography method to include only specific fiber tracts entering/passing such a waypoint region. From the in vivo tracer experiment, three specific fiber tracts were individually tracked by probabilistic tractography: the contralateral corticocortical, corticothalamic and the corticonigral fiber tracts. Two waypoint regions were drawn in the corpus callosum (CC) for extracting contralateral corticocortical projections: one including the genu and the rostrum of CC (tracts seeded from the SC or PFC) and another including the body of CC (tracts seeded from MC). For extracting corticothalamic fiber tracts, a waypoint region was drawn in three thalamic nuclei: the ventral posterior (VP), the mediodorsal (MD) and the ventral anterior/ventral lateral (VA/VL) in correspondence with the seed regions for SC, PFC and MC. Finally, for extracting corticonigral fiber tracts, a broad waypoint region cross-sectioning fibers in the cerebral peduncle was drawn at the entrance of the nucleus substantia nigra (SN).

Tractography results for each seed region were summed to facilitate an anatomical description of the three fiber tracts.

Quantitative tractography

An overlap fraction (OF) (Anbeek et al., 2004) was used to obtain a quantitative measure describing the spatial agreement between projections detected by manganese labeling and tractography. The OF is a voxel-based analysis expressing the overlap fraction between two binary regions of interest (ROI)—a target and a reference ROI.

$$\mathrm{OF} = \frac{V_{\mathrm{Target}\cap\mathrm{Reference}}}{V_{\mathrm{Reference}}} \qquad \mathrm{OF} = [0:1] \tag{1}$$

The numerator expresses the volume of intersection between the reference and target ROI and is normalized by the volume of the reference ROI in the denominator. The target ROIs representing manganese labeling were the *t*-maps warped into in vitro DWI space. Warped *t*-maps were thresholded in such a way that the longest projection of interest appeared dense and continuous between injection and projection site. Thresholds for each injection site were $t>30$, $t>8$ and $t>14$ for SC, PFC and MC respectively. The reference ROI comprised of fiber tracts thresholded at $\mathrm{Pc}\geq 4\%$. As a thresholded manganese pathway comprises a broad region in the brain, the highest sensitivity of the OF was guaranteed by using the tractography ROI as the reference.

Results

In vivo tracing

Pathways emanating from the simultaneous injection of two in vivo tracers in the right SC of brain 1, in the right PFC of brain 2 or in the left MC of brain 3 were described anatomically and compared. Injections of BDA into the SC of brain 1 (Fig. 1A) revealed several specific ipsilateral and contralateral corticothalamic, corticostriatal and corticocortical pathways. Dense corticothalamic innervations were observed in the ipsilateral VP nuclei of the thalamus (Figs. 1B, C, F, G). Other fibers were directed towards the SN and the midbrain superior colliculi (Figs. 1H–J). From the injection site a dense aggregation of fibers was observed in the internal capsule. Some of these fibers terminated in the putamen (Fig. 1E) or were directed ventrocaudally towards the ventral parts of the basal ganglia. Besides the dense reciprocal projections to the thalamus (Fig. 1C), fibers also passed the zona incerta and the subthalamic nucleus. Further caudally, projections went through the cerebral peduncle towards the SN (Figs. 1G, H) eventually crossing the mesencephalon with a dense aggregation of terminals in the intermediate layers of the superior colliculus (Figs. 1I, J). Contralateral pathways from the SC were observed heading towards the SC (Fig. 1D) and the putamen whereas the density of fibers in the contralateral thalamus VP and SN was indistinct and sparse.

The corresponding pathways visualized by the manganese injected into the SC are shown in Fig. 2. In general, the manganese tracer terminated in brain regions corresponding to those identified with BDA. The most significant manganese-induced signal (Fig. 2A) was observed at the cortical injection site; the relatively large size of this area was likely to be due to a local cortical transport or extra cellular diffusion of manganese. From the injection site, the main pathway passed through the ipsilateral superior frontal gyrus towards the genu of the corpus callosum (Figs. 2A, B) where the path split into ipsilateral and contralateral tracts. The contralateral tract crossed the genu of the corpus callosum towards the contralateral SC (Figs. 2A, B, G). The ipsilateral tract traversed the internal capsule (Figs. 2B, H), eventually merging in a large ventral striatal area including globus pallidus and parts of the putamen (Figs. 2C, D, H, I). This area consisted of a number of segregated pathways probably representing both direct and indirect (transsynaptic) tracts. At this level manganese was segregated into a corticothalamic and a corticonigral tract (Fig. 2D). The corticothalamic pathway crossed the internal capsule before entering the ventral part of the thalamus (Fig. 2D). The path turned dorsolaterally and ended in the medial and lateral subdivision of the VP nuclei (Figs. 2E, I). A significant labeling of the ventral part of the MD nucleus of the thalamus was also observed (Fig. 2E). The corticonigral trace developed from the

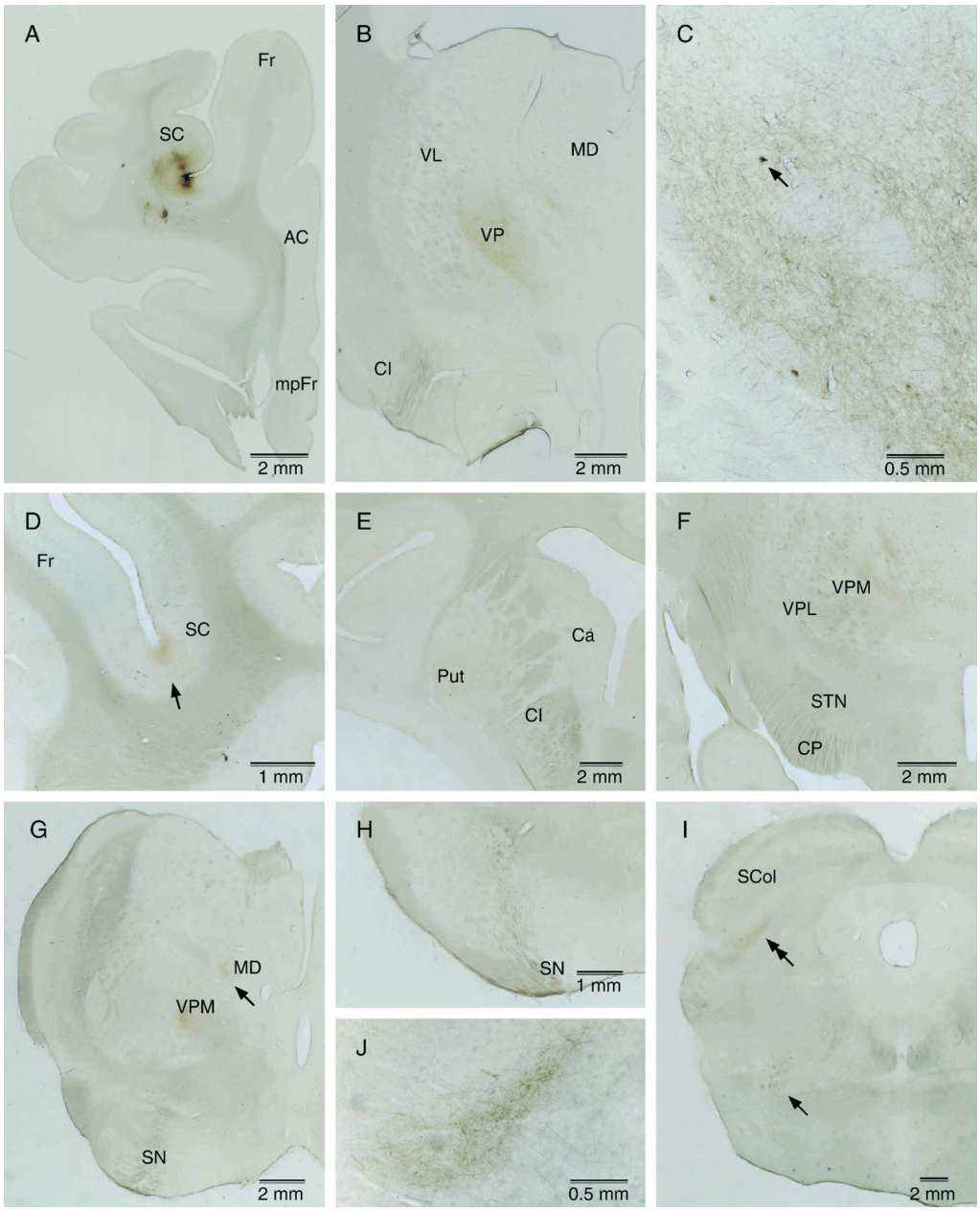

Fig. 1. Histological tracing from the SC of the Göttingen minipig brain (brain 1; coronal section plane). The right side of the brain is depicted in the left side of the figures. Injections into the right SC (A) revealed a dense number of reciprocal connections with the VP nuclei of the thalamus (B, C), including the medial (VPM) and lateral (VPL) subdivisions (F, G), as well as parts of the MD (G, arrow). BDA was transported reciprocally showing both anterograde-labeled terminals and retrograde-labeled perikarya (C, arrow). Corticocortical pathways were observed in the contralateral SC (D, arrow), whereas ipsilateral pathways were observed innervating the putamen (Put) (E), the subthalamic nucleus (STN) and the SN (G, H), and more caudally traversing the mesencephalon (I, arrow) to terminate in the intermediate layers of the superior colliculus (SCol) (I, J, double arrow). Abbr.: AC, anterior cingulate cortex; Ca, caudate nucleus; CI, capsula interna; CP, cerebral peduncle; Fr, frontal cortex; mpFr, mediopolar frontal cortex.

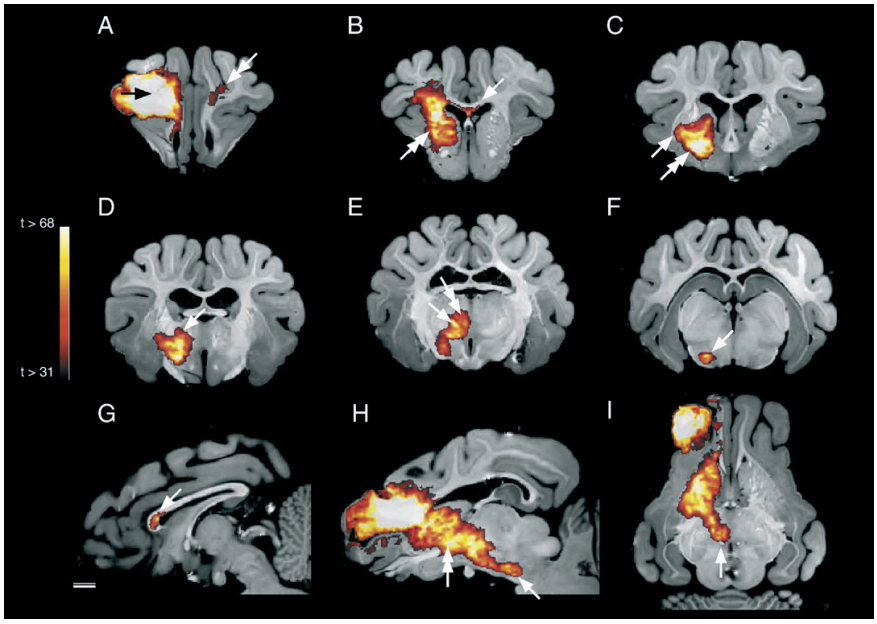

Fig. 2. In vivo tracing using manganese injected into the right SC of brain 1. Pathways of the manganese labeling are represented by the statistical *t*-map (color bar) visualized on the high resolution in vitro MPRAGE MRI seen in coronal (A–F), sagittal (G, H) or horizontal section plane (I). The right side of the brain is depicted in the left side of the figures. The frontal injection site in the SC (A, arrow) with corticocortical pathway towards the contralateral SC (A, double arrow) is seen crossing through the genu of the corpus callosum (B, G, arrow). Ipsilaterally, manganese is seen in the internal capsule (B, H, double arrow), parts of the putamen (C, arrow) as well as the pallidum (C, double arrow). Several segregated pathways were observed; one pathway enters the ventral thalamus (D, arrow) with manganese labeling in the VP (E, I arrow), as well as parts of the MD nucleus of the thalamus (E, double arrow). Another pathway was detected more ventrally oriented towards the subthalamic nucleus (E) and the SN (F, H, arrow). Scale bar = 5 mm.

ventral striatum caudally along the internal capsule and cerebral peduncle towards the SN (Figs. 2E, F, H). Moreover, part of this corticonigral tract seemed to terminate in the subthalamic nucleus (Fig. 2E) and in the intermediate layers of the superior colliculus of the midbrain (not shown). At these caudal levels, the manganese signal became weaker and the tracer deposit in the superior colliculus was evident only when decreasing the threshold level of significance of the *t*-test to $t>8$. Besides the corticocortical transport of manganese in the contralateral SC, manganese was conveyed contralaterally through the basal ganglia towards the SN with a lower threshold of $t>7.9$ (p-value<0.01) (not shown). It was not possible to unambiguously discriminate indirect transsynaptic tracts originating from the manganese deposits in the putamen (see Discussion).

A high correspondence in labeled pathways was also observed for BDA and manganese injected into the PFC (brain 2) and the MC (brain 3). Evaluation of BDA injected into the left lateral and medial subdivision of the mediopolar PFC revealed a clear and dense reciprocal corticothalamic pathway to the medial part of the thalamic MD nucleus. A dense aggregation of fibers and terminals was also observed in the caudate nucleus, whereas projections towards the SN were fewer. Moreover, a clear pathway to the contralateral MD nucleus was evident. In comparison, manganese was seen following ipsilateral corticothalamic and corticonigral pathways as well as discrete corticocortical pathways passing through the rostrum of corpus callosum to the contralateral PFC (Figs. 3A, E, G). The labeling of manganese went through the medial part of the internal capsule and terminated in the caudate nucleus or accumulated in the medioventral part of the internal capsule ($t>26$; Figs. 3B, F). The deposit of manganese in this ventral region was not as dense and widespread as observed for SC and did not include the pallidum. Two tracts could be discerned: a medial corticothalamic pathway directed towards and ending in the MD nucleus (Figs. 3C, E, G) and a more ventral corticonigral pathway terminating in the SN (Figs. 3D, F). Additionally, and in accordance with the ipsilateral tracts, manganese passed through the basal ganglia towards the SN (Fig. 3B) and the contralateral MD nucleus when decreasing thresholds for statistical significance ($t>6.7$, not shown).

BDA injections into the MC (not shown) revealed not as distinct terminals in the VA/VL nucleus of the thalamus as observed for the MD projection (Fig. 1). The indistinct detection of terminals might be related to an inferior histological quality due to tissue freezing artefacts observed in this animal only. A corresponding pattern was observed for manganese following a direct pathway through the dorsal parts of the internal capsule (Figs. 3H–J). A significant accumulation of manganese was also observed in the caudate nucleus (Fig. 3J), whereas pathways to the SN were neither clearly visible by BDA nor reliably detected by manganese (uncertain and noisy at very low threshold). Corticocortical pathways were observed for manganese in the contralateral MC (Fig. 3H).

Projections observed with the two in vivo tracers are summarized and illustrated schematically in Fig. 4.

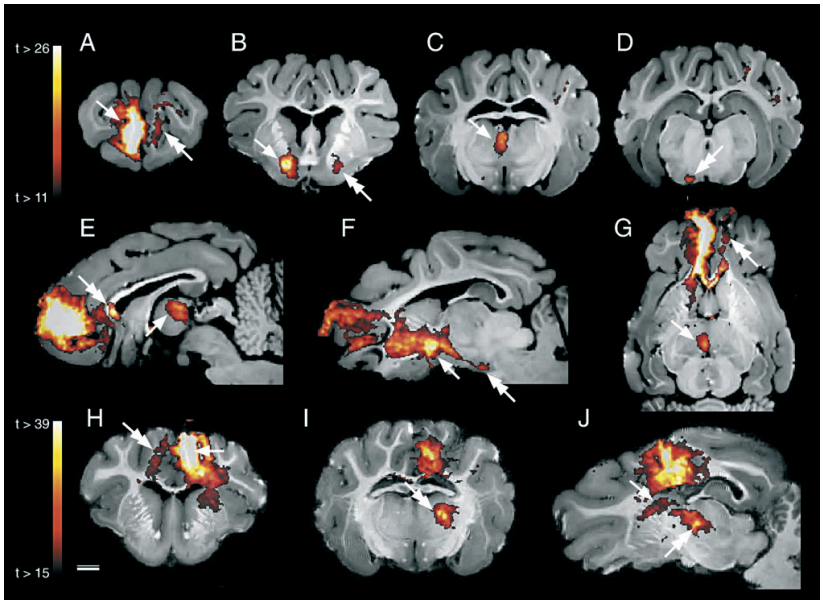

Fig. 3. In vivo tracing using manganese injected into the right PFC of brain 2 (A–G) and the left MC of brain 3 (H–J). Pathways of the manganese labeling are represented by the statistical *t*-maps (color bar) visualized on the high resolution in vitro MPRAGE MRI seen in coronal (A–D, H, I), sagittal (E, F, J) or horizontal section plane (G). The right side of the brain is depicted in the left side of the figures. Injections into the PFC (A, arrow) revealed a corticocortical pathway to the contralateral PFC (A, G, double arrow) crossing through the rostrum of the corpus callosum (E, double arrow). Ipsilateral labeling of manganese was observed passing through the internal capsule depositing ventrally in a high intensity ventral area (B, F, arrow) as well as contralaterally (B, double arrow). More caudally, this region splits into at least two distinct pathways; one passes through the ventral thalamus eventually entering the MD nucleus (C, E, G, arrow), while another pathway is directed ventrally towards the SN (D, F, double arrow). Manganese injected into the MC (H, arrow) projects to the contralateral MC (H, double arrow) via the body of corpus callosum, as well as to the caudate (J, arrow) and the VA and VL nuclei of the thalamus (I, J, double arrow). Scale bar = 5 mm.

In vitro tractography

For each brain, fiber tracking was initiated in seed regions located at the tracer injection site e.g. the right SC for brain 1, the right PFC in brain 2 and the left MC in brain 3. Unless otherwise stated, probabilistic tractography was constrained by means of waypoint regions to individually track the three main fiber tracts identified by BDA and manganese: a corticothalamic, a corticonigral and a contralateral corticocortical fiber tract (see Figs. 1–3). The correspondence between resulting probabilistic fiber tracts and manganese labeled pathways was quantitatively assessed using an OF (Table 1). Only probabilistic fiber tracts for the SC are presented here (Fig. 5).

Probabilistic tractography seeded in the SC was able to reconstruct several segregated fiber tracts passing through the dorsal and medial part of the internal capsule towards the ventral thalamus and the SN (Figs. 5A–E). In high agreement with manganese the corticothalamic fiber tract entered the ventral part of

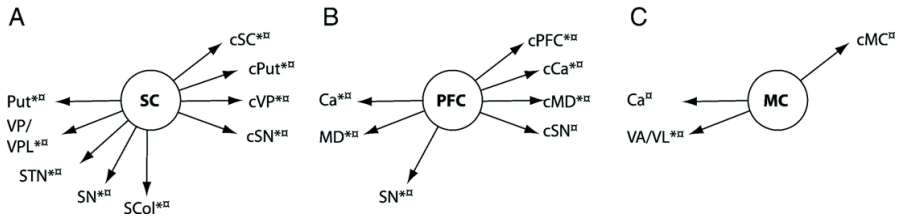

Fig. 4. Schematic illustration of the projection sites that could be detected by the two in vivo tracers, BDA (*) and manganese, when injected into the right SC, the right PFC or the left MC. Contralateral projection sites are abbreviated with the prefix "c". (A) Injection into the SC of brain 1 revealed ipsilateral projections toward: putamen (Put), ventral posterior (VP) and ventral posterior lateral (VPL) nucleus of thalamus, subthalamic nuclei (STN), substantia nigra (SN) and the superior colliculus (SCol). Contralateral projections were observed towards: cSC, cPut, cVP and cSN. (B) Injection into the PFC of brain 2 revealed ipsilateral projections toward: caudate (Ca), medial dorsal (MD) nucleus of thalamus and SN, whereas the contralateral projections were observed towards: cPFC, cCa, cMD and cSN. (C) Injection into the MC of brain 3 revealed ipsilateral projections towards: Ca, and the ventral anterior (VA) and the ventral lateral (VL) nucleus of thalamus. The only contralateral projection observed was that towards the MC.

Table 1
The spatial agreement between the thresholded probabilistic fiber tracts and the thresholded manganese *t*-maps is expressed by an overlap fraction (OF)

Fiber tracts	Somatosensory cortex (SC)			Prefrontal cortex (PFC)			Motor cortex (MC)		
	Brain 1	Brain 2	Brain 3	Brain 1	Brain 2	Brain 3	Brain 1	Brain 2	Brain 3
Corticocortical	0.66	0.67	0.70	0.94	0.96	0.98	0.63	0.75	0.59
Corticothalamic	0.63	0.91	0.93	NC	0.63	0.58	0.89	0.79	NC
Corticonigral	0.87	0.74	0.92	0.84	0.75	0.69	–	–	–

Fiber tracts not found by probabilistic tractography are abbreviated NC (no connection). Corticonigral fiber tracts seeded in MC were not investigated since they could not be reliably detected by the in vivo tracers.

the thalamus (Fig. 5D) turning dorsolaterally toward the VP nucleus (Figs. 5E, I). However, in contrast to manganese, the probabilistic fiber tract continued towards the periventricular part of the third ventricle, eventually joining fiber tracts emanating from the contralateral hemisphere (Figs. 5E, G). This discrepancy resulted in a relatively low OF (0.63) (Table 1, SC). The comparatively low OF (0.66) seen for the contralateral corticocortical connections could be attributed to differences at the level of the genu of the corpus callosum where fiber tracts traversed more dorsally than those identified by the manganese (Figs. 2G, 5G). Eventually, these fiber tracts terminated in the contralateral PFC rather than the contralateral SC (Figs. 1D, 2A, 5A).

A high agreement (OF=0.87, Table 1, SC) was observed for the direct corticonigral fiber tracts passing through the internal capsule and cerebral peduncle towards the SN (Figs. 5F, H). However, minor discrepancies were found close to the SN where two fiber tracts were situated more dorsally than were seen with manganese. One of the fiber tracts seemed to terminate in the SN, whereas the other seemed to pass around SN before finally extending caudally in a seemingly alternative fiber tract (Fig. 5H). The latter tract ended when the probabilistic connectivity index decreased below the threshold for visualization (Pc<4%). Due to the constraining of probabilistic tractography by means of waypoint regions, no fiber tracts were observed towards the putamen or the ventral pallidal area (Fig. 5C) as observed for the in vivo tracers (Figs. 1E, 2C). However, corticopallidal fiber tracts were detectable when using unconstrained probabilistic tractography (not shown).

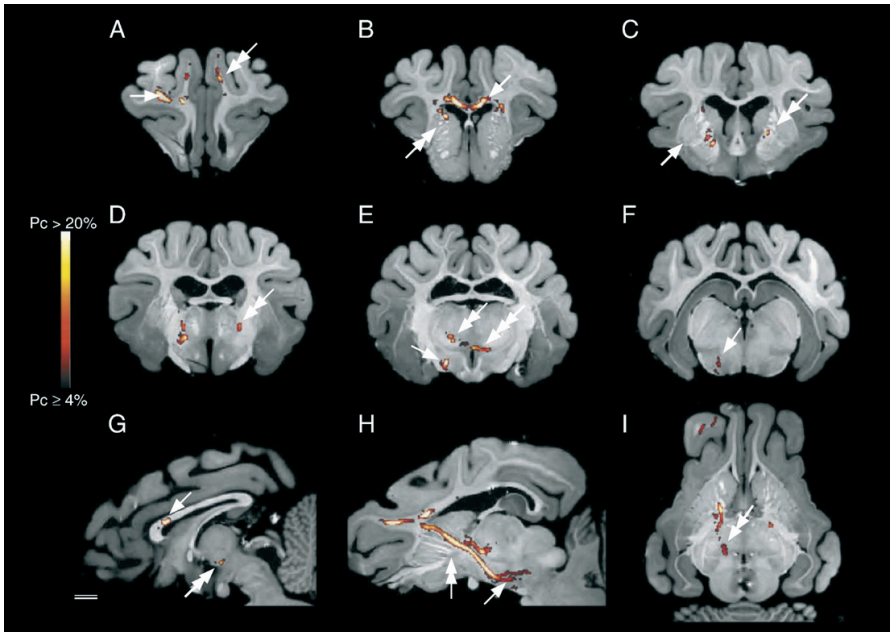

Fig. 5. In vitro probabilistic tractography seeded in the right SC of brain 1 and constrained using waypoint regions. The (probabilistic) fiber tracts are overlaid on the high resolution in vitro MPRAGE MRI seen in coronal (A–F), sagittal (G, H) or horizontal section plane (I). The right side of the brain is depicted in the left side of the figures. The color bar represents the probabilistic connectivity index of the fiber tracts. Tractography from the SC (A, arrow) revealed a fiber tract towards the contralateral PFC (A, double arrow) and SC crossing through the caudal part of the genu of the pallidum (G, arrow). Ipsilaterally, several segregated fiber tracts were observed passing through the medial and dorsal part of the capsula interna (B, H, double arrow). Tractography did not include the putamen (C, arrow) or the pallidum. Tractography entered the rostral part of the thalamus and eventually the VP and VPL nuclei (E, I, double arrow) before continuing (E, triple arrow) onto the contralateral hemisphere (C, D, G double arrow). Other fiber tracts were directed towards the SN (E, F, H arrow) or further caudally along an alternative fiber tract. Scale bar = 5 mm.

In agreement with manganese labeled pathways, probabilistic tractography seeded in the PFC revealed several segregated fiber tracts passing through the medial and ventral parts of the internal capsule (not shown). However, as indicated by the relatively low OFs (0.63; Table 1, PFC) inconsistencies were also apparent. Indeed, corticothalamic fiber tracts were restricted to the dorsomedial part of the capsula interna passing towards the ventral part of the thalamus. Moreover, a small portion of this tract split off, turned dorsolaterally towards the MD nucleus and terminated in the intralaminar central lateral nucleus instead of entering the MD nucleus. In addition, another corticothalamic fiber tract, not seen with manganese, processed in a dorsorostral loop-like fashion towards the stria medullaris, eventually entering the caudal part of the MD nucleus. Probabilistic tractography seeded in the MC did not reveal the corticothalamic pathways observed with the two in vivo tracers.

The corticonigral fiber tracts emanating from the PFC passed through the rostral part of the pallidum towards the SN and segregated into several fiber tracts close to the SN. In contrast to the corticonigral fiber tract seeded in the SC, none of the fiber tracts terminated in the SN but continued caudally in a seemingly alternative fiber tract (OF = 0.75, Table 1, PFC). The corticocortical fiber tract towards the contralateral PFC was found to be nearly identical to the pathway labeled by manganese (OF = 0.96). In contrast, when seeded in the MC, the OF for the corticocortical fiber tract towards the contralateral MC was low (OF = 0.59; Table 1, MC). With respect to the latter, the major difference between

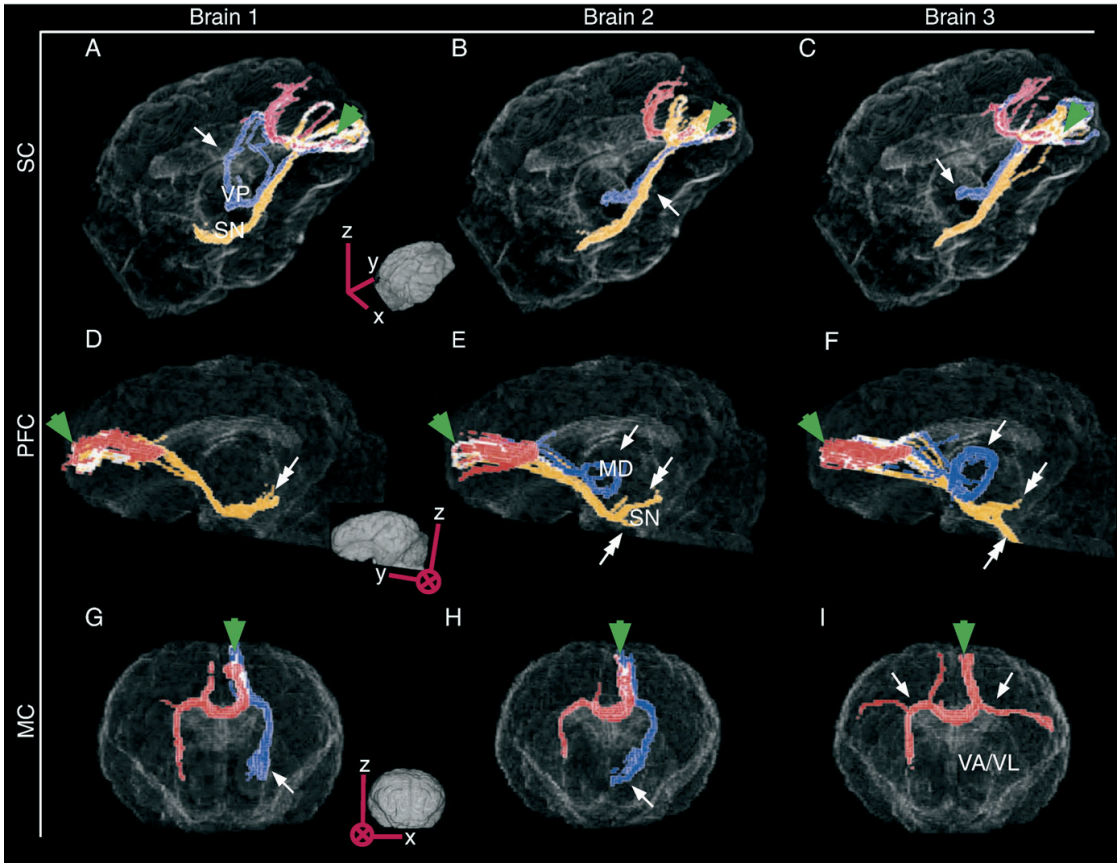

Fig. 6. Reproducibility of in vitro probabilistic tractography was visualized across the three Göttingen minipig brains (brain 1, left column; brain 2, center column; brain 3, right column). Seed regions were placed in all three brains (green arrow): SC (A–C), PFC (D–F) and MC (G–I). Brains that received the original injection of the in vivo tracers are visualized in panels A, E and I. The contralateral corticocortical (red), corticothalamic (blue) and corticonigral (orange) (probabilistic) fiber tracts were traced using waypoint regions then thresholded (Pc ≥ 4%) and visualized on a glass (pig) brain. Voxels containing two or more fiber tracts are shown in white. Contralateral corticocortical fiber tracts were consistently reproduced among brains (A–I). The segregation of fibers in the region of the centrum semiovale was also consistent (e.g. I, arrow). Probabilistic tractography encountered problems terminating in the thalamic MD and VA/VL nuclei (E–H, arrow), but not for the VP nucleus (B, C, arrow). However, an "ongoing" corticothalamic fiber tract from the VP can be seen in panel A (arrow). No corticothalamic fiber tract was detected in panels D and I. Minor differences are seen in the corticonigral fiber tracts passing through the internal capsule (e.g. B, arrow). All the corticonigral fiber tracts had problems terminating in SN. This is clearly visible when injected in the PFC (D–F, double arrows). The corticonigral fiber tract seeded in MC was not investigated (G–I).

manganese and probabilistic tractography occurred in the centrum semiovale, a highly heterogeneous white matter region, where callosal and corona radiata fibers congregate. In this region fiber tracts seeded in the MC split into two tracts: one directed towards the contralateral MC and another directed towards the contralateral striatum. The latter was not seen with manganese labeling.

Reproducibility

The reproducibility of the probabilistic tractography was assessed by tracking fibers seeded in the SC, PFC and MC in each of the three pig brains. An overlap fraction (Table 1) was then used to quantify the correspondence of the manganese tracer among the three brains for three predetermined fiber tracts: the corticothalamic, the corticonigral and the contralateral corticocortical tracts (Fig. 6).

Probabilistic tractography encountered problems when tracing corticothalamic projections emanating from PFC and MC towards the thalamic MD and VA/VL nuclei (Figs. 6D–I, blue). Indeed, no corticothalamic fiber tract was detected in brain 1 or brain 3 when seeded in the PFC or MC, respectively (Figs. 6D, I). Moreover, when seeded in PFC, differences in the fiber tracts between brain 2 and brain 3 were observed in the region of internal capsule and in the way they terminated in a loop-like fashion in thalamus (Figs. 6E, F). Finally, the corticothalamic fiber tracts emanating from MC towards the thalamus followed the same fiber tract in brain 1 and brain 2 with a minor variation of 6% of the mean OF (Mean OF was calculated on all the three brains). However, instead of entering VA/VL nuclei they continued ventrally around the thalamus (Figs. 6G, H, blue).

In contrast to PFC and MC, probabilistic tractography from SC to the thalamic nuclei VP encountered no problems in any of the three brains (Figs. 6A–C). Nevertheless, the ongoing corticothalamic fiber tract in brain 1 that crossed the diencephalon to the contralateral hemisphere (Fig. 6A) was not evident in the two other brains (Figs. 6B, C) leading to OFs of 0.91 and 0.93 in brains 2–3 as opposed to 0.63 in brain 1 (Table 1, SC).

Corticonigral fiber tracts originating in the SC and PFC were found in all three brains (Fig. 6, orange). Minor deviations between fiber tracts were restricted to the internal capsule (Figs. 6B, F). The corticonigral fiber tract observed from the SC and seemly terminating in SN in brain 1 was not reproduced in brain 2 or 3 (Figs. 6A–C). None of the corticonigral fiber tracts emanating from PFC towards the SN terminated in the manner observed with the in vivo tracers, but instead they continued caudally in alternative fiber tracts as previously described (Figs. 6D–F).

Contralateral corticocortical fiber tracts (Fig. 6, red) were consistently reproduced in all three brains. When seeded in the SC or PFC, we observed an interbrain variation in the contralateral corticocortical fiber tracts of less than 3.5% in the mean OF (Figs. 6A–C, D–F). Nonetheless, a large difference was found when comparing the two mean OFs when seeded in SC (0.68) or in PFC (0.96) (Table 1, SC, PFC). In contrast, a high interbrain variation of 14% was found for the contralateral corticocortical fiber tract when seeded in MC, probably related to the discrepancies between fiber tracts in the region of the centrum semiovale (Figs. 6G–I).

Discussion

In the present study the porcine brain was used as a gyrated brain model in order to quantitatively and qualitatively assess the anatomical validity, consistency and reliability of in vitro probabilistic tractography. Previous validation studies of tractography methods have been based on e.g. simulations (Lazar and Alexander, 2003; Leemans et al., 2005) or groups of human subjects (Behrens et al., 2007; Ciccarelli et al., 2003; Heiervang et al., 2006). Using the porcine brain we demonstrate that the multi-fiber probabilistic tractography method used in the present study is able to reconstruct fiber tracts comparable to projection pathways obtained using two invasive tracers: the histology tracer BDA and the MRI detectable paramagnetic contrast agent manganese. The simultaneous injection of the two in vivo tracers allowed the identification of distinct functionally organized neural networks with high accuracy and confidence (Alexander et al., 1986, 1990; Groenewegen et al., 1997) and provided the indispensable independent anatomical data for validating tractography results. In agreement with the invasive tracers, probabilistic tractography identified three specific fiber tracts for each of the three cortical injection sites: a corticothalamic, a corticonigral and a contralateral corticocortical fiber tract. Moreover, the results allowed us to identify limitations that are likely to be typical of many available tractography methods.

The consistency between the two tracers was in general high though differences were observed in projection pathways involving the striatum and pallidum. The putamen is known to receive afferents from motor and somatosensory areas, whereas the caudate nucleus is innervated mainly by associative prefrontal cortical connections (Selemon and Goldman-Rakic, 1985). Except for the MC, these direct projections were apparent using both tracers in the Göttingen minipig brain. However, the highly significant labeling of the ventral pallidal area observed for manganese injected into the SC, but not for BDA, indicates a further transport and transsynaptic capacity for manganese in agreement with previous studies (Murayama et al., 2006; Pautler, 2004; Saleem et al., 2002). The transsynaptic capacity of manganese may in principle affect the ability to validate tractography against meMRI as tractography generally has difficulties in tracking fibers through such relay regions. However, as the three specific fiber tracts used for validation did not include these areas we did not find any evidence that this might be the case.

The use of post mortem DWI data sets is pivotal in evaluating the probabilistic tractography method (or any other tractography method for that matter) as it overcomes most of the sources known to degrade in vivo DWI, such as low SNR, and motion and image artefacts (Le Bihan et al., 2006; Lori et al., 2002). The problems encountered by the multi-fiber probabilistic tractography method are therefore likely to be related to limitations of the tractography method itself rather than the quality of the DWI data sets. An obvious exception to the latter assertion is image resolution. Indeed, the smaller the image voxels are, the better one can in principal model the often complex composition of fibers within a voxel (e.g. crossing fibers). However, decreasing the voxel size would be at the expense of a lower SNR. The post mortem DWI data set used in the present study had 0.5 mm isotropic voxels which, given the volume of the pig brain, is comparable to 1.7 mm isotropic voxels in the human brain. As such, tractography findings in the current study correspond to what one might expect to find in clinical human DWI data sets.

Although the probabilistic fiber tracts generally agreed with those labeled by the two in vivo tracers, the tractography method had

difficulties in identifying terminating fiber tracts in the SN or thalamus. Often fiber tracts were observed to continue. One of the reasons for the uncertainty in identifying termination in a nucleus might be related to a GM–WM partial volume effect (PVE), which often appears at the border of a nucleus where high diffusion anisotropy from WM mixes with low anisotropy from the GM in the nucleus. Increasing the image resolution might diminish the "termination" problem as it reduces the PVE. Alternatively, although not yet proven, more advanced models such as q-ball imaging (Tuch, 2004) or PAS-MRI (Jansons and Alexander, 2003) might be able to reduce PVE related problems.

We also observed that the probabilistic fiber tracts do not always follow the same pathways as the in vivo tracers. For example, alternative fiber tracts were seen in the region of the centrum semiovale when the tractography was seeded in the MC. It might be erroneous to label these alternative fiber tracts as false positives beforehand because diffusion has multidirectional properties, in contrast to both of the in vivo tracers which only visualize anterograde projections. However, since the centrum semiovale is known to be a region where tractography has problems (Jones et al., 2005), the likelihood of observing a false positive tract in this region may be higher than finding a direct fiber tract undetected by the in vivo tracers. Nevertheless, the same "false positive" fiber tract was consistently observed across the three pig brains, with only minor OF differences. Similarly, false positive fiber tracts were recognized for SC seeded corticocortical fiber tracts. Overall, these findings underline the fact that inter-subject agreement for a particular fiber tract is not necessarily a gold standard for the validity of tractography methodologies. Instead, they are likely to be merely an indication of the consistency by which the tractography method, in combination with the DWI data set used, tracks fibers. As with the PVE problem discussed above, more advanced models of fiber orientations may increase the accuracy and precision of the fiber orientation estimates required for tractography and reduce some of the observed discrepancies between tractography and tracers.

In conclusion, we demonstrate that the combination of in vivo tracers and a post mortem DWI data set provides a unique way for testing fiber models and tractography methods. Our results substantiate that the use of independent anatomical data such as invasive tracers is pivotal for the validation and continuous refinement of existing and future (probabilistic) tractography methods. As such we hope that the anatomical model developed in the present study will contribute to in vivo tractography realizing its full potential within the human brain in the near future.

Acknowledgments

We thank Matthew G. Liptrot, MSc and Torben Lund, MSc PhD for critical technical input and Birgitte R. Kornum, MSc for assisting during surgery. Thanks to Dr. Klaus Qvortrup and Dr. Maibritt B. Andersen for placing perfusion and stereotaxic equipment at our disposal. Thanks to DVM Nanna Grand and Lars Ellegaard at Ellegaard Minipigs Aps for donating experimental animals. We would like to express our gratitude for the financial support from the Lundbeck Foundation, the Gangsted Foundation, the Danish Centre for Scientific Computing grant no. HDW-1104-08 and the Velux Foundation. GJMP is supported by the BBSRC, MRC and EPSRC in the United Kingdom, under grant numbers BB/E002226/1, G0501632 and GR/TO2669/01, respectively.

References

Alexander, D.C., 2005. Multiple-fibre reconstruction algorithms for diffusion MRI. Ann. N. Y. Acad. Sci. 1064, 113–133.

Alexander, G.E., DeLong, M.R., Strick, P.L., 1986. Parallel organization of functionally segregated circuits linking basal ganglia and cortex. Annu. Rev. Neurosci. 9, 357–381.

Alexander, G.E., Crutcher, M.D., DeLong, M.R., 1990. Basal ganglia–thalamocortical circuits: parallel substrates for motor, oculomotor, "prefrontal" and "limbic" functions. Prog. Brain Res. 85, 119–146.

Alexander, D.C., Barker, G.J., Arridge, S.R., 2002. Detection and modeling of non-Gaussian apparent diffusion coefficient profiles in human brain data. Magn. Reson. Med. 48, 331–340.

Anbeek, P., Vincken, K.L., van Osch, M.J., Bisschops, R.H., van der Grond, J., 2004. Probabilistic segmentation of white matter lesions in MR imaging. NeuroImage 21, 1037–1044.

Assaf, Y., Freidlin, R.Z., Rohde, G.K., Basser, P.J., 2004. New modeling and experimental framework to characterize hindered and restricted water diffusion in brain white matter. Magn. Reson. Med. 52, 965–978.

Basser, P.J., Mattiello, J., LeBihan, D., 1994. MR diffusion tensor spectroscopy and imaging. Biophys. J. 66, 259–267.

Basser, P.J., Pajevic, S., Pierpaoli, C., Duda, J., Aldroubi, A., 2000. In vivo fibre tractography using DT-MRI data. Magn. Reson. Med. 44, 625–632.

Behrens, T.E., Woolrich, M.W., Jenkinson, M., Johansen-Berg, H., Nunes, R.G., Clare, S., Matthews, P.M., Brady, J.M., Smith, S.M., 2003. Characterization and propagation of uncertainty in diffusion-weighted MR imaging. Magn. Reson. Med. 50, 1077–1088.

Behrens, T.E., Berg, H.J., Jbabdi, S., Rushworth, M.F., Woolrich, M.W., 2007. Probabilistic diffusion tractography with multiple fibre orientations: what can we gain? NeuroImage 34, 144–155.

Ciccarelli, O., Parker, G.J., Toosy, A.T., Wheeler-Kingshott, C.A., Barker, G.J., Boulby, P.A., Miller, D.H., Thompson, A.J., 2003. From diffusion tractography to quantitative white matter tract measures: a reproducibility study. NeuroImage 18, 348–359.

Cook, P.A., 2006. Modelling uncertainty in brain fibre orientation from diffusion-weighted magnetic resonance imaging. Department of Computer Science, University College London. [Ph. D. thesis].

Frank, L.R., 2002. Characterization of anisotropy in high angular resolution diffusion-weighted MRI. Magn. Reson. Med. 47, 1083–1099.

Groenewegen, H.J., Wright, C.I., Uylings, H.B., 1997. The anatomical relationships of the prefrontal cortex with limbic structures and the basal ganglia. J. Psychopharmacol. 11, 99–106.

Heiervang, E., Behrens, T.E., Mackay, C.E., Robson, M.D., Johansen-Berg, H., 2006. Between session reproducibility and between subject variability of diffusion MR and tractography measures. NeuroImage 33, 867–877.

Jansons, K.M., Alexander, D.C., 2003. Persistent angular structure: new insights from diffusion magnetic resonance imaging data. Inverse Problems 19, 1031–1046.

Jelsing, J., Hay-Schmidt, A., Dyrby, T., Hemmingsen, R., Uylings, H.B., Pakkenberg, B., 2006. The prefrontal cortex in the Gottingen minipig brain defined by neural projection criteria and cytoarchitecture. Brain Res. Bull. 70, 322–336.

Jiang, H., van Zijl, P.C., Kim, J., Pearlson, G.D., Mori, S., 2006. DtiStudio: resource program for diffusion tensor computation and fibre bundle tracking. Comput. Methods Programs Biomed. 81, 106–116.

Jones, D.K., Travis, A.R., Eden, G., Pierpaoli, C., Basser, P.J., 2005. PASTA: pointwise assessment of streamline tractography attributes. Magn. Reson. Med. 53, 1462–1467.

Kobbert, C., Apps, R., Bechmann, I., Lanciego, J.L., Mey, J., Thanos, S., 2000. Current concepts in neuroanatomical tracing. Prog. Neurobiol. 62, 327–351.

Lazar, M., Alexander, A.L., 2003. An error analysis of white matter tractography methods: synthetic diffusion tensor field simulations. NeuroImage 20, 1140–1153.

Le Bihan, D., Poupon, C., Amadon, A., Lethimonnier, F., 2006. Artifacts and pitfalls in diffusion MRI. J. Magn. Reson. Imaging 24, 478–488.

Leemans, A., Sijbers, J., Verhoye, M., Van der Linden, A., 2005. Mathematical framework for simulating diffusion tensor MR neural fibre bundles. Magn. Reson. Med. 53, 944–953.

Leergaard, T.B., Bjaalie, J.G., Devor, A., Wald, L.L., Dale, A.M., 2003. In vivo tracing of major rat brain pathways using manganese-enhanced magnetic resonance imaging and three-dimensional digital atlasing. NeuroImage 20, 1591–1600.

Lin, C.P., Tseng, W.Y., Cheng, H.C., Chen, J.H., 2001. Validation of diffusion tensor magnetic resonance axonal fibre imaging with registered manganese-enhanced optic tracts. NeuroImage 14, 1035–1047.

Lind, N.M., Moustgaard, A., Jelsing, J., Vajta, G., Cumming, P., Hansen, A.K., 2007. The use of pigs in neuroscience: modeling brain disorders. Neurosci. Biobehav. Rev. 31, 728–751.

Lori, N.F., Akbudak, E., Shimony, J.S., Cull, T.S., Snyder, A.Z., Guillory, R.K., Conturo, T.E., 2002. Diffusion tensor fibre tracking of human brain connectivity: acquisition methods, reliability analysis and biological results. NMR Biomed. 15, 494–515.

Mori, S., Crain, B.J., Chacko, V.P., van Zijl, P.C., 1999. Three-dimensional tracking of axonal projections in the brain by magnetic resonance imaging. Ann. Neurol. 45, 265–269.

Murayama, Y., Weber, B., Saleem, K.S., Augath, M., Logothetis, N.K., 2006. Tracing neural circuits in vivo with Mn-enhanced MRI. Magn. Reson. Imaging 24, 349–358.

Oztas, E., 2003. Neuronal tracing. Neuroanatomy 2, 2–5.

Parker, G.J., Alexander, D.C., 2003. Probabilistic Monte Carlo based mapping of cerebral connections utilising whole-brain crossing fibre information. Lect. Notes Comput. Sci. 2732, 684–695.

Parker, G.J., Alexander, D.C., 2005. Probabilistic anatomical connectivity derived from the microscopic persistent angular structure of cerebral tissue. Philos. Trans. R. Soc. Lond., B Biol. Sci. 360, 893–902.

Parker, G.J., Wheeler-Kingshott, C.A., Barker, G.J., 2002. Estimating distributed anatomical connectivity using fast marching methods and diffusion tensor imaging. IEEE Trans. Med. Imaging 21, 505–512.

Parker, G.J., Haroon, H.A., Wheeler-Kingshott, C.A., 2003. A framework for a streamline-based probabilistic index of connectivity (PICo) using a structural interpretation of MRI diffusion measurements. J. Magn. Reson. Imaging 18, 242–254.

Pautler, R.G., 2004. In vivo, trans-synaptic tract-tracing utilizing manganese-enhanced magnetic resonance imaging (MEMRI). NMR Biomed. 17, 595–601.

Pautler, R.G., Silva, A.C., Koretsky, A.P., 1998. In vivo neuronal tract tracing using manganese-enhanced magnetic resonance imaging. Magn. Reson. Med. 40, 740–748.

Saleem, K.S., Pauls, J.M., Augath, M., Trinath, T., Prause, B.A., Hashikawa, T., Logothetis, N.K., 2002. Magnetic resonance imaging of neuronal connections in the macaque monkey. Neuron 34, 685–700.

Selemon, L.D., Goldman-Rakic, P.S., 1985. Longitudinal topography and interdigitation of corticostriatal projections in the rhesus monkey. J. Neurosci. 5, 776–794.

Skare, S., Andersson, J.L., 2001. On the effects of gating in diffusion imaging of the brain using single shot EPI. Magn. Reson. Imaging 19, 1125–1128.

Tournier, J.D., Calamante, F., Gadian, D.G., Connelly, A., 2004. Direct estimation of the fibre orientation density function from diffusion-weighted MRI data using spherical deconvolution. NeuroImage 23, 1176–1185.

Tuch, D.S., 2004. Q-ball imaging. Magn. Reson. Med. 52, 1358–1372.

Tuch, D.S., Reese, T.G., Wiegell, M.R., Makris, N., Belliveau, J.W., Wedeen, V.J., 2002. High angular resolution diffusion imaging reveals intravoxel white matter fibre heterogeneity. Magn. Reson. Med. 48, 577–582.

Zaborszky, L., Wouterlood, F.G., Lanciego, J.L., 2006. Neuroanatomical Tract-Tracing 3: Molecules–Neurons–Systems. Springer, New York.

Manuscript III

Dyrby TB., Rostrup E., Baaré WFC., van Straaten ECW., Barkhof F., Vrenken H., Ropele S., Schmidt R., Erkinjuntti T., Wahlund L-O., Pantoni L., Inzitari D., Paulson OB., Hansen LK., Waldemar G. on behalf of the LADIS study group, Segmentation of Age-related White Matter Changes in a Clinical Multi-centre Study. Neuroimage. 2008, doi:10.1016/j.neuroimage.2008.02.024

ARTICLE IN PRESS

YNIMG-05267; No. of pages: 11; 4C: 5, 6, 7, 8, 9

ELSEVIER

NeuroImage

www.elsevier.com/locate/ynimg
NeuroImage xx (2008) xxx–xxx

Segmentation of age-related white matter changes in a clinical multi-center study

Tim B. Dyrby,[a,b,c,*] Egill Rostrup,[a] William F.C. Baaré,[a] Elisabeth C.W. van Straaten,[d] Frederik Barkhof,[d] Hugo Vrenken,[d] Stefan Ropele,[e] Reinhold Schmidt,[e] Timo Erkinjuntti,[f] Lars-Olof Wahlund,[g] Leonardo Pantoni,[h] Domenico Inzitari,[h] Olaf B. Paulson,[a,i] Lars Kai Hansen,[c] and Gunhild Waldemar[b] on behalf of the LADIS study group

[a]*Danish Research Centre for Magnetic Resonance, Copenhagen University Hospital, Hvidovre, Denmark*
[b]*Memory Disorders Research Group, Department of Neurology, Rigshospitalet, Copenhagen University Hospital, Copenhagen, Denmark*
[c]*Intelligent Signal Processing Group, Informatics and Mathematical Modelling, Technical University of Denmark, Lyngby, Denmark*
[d]*Department of Neurology, VU Medical Center, Amsterdam, Netherlands*
[e]*Department of Radiology, Medical University, Graz, Austria*
[f]*Memory Research Unit, Department of Neurology, University of Helsinki, Helsinki, Finland*
[g]*Department of Clinical Neuroscience, NEUROTEC, Karolinska Institutet, Huddinge University Hospital, Stockholm, Sweden*
[h]*Department of Neurological and Psychiatric Sciences, University of Florence, Florence, Italy*
[i]*Neurobiology Research Unit, Rigshospitalet, Copenhagen University Hospital, Copenhagen, Denmark*

Received 7 August 2007; revised 10 February 2008; accepted 14 February 2008

Age-related white matter changes (WMC) are thought to be a marker of vascular pathology, and have been associated with motor and cognitive deficits. In the present study, an optimized artificial neural network was used as an automatic segmentation method to produce probabilistic maps of WMC in a clinical multi-center study. The neural network uses information from T1- and T2-weighted and fluid attenuation inversion recovery (FLAIR) magnetic resonance (MR) scans, neighboring voxels and spatial location. Generalizability of the neural network was optimized by including the Optimal Brain Damage (OBD) pruning method in the training stage. Six optimized neural networks were produced to investigate the impact of different input information on WMC segmentation. The automatic segmentation method was applied to MR scans of 362 non-demented elderly subjects from 11 centers in the European multi-center study Leukoaraiosis And Disability (LADIS). Semi-manually delineated WMC were used for validating the segmentation produced by the neural networks. The neural network segmentation demonstrated high consistency between subjects and centers, making it a promising technique for large studies. For WMC volumes less than 10 ml, an increasing discrepancy between semi-manual and neural network segmentation was observed using the similarity index (SI) measure. The use of all three image modalities significantly improved cross-center generalizability compared to neural networks using the FLAIR image only. Expert knowledge not available to the neural networks was a minor source of discrepancy, while variation in MR scan quality constituted the largest source of error.

Keywords: Artificial neural network; Automatic segmentation; Disability; Elderly; LADIS study; Leukoaraiosis; MRI; White matter lesions

Introduction

Age-related white matter changes (WMC) are frequently observed in clinical magnetic resonance imaging (MRI) and computed tomography (CT) in the elderly and have been associated with a number of vascular risk factors (Pantoni, 2002). MRI benefits from the availability of multiple assessment methods and is generally recognized as the most sensitive technique for detecting WMC (Lopez et al., 1995; Scheltens et al., 2003; van Straaten et al., 2004; Wahlund et al., 2001).

Using MRI, much effort has been put into developing and validating qualitative visual rating scales for WMC (Fazekas et al., 2002; Scheltens et al., 1998; Wahlund et al., 2001). Visual

* Corresponding author. Danish Research Centre for Magnetic Resonance, Copenhagen University Hospital, Hvidovre, Kettegaard Allé 30, DK-2650 Hvidovre, Denmark. Fax: +45 3647 0302.
E-mail address: timd@drcmr.dk (T.B. Dyrby).
Available online on ScienceDirect (www.sciencedirect.com).

1053-8119/$ - see front matter © 2008 Elsevier Inc. All rights reserved.
doi:10.1016/j.neuroimage.2008.02.024

rating scales are easily implemented in clinical practice, where they can provide a rapid assessment of the degree of WMC. Nevertheless, the technique is observer-dependent, and correlations with clinical deficits may be obscured by a low number of classes or by ceiling effects (Scheltens et al., 1998; van Straaten et al., 2006). Furthermore, the limited ability to detect progression necessitates the use of specialized rating scales (Scheltens et al., 2003).

In order to quantify WMC, a recent multi-center study (van Straaten et al., 2006) measured WMC volumes using a semi-manual technique. While good correspondence was found with visual rating scales, there was great variability in WMC volumes within each class of the visual rating scale. Although quantitative, a major drawback with the (semi-) manual technique is that it is very labor intensive and therefore very costly. Only few studies in age-related WMC in the elderly have focused on developing automatic segmentation methods (Admiraal-Behloul et al., 2005; DeCarli et al., 2005; Jack et al., 2001; Wen and Sachdev, 2004; Wu et al., 2006). This is in contrast to research in multiple sclerosis (MS) (Alfano et al., 2000; Anbeek et al., 2004; Erickson and Avula, 1998; Goldberg-Zimring et al., 1998; Kamber et al., 1995; Kikinis et al., 1999; Rey et al., 2002; Van Leemput et al., 2001; Zijdenbos et al., 1994; Zijdenbos et al., 2002). Typically, only few subjects (<20) have been used to validate methods for automatic segmentation of the heterogeneous WMC with exception of for example Lao et al. (2006) ($n=46$), and Admiraal-Behloul et al. (2005) ($n=100$). Using such a sparse data set for validation, it is difficult to reveal the "true face" (consistency) of a segmentation method in a real life situation. Nevertheless, many have reported good agreement between manual and automatic segmentation methods (Gasperini et al., 2001; Jackson et al., 1993; Kapeller et al., 2003; Zijdenbos et al., 1994). When applied in multi-center cohorts, automatic segmentation methods must be flexible to cope with the variation across various MR scanner types, field strengths and imaging strategies. These sources of variation can be reduced significantly using pre-processing pipelines, such as the one proposed by Zijdenbos et al. (2002). By using strict pre-processing pipelines, the method selected for segmenting age-related WMC in multi-center studies is not constrained to be an adaptive classifier as for example proposed by Van Leemput et al. (2001). Instead, classifiers with a fixed architecture once trained, such as the K-nearest neighbors (KNN) classifier used by Anbeek et al. (2004), the generalized linear support vector machine (SVM) classifier used by Lao et al. (2006) or the non-linear artificial neural network (ANN) classifier used by Zijdenbos et al. (2002), can be employed. Until now, only the ANN method has been shown to possess promising generalization characteristics in segmenting WMC in a multi-center study (Zijdenbos et al., 2002).

The present study aimed to optimize the generalizability of artificial neural networks for automatic segmentation of age-related WMC on clinical multi-center MR scans. MR scans were acquired for a large population of non-demented elderly subjects, who participated in the European multi-center study, Leukoaraiosis And Disability (LADIS) (Pantoni et al., 2005). MR scans were acquired from 11 different MR centers. The neural network used information from T1- and T2-weighted and FLAIR sequences, neighboring voxels and spatial location. Six neural networks optimized by an iterative training/pruning procedure were produced to investigate the impact of different input information on WMC segmentation. Finally, neural network output was compared to semi-manually measured WMC volumes, which were available for the whole cohort.

Material and methods

Subjects

MRI data were acquired from a population consisting of 639 non-demented elderly subjects from 11 centers as part of the Leukoaraiosis And Disability (LADIS) study, a European 5th Framework project investigating the impact of age-related WMC on the transition to disability (Pantoni et al., 2005).

The study included subjects fulfilling the criterion of having some degree of WMC found on a baseline MRI scan. Further inclusion criteria were age between 65 and 85 years and no or only mild disability in everyday life according to the Instrumental Activities of Daily Living scale (Lawton and Brody, 1969; Pantoni et al., 2005). MRI data were collected over a 3-year period from end 2001 to 2004.

MR protocols

The standardized MR sequences obtained within the LADIS protocol included 2D axial T2-weighted fast spin echo (T2W) and FLAIR scans, and a 3-D, coronal or sagittal, T1-weighted (T1W) sequence. The specification of the MR sequences was somewhat flexible in order to meet the abilities of the various MR scanner types (all 1.5 T) used at each center. The parameter ranges were: *T2W MR scan*: TR/TE 4000–6000/100–120 ms; NEX=2; *FLAIR sequence*: TR/TE=6000–10,000/100–140 ms; TI=2000–2400 ms; NEX=1. For T2W and FLAIR, the resolution was $1\times1\times5$–7.5 mm^3; slice gap=0.5 mm; FOV=250 mm; matrix size=256×256–192, number of slices=19–28. For the *T1W sequence*: TR/TE=10–25/4–7 ms; TI=100–950 ms; flip–angle=15–30°; FOV=250 mm; 1 mm^3 isotropic voxels.

Data quality assessment

Prior to processing, all MRI data sets were evaluated in order to achieve a more homogenous quality level. Subjects were excluded from further participation if (1) not all three MRI modalities were present; (2) the brain was only partially covered; and (3) if gross motion or other image artifacts were present. Scans were evaluated by visual inspection and by means of the quantitative automated method described previously (Dyrby and Liptrot, 2005), according to which data sets with a T1W with a contrast-to-noise ratio (CNR) less than 1.5 were inspected for an exclusion. The CNR was calculated between the mean intensities of grey matter (GM) and white matter (WM).

Data processing

The data processing procedure used in this study consisted of two steps: a pre-processing and a post-processing procedure. The pre-processing was applied before segmentation in order to reduce differences in image quality between subjects as well as centers. The post-processing was applied after segmentation in order to reduce the volume of false-positives WMC voxels in the WMC probability maps.

Pre-processing

In the current study, pre-processing was streamlined using a pipeline program that controls the execution and data generation

Please cite this article as: Dyrby, T.B., et al., Segmentation of age-related white matter changes in a clinical multi-center study, NeuroImage (2008), doi:10.1016/j.neuroimage.2008.02.024

for each subject in a standardized way (Rask et al., 2004). The different tasks in the pre-processing setup were as follows (I–VII):

(I) Intensity difference between odd and even numbered slices in the 2D MR protocols (FLAIR and T2W scans), that appear due to imperfect slice profiles, were corrected using an 8th degree polynomial. The polynomial was fitted to the mean intensity of each slice.

(II) The FLAIR and T1W images were co-registered to the T2W image space using normalized mutual information and 6 degrees-of-freedom available in the SPM2 software (Wellcome Department of Imaging Neuroscience, www.fil.ion.ucl.ac.uk/spm).

(III) All three modalities were then re-sampled, using a 7th order b-spline interpolation, to the FLAIR image space with 1 mm^3 isotropic resolution to preserve the detailed structural information of the T1W. The WMC volume-of-interest (VOI), which was semi-manually delineated on the original FLAIR image (van Straaten et al., 2006), was also re-sampled to the higher resolution using nearest neighbor interpolation. Unless otherwise stated, manual WMC will be treated from now on as synonymous with the re-sampled semi-manual WMC.

(IV) A brain mask was automatically generated for separating the brain from surrounding structures. First the T1W and T2W data were each segmented into GM, WM and cerebrospinal fluid (CSF) probability maps using SPM2 (Ashburner and Friston, 1997). Next, combining segmentation results and applying standard morphologic operations ensured a robust extraction of the brain, which was confirmed by visual inspection.

(V) Signal intensity variation due to RF inhomogeneity was reduced using the N3 software (Sled et al., 1998). This correction was applied to each of the three modalities within the brain mask generated in step IV.

(VI) Spatial context, which describes relative distances within the brain mask, was used as input feature for the neural network. The three directions of a distance map were defined in native FLAIR space (step III) in, respectively, the inferior–superior, left–right and anterior–posterior direction. The starting point for each of the three directions was automatically determined by identifying the slice where the brain mask begins in the coronal, sagittal or the axial plane. Combined, the three distance maps define a relative (3-D) position within the brain. Each distance map was normalized to the maximal distance value found within the brain mask.

(VII) Finally, inter-subject intensity standardization was applied to each type of modality to suppress center-specific intensity variations using a standard z-score (Dyrby and Liptrot, 2005). Based on the segmentation results of the T1W obtained in step IV, reference regions including only GM and WM tissue classes were automatically generated by thresholding the GM and WM probability maps at >85%. For the re-sampled T1W and T2W image, the mean value and standard deviation were calculated from the intensities within the GM and WM reference regions. For the re-sampled FLAIR image, the WM reference region was used for intensity standardization, because the contrast between other tissue types, which is normally low in FLAIR images, significantly varied across centers. After normalization of the intensities, each (whole) image (T1W, T2W and FLAIR) was linearly scaled to a user-defined mean intensity of 500 and standard deviation of 50.

Post-processing

Anatomically WMC must (1) be spatially connected to WM and (2) located inside the brain mask (step IV). By incorporating this knowledge in the post-processing of the automatically segmented WMC, the volume of false-positives was greatly reduced. In neural network configurations in which only the FLAIR modality was used as input (F4–F6 in Table 1), the first criterion was not used due to a low GM–WM CNR in the image. Therefore, only the criterion of location within the brain mask was applied in the post-processing.

Neural network configurations

Delineation of training regions

Age-related WMC were semi-manually delineated on the whole cohort by a single expert using the procedure described in van Straaten et al. (2006). The reliability was tested twice over a 2-month interval in 18 subjects with a mean volume (SD) of 26.3 (19.0) ml, resulting in a coefficient of variation of 4%.

The MR scans of the five subjects used for generating the training set were carefully selected after visual inspection of the whole cohort and were deemed representative for the various degrees of observed WMC volumes. The five subjects originated from three centers: two subjects from center C01 and C02, and one subject from center C04. Training samples for WMC consisted of manual WMC (see data processing, step III). Training samples for GM, WM and CSF consisted of manually delineated VOIs, drawn on the re-sampled T1W image using the MIPAV program (http://mipav.cit.nih.gov/). Voxels included in the VOIs were equally distributed within each brain and provided the neural network with spatial information of the tissue type as well as partial volume effects (PVE). The GM, WM and CSF VOIs each contained approximately 9000 voxels per subject. Finally, in order to create the training data set for the neural network, from each subject, a total of 2448 voxels (samples) were selected pseudo randomly—666 samples from GM, WM and CSF each and 450 from manual WMC.

The neural classifier

The artificial neural network used in this study was initiated as a fully connected 2-layer feed-forward network (Bishop, 1995). The neural network has an input layer with N_i input neurons determined by the dimension of input features. The hidden layer consists of N_h units each with a non-linear hyperbolic tangent function as the activation function

$$h_j(\mathbf{x}) = \tanh\left(\sum_{k=1}^{N_i} w_{j,k}^{(1)}\mathbf{x}_k + w_{j,0}^{(1)}\right) \quad (1)$$

where $\mathbf{x}$ is a input vector of features (Table 1); the weight $w_{j,k}^{(1)}$ connecting the kth input neuron with the jth hidden neuron. Biases to the hidden layer are $w_{j,0}^{(1)}$.

For providing the voxel-wise probability of the N_c tissue classes the output layer has $N_o = N_c - 1$ output neurons, each expressed as

$$y_q(\mathbf{x}) = \sum_{j=1}^{N_h} w_{q,j}^{(2)} h_j(\mathbf{x}) + w_{q,0}^{(2)} \quad (2)$$

The posterior probability, $p(C|\mathbf{x})$, of an input feature $\mathbf{x}$ belonging to one of N_c tissue classes was then calculated from the response of

Please cite this article as: Dyrby, T.B., et al., Segmentation of age-related white matter changes in a clinical multi-center study, NeuroImage (2008), doi:10.1016/j.neuroimage.2008.02.024

Table 1
Configuration of the six neural networks (F1–F6)

Neural network	Input feature sets	F1	F2	F3	F4	F5	F6
		T1, *T2*, *F*, $N_{3\times3}$, S_{xyz}	*T1*, *T2*, *F*, $N_{3\times3}$	*T1*, *T2*, *F*	*F*, $N_{3\times3}$, S_{xyz}	*F*, $N_{3\times3}$	*F*
Fully connected	Input units (N_i)	30	27	3	12	9	1
	Hidden units (N_h)	80	80	80	80	80	80
	Number of weights (w)	2723	2483	563	1283	1043	403
Optimized	Hidden units	48	26	33	73	37	9
	Number of weights	352	181	123	608	221	30
	Optimal threshold	91%	82%	75%	89%	84%	81%
	(maximal) mean SI	0.54	0.56	0.54	0.49	0.48	0.40

Input features sets are voxel intensities from the image modalities: T1W (*T1*), FLAIR (*F*), T2W (*T2*) and 3×3 neighboring voxels ($N_{3\times3}$) and relative positions in 3-D (S_{xyz}). All six neural networks outputted four probability maps representing GM, WM, CSF and WMC. Fully connected: Neural networks used for initial training. Optimized: Selected trained neural network with highest generalizability among pruned neural networks (Fig. 2). The optimal threshold for segmenting WMC was determined at maximal mean SI (Fig. 3). Training samples for the four tissue types to be segmented were extracted from five subjects: two subjects from centers C01 and C02, one subject from center C04.

the output in Eq. (2) using the softmax function. Then the model function of a neural network for probabilistic tissue segmentation expresses

$$p(C_s|\mathbf{x}) = \begin{cases} \dfrac{\exp(y_s(\mathbf{x}))}{\sum_{t=1}^{N_c-1}\exp(y_t(\mathbf{x}))+1} & \text{for } s = 1,\ldots,N_c-1 \\ 1-\sum_{t=1}^{N_c-1} p(C_t\,|\,\mathbf{x}) & \text{for } s = N_c \end{cases} \quad (3)$$

Input features

Various input features and their impact on WMC classification were investigated. We created data sets, $D=\{(\mathbf{x}^n, \mathbf{t}^n)\}$, $n=1,\ldots,N$, of N corresponding values of input features ($\mathbf{x}$) and delineated examples ($\mathbf{t}$) for training the model function $p(C|\mathbf{x})$ from Eq. (3). The input features were extracted from the pre-processed T1W (T1), FLAIR (F) and T2W (T2) images. Additionally, for each image, the intensity information from each voxel of a 3×3 neighborhood in the axial plane (N_{3x3}) or spatial information (S) as obtained in pre-processing (see data processing, step VI) was included as input features. In total, six different input configurations (outlined in Table 1) producing six neural networks (F1 to F6) were created; three with multi-modality inputs (F1–F3), and three with the FLAIR as single-modality input (F4–F6).

Generalizability of the neural classifier

Even though the manually delineated training sets (defined on the MR scans of five subjects from 3 of the 11 centers) represent a broad variety of tissue examples, it was anticipated that this would not guarantee high generalizability of the neural network. Neural networks are most likely to produce generalizable results when the number of weights is optimally selected. To this end, a three-step procedure was followed in the training phase of the neural networks, consisting of an over-fitting step, a pruning step and a selection step.

The over-fitting step. The fully connected neural networks (Table 1), containing more weights than required for the segmentation task, were trained to produce six over-fitted neural networks. Training was realized by iteratively minimizing the negative log-likelihood cost function

$$E(\mathbf{w}) = \sum_N -\log(p(D|\mathbf{w})) + R \quad (4)$$

where $R=1/2\alpha\cdot\mathbf{w}^2$ is a weak regulation term on both input and output weights ensuring numerical stability and $p(D|\mathbf{w})$ is the likelihood of the data set given the weights.

For initial training, first the Gradient Descent (GD) optimization scheme was used to obtain an approximated quadratic solution needed for the subsequent Pseudo Gauss-Newton (PGN) optimization scheme. For the first step, 250 iterations were used, while 60,000 iterations were needed to ensure over-fitting in the second step (Bishop, 1995).

The pruning step. For each of the six over-fitted fully connected neural networks, a whole family of neural networks ($l=1,\ldots, L$) with individual ability to generalize over the training samples was then generated by repeating a pruning-retraining procedure based on the Optimal Brain Damage (OBD) method (Le Cun et al., 1990). First, weights having the lowest saliency in the neural network were pruned (here 1% of the weights). Saliency was defined as

$$\xi(w_n) = -w_n\frac{\partial E(w)}{\partial w_n} + w_n^2\left(R + 0.5\frac{\partial^2 E(w)}{\partial w_n^2}\right) \quad (5)$$

where $E(w)$ is the cost function from Eq. (4) without any regulation term. Instead, the regulation R from Eq. (4) was used in Eq. (5).

Retraining the pruned neural network then followed by using five iterations of GD and 60 and 200 iterations of PGN for neural network F1–F3 and F4–F6, respectively (Table 1). The pruning–retraining procedure was repeated until 95% of the weights in a fully connected neural network were pruned or an output neuron was disconnected from the hidden layer.

The selection step. Finally, among the family of neural networks produced in the pruning step, the (optimized) neural network with highest generalizability was selected for the segmentation task. The selection was based on the Bayesian Information Criteria (BIC)

Please cite this article as: Dyrby, T.B., et al., Segmentation of age-related white matter changes in a clinical multi-center study, NeuroImage (2008), doi:10.1016/j.neuroimage.2008.02.024

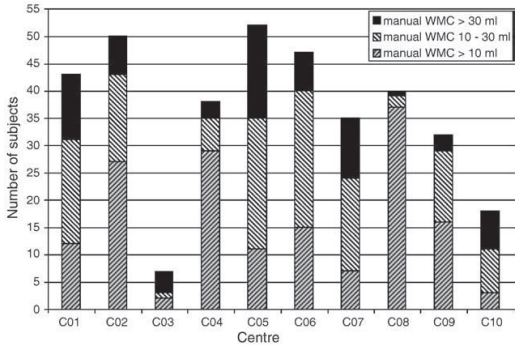

Fig. 1. Within each center, the distribution of subjects falling into three subgroups of manual WMC volume is shown: a low, moderate and a high subgroup having <10 ml, 10–30 ml and >30 ml of manual WMC volume.

(Schwarz, 1978) expressed in Eq. (6) where a penalty term added to the training error in Eq. (4) ensured punishment of large neural networks with expected reduced generalizability compared to the smaller neural networks.

$$E_{\mathrm{BIC}}(w_l) = 2E(w_l) + \log(N)K \tag{6}$$

where K expresses the total number of weights in the lth pruned neural network and N expresses the number of training samples used.

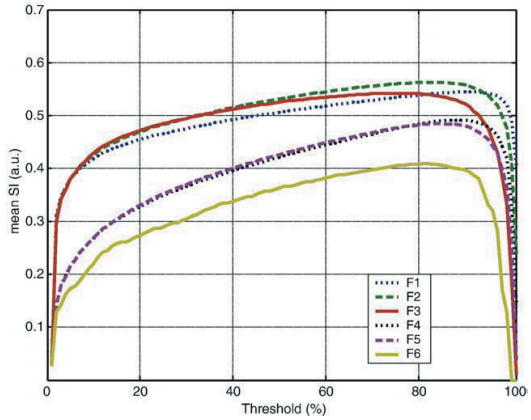

Fig. 3. Mean SI versus threshold for all 362 subjects in the cohort using the (optimized) neural networks (F1–F6). Optimal threshold for segmentation of WMC was selected at maximal mean SI. All feature inputs to a single modality neural network (F4–F6) improve the overall mean SI. In contrast, the multi-modality neural networks (F1–F3) demonstrated less dependency.

Evaluation

The agreement between the WMC VOIs arising from the manual delineation (MAN) and the neural networks was expressed using the similarity index and the sensitivity measure. The similarity index

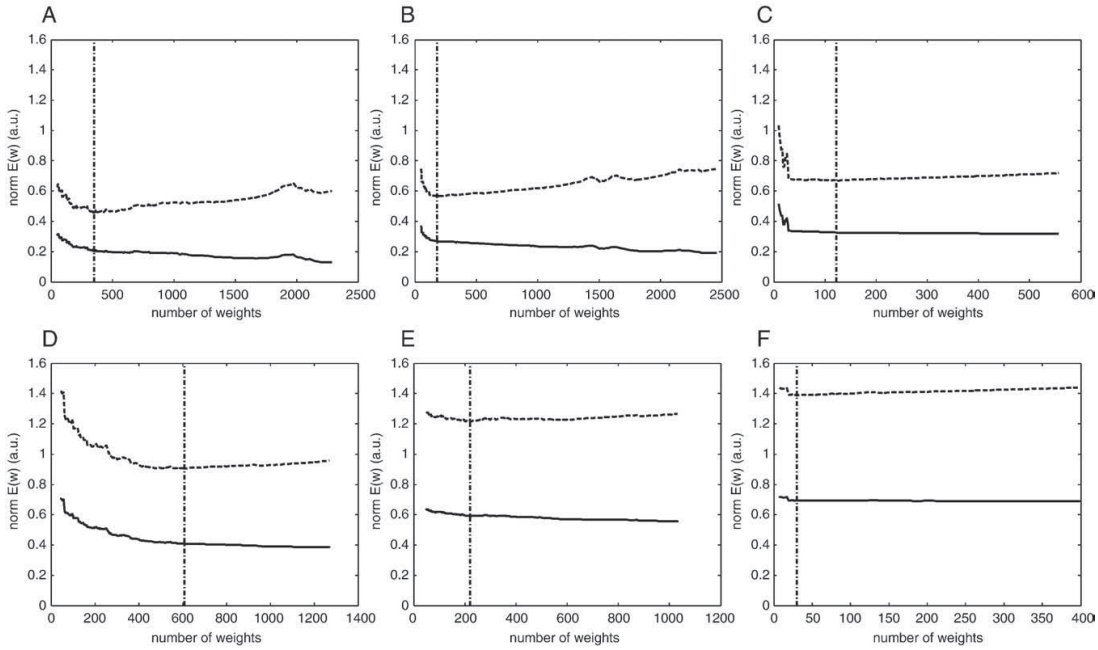

Fig. 2. In the pruning step, a series of neural networks were produced for each of the six neural networks (F1–F6) in (A–F). The x-axis shows the number of weights of a pruned network, and the y-axis corresponds to the negative log-likelihood error normalized to the number of training samples used. (Solid) Training error and (dashed) regulated training error using BIC. Highest number of weights was the (initially) fully connected neural network. An optimized neural network (F1–F6) was the one having the highest generalizability among the series of neural networks defined as the minimum regulated training error (vertical line dashed-dot) (A–F).

Please cite this article as: Dyrby, T.B., et al., Segmentation of age-related white matter changes in a clinical multi-center study, NeuroImage (2008), doi:10.1016/j.neuroimage.2008.02.024

Table 2
Mean SI (±SD) of the cohort within subgroups of manual WMC volume using neural networks (F1–F6) and corresponding optimal thresholds given in Table 1

	<10 (ml)	10–30 (ml)	>30 (ml)
F1	0.43±0.15	0.61±0.11	0.63±0.14
F2	0.45±0.15	0.62±0.11	0.65±0.15
F3	0.42±0.15	0.62±0.11	0.64±0.16
F4	0.21±0.13	0.47±0.11	0.57±0.14
F5	0.15±0.10	0.40±0.12	0.55±0.14
F6	0.11±0.08	0.33±0.12	0.52±0.14

(SI) was derived from the kappa statistics (Zijdenbos et al., 1994), an agreement measure corrected for chance correspondence, under the assumption of a large rate of negative judgments for both observers. The similarity index was defined as

$$\mathrm{SI} = \frac{2V_{\mathrm{ANN+MAN}}}{V_{\mathrm{ANN}} + V_{\mathrm{MAN}}} \quad \mathrm{SI} \in [0:1] \tag{7}$$

where V_{MAN} and V_{ANN} were the volumes of WMC as determined by each method, and $V_{\mathrm{ANN+MAN}}$ was the volume agreed by both methods to be WMC. A similarity index of 0.6 has been defined as good (Bartko, 1991).

The sensitivity measure (SE) describes how sensitive a neural network is in detecting the spatially same voxels as found in MAN regardless of the amount of false-positives. The sensitivity measure was derived as the fraction by which segmented voxels by the neural network were overlapping MAN, and was expressed as

$$\mathrm{SE} = \frac{V_{\mathrm{ANN+MAN}}}{V_{\mathrm{MAN}}} \quad \mathrm{SE} \in [0:1] \tag{8}$$

Results

Of the 639 subjects in the LADIS cohort, 362 subjects from 10 of the 11 different centers passed the data quality and homogeneity criteria for the present segmentation study and were successfully pre-processed. Subjects were excluded due to incomplete brain coverage ($n=66$), missing modalities ($n=86$), motion ($n=40$), low contrast-to-noise (CNR) in the T1W images ($n=37$) or problems related to image processing ($n=48$). The distribution of excluded subjects was found dependent upon the actual artifact; brain coverage and low CNR in the T1W images were center dependent, in contrast to motion artifacts. For example, subjects excluded because of CNR problems were from center C03 only (Fig. 1) and one center was excluded due to incomplete brain coverage. Fig. 1 shows, within centers, how subjects were distributed over three subgroups of manual WMC volume: <10 ml, 10–30 ml and >30 ml. Most centers had similar distribution of WMC volume, although centers C04 and C08 were observed having relatively few subjects with high WMC volume. The distribution of subjects within the three subgroups of WMC volume was 159, 131 and 72 with the high WMC volume as the latter.

Generalized neural networks

Training error, with and without BIC, as a function of the number of weights after pruning is shown in Fig. 2. The training error without BIC (solid curve) was continuously decreasing with a minimal error found at the fully connected neural network (maximum number of weights). The BIC-regulated training error, however, displayed minima error at the neural network having the highest generalizability among the family of neural networks (dot-dashed vertical line). (Please note, the training (with and without regulation) in Fig. 2 is a within (family-) neural network measure only.) Compared to the initial fully connected neural networks before pruning, the optimized neural networks required much fewer weights to segment the different brain tissues (Table 1). Moreover, both the optimized multi- (F1–F3) and single-modality (F4–F6) neural networks generally demonstrated an increased use of hidden units with increased number of input features as a consequence of the increasingly complex feature space provided. However, an exception was the optimized F2 neural network, which was found to have fewer hidden units than the optimized (and simpler) F3 neural network (Table 1). In the remainder of the study, neural networks (F1–F6) refer to those optimized for having the highest generalizability as marked in Fig. 2 and shown in Table 1.

Mean similarity index

For each of the six neural networks (F1–F6), mean SI (of all 362 subjects) as a function of threshold is shown in Fig. 3. Mean SI for the multi-modality neural networks F1–F3 was observed to be similar over a wide range of thresholds. For example, for the F2 neural network, the mean SI did not fall below 10% of its maximum value between thresholds ranging from 34% to 97% (Fig. 3). Moreover, mean SI for the multi-modality neural networks was considerably higher than those for the single-modality neural networks F4–F6. Overall, the F2 neural network had the highest and the F6 neural network the lowest mean SI. For a robust binarization of the probabilistic WMC maps produced by the neural networks, the optimal threshold was defined as the one giving the maximal mean SI (MMSI). Optimal thresholds ranged from 91% for neural network F1 (MMSI 0.54) to 75% for F6 (MMSI 0.40) (Table 1).

Volumetric agreement

The correlations between WMC volumes obtained by manual and neural network segmentation were highly significant. The

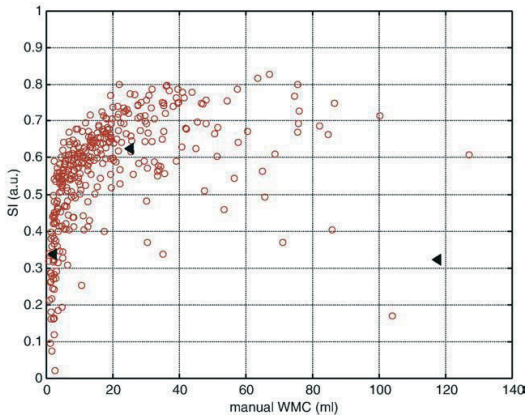

Fig. 4. Similarity index in relation to manual WMC volume on the 362 subjects included. SI was based on WMC probability maps from the F2 neural network thresholded at 82%. Subjects visualized in Figs. 5, 6 and 7 are visualized as black triangles. Good SI ranging can be observed above 5 ml of manual WMC.

Please cite this article as: Dyrby, T.B., et al., Segmentation of age-related white matter changes in a clinical multi-center study, NeuroImage (2008), doi:10.1016/j.neuroimage.2008.02.024

Table 3
Mean SE (±SD) of the cohort within subgroups of manual WMC volume using neural networks (F1–F6) and corresponding optimal thresholds given in Table 1

	<10 (ml)	10–30 (ml)	>30 (ml)
F1	0.59±0.14	0.62±0.12	0.57±0.16
F2	0.61±0.15	0.63±0.13	0.57±0.17
F3	0.58±0.15	0.60±0.14	0.54±0.17
F4	0.52±0.15	0.56±0.14	0.50±0.18
F5	0.51±0.14	0.58±0.12	0.49±0.19
F6	0.51±0.14	0.49±0.14	0.38±0.18

correlation coefficients were 0.81, 0.77, 0.74, 0.69, 0.63 and 0.28 ($p<0.001$) for neural networks F1 through F6, respectively. Among neural networks, the F1 neural network had the highest correlation (Pearson) coefficient. Correlations varied widely across centers. The lowest correlation was found in C01 for neural network F1 ($r=0.64$) and the highest for C04 ($r=0.95$). In general, the neural networks relatively overestimated WMC volumes when manual WMC volumes were low and underestimated volumes at high manual WMC volumes. For example, for the F1 neural network, the average difference $V_{ANN}-V_{MAN}$ for the three subgroups was 3.7±6 ml for $V_{MAN}<10$ ml, −0.73±9.9 ml for 10 ml$<V_{MAN}<$30 ml and −17.2±30 ml for $V_{MAN}>30$ ml.

Spatial agreement

The similarity index varied widely for individual subjects with respect to manual WMC volumes and decreased significantly for small WMC volumes. For example, for the F2 neural network, the mean SI was 0.45 (±0.15) for volumes less than 10 ml as compared to a SI of 0.65 (±0.15) for volumes larger than 30 ml (Table 2 and Fig. 4). Sources of variation were investigated using general linear modeling with SI expressed as a linear function of the center from which data originated: the neural network used, WMC volume, as well as age and gender of the subject. WMC volumes were logarithmically transformed ($\log(V_{MAN})$) to approach a normal distribution. As shown in Fig. 3, a significant difference between the six neural networks was observed, but there was no significant difference between the three multi-modality neural networks (F1–F3) (Table 2). Nevertheless, based on the SI, the best spatial agreement within the three subgroups of WMC volume was observed for the F2 neural network (Table 2). For each neural network, the most significant covariate was $\log(V_{MAN})$ (e.g. for F2: $r^2=0.44$, $p<0.001$, Fig. 4), while the center from which the data originated contributed only very little to overall variance (e.g. for F2: $r^2=0.05$, $p<0.05$). Generally, age and gender were not significant and explained less than 1% of the total variance. In contrast to SI, SE did not differ between the three subgroups of WMC volume and was similar across the six neural networks (Table 3).

Visual inspection

The segmented images were inspected visually to assess the localization and spatial extent of discrepancies between the manual and automated method. For illustrative purposes, three subjects, each representing one of the three subgroups of WMC volume, were selected in order to visualize the factors leading to a lowered SI. The selected subjects are indicated in Fig. 4 and represent an average performance as indicated by SI of the F2 neural network (Figs. 5–7).

The visual inspection revealed a number of regions where overestimation of WMC volumes by the neural networks leads to decreases in SI (Figs. 5 and 6). In combination, image artifacts in the FLAIR image typically seen as hyper intense regions in cortical areas, the septum pellucidum and flow artifacts in the 4th ventricle contributed to a large percentage of false-positive WMC (Fig. 5). Such artifacts in the FLAIR image were found varying across MR centers as well as subjects, seemingly independent of the total WMC volume (results not shown). Minor differences between WMC segmented manually and by the neural network were observed at moderate WMC volume (Fig. 6) as reflected in the SI (Fig. 4). However, at high WMC volume where the changes are more diffuse, larger and fewer in number, the neural networks tend to be more conservative in determining the WMC compared to manual WMC (Figs. 4 and 7).

Sagittal view disclosed a systematic discrepancy that is likely causing a bias in the results (e.g. in a lowered SI) when comparing manual and automated segmentation. While the manual WMC VOIs

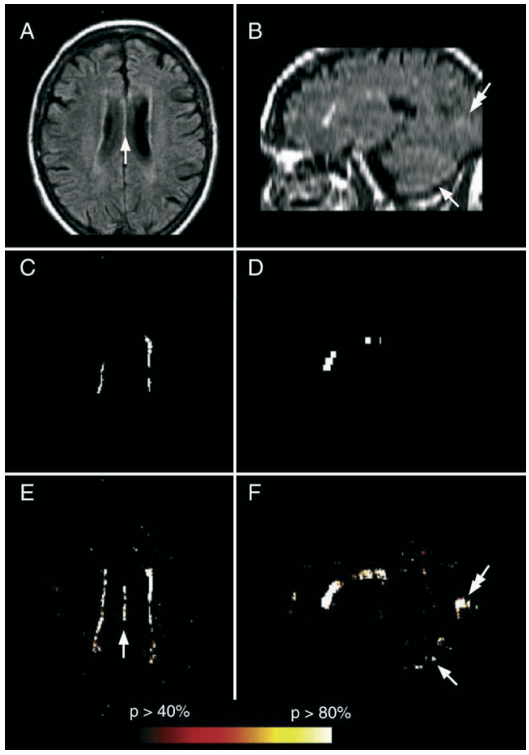

Fig. 5. Subject from center C09 having low manual WMC volume. Axial (A, C, E) and sagittal (B, D, F) view. Re-sampled FLAIR image (A, B); semi-manual re-sampled WMC VOI (C, D). Probability map of WMC using a F2 neural network (E, F). Manual WMC volume: 2.2 ml; SE=0.77 and SI=0.34. Artifacts in the automatic segmentation caused by image artifacts in FLAIR (single arrow) and WMC not found in the manual WMC VOI (double arrow).

Please cite this article as: Dyrby, T.B., et al., Segmentation of age-related white matter changes in a clinical multi-center study, NeuroImage (2008), doi:10.1016/j.neuroimage.2008.02.024

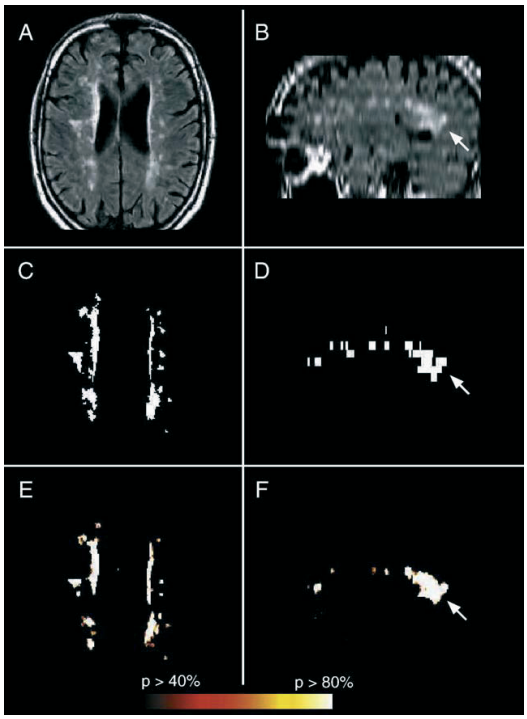

Fig. 6. Subject from center C07 having moderate manual WMC volume. Axial (A, C, E) and sagittal (B, D, F) view. Re-sampled FLAIR image (A, B); semi-manual re-sampled WMC VOI (C, D). Probability map of WMC using a F2 neural network (E, F). Manual WMC volume: 25.2 ml; SE=0.49 and SI=0.62. In sagittal view, the probability maps by neural networks are smooth (D, F) compared to manual (D) because of the higher resolution used for the segmentation (arrow).

were delineated on the original low resolution FLAIR image, the WMC probability maps produced by the neural network were based on high-resolution data (3-D T1W, or FLAIR/T2W re-sampled to high resolution). The automatically generated maps therefore appear continuous and possibly more specific than the manually delineated WMC (Figs. 5–7).

The F1 and F4 neural networks (Table 1) incorporated relative spatial positions in their input feature set. Contrary to expectations, the resulting probability maps displayed a weak bias, i.e. a small but consistent decrease in probability as a function of position across the two brain hemispheres (results not shown). Such an asymmetric bias in tissue probability was not observed for any of the other neural networks, or for manual WMC VOIs.

Discussion

In the present study, we successfully applied an optimized artificial neural network for automatic segmentation of age-related WMC in the LADIS multi-center study. The automatic segmented WMC were validated against semi-manually drawn WMC VOIs available for the 362 included subjects. We found a good spatial correspondence between manual and neural network segmented WMC as evidenced by high SI measures. It is noteworthy that the consistency of the neural network segmentation results achieved was based on training samples extracted from five subjects only. Among the six neural networks, the F2 neural network using multi-modal and neighboring voxel information was found to have the best overall performance in segmenting WMC. Discrepancies found between manually and automatically segmented WMC could generally be attributed to: (I) the high image resolution used in the neural network segmentation compared to the lower resolution of the FLAIR images that were used in the manual segmentation; (II) inaccuracies in the neural network segmentation due to varying MR scan quality not accounted for by the pre-processing; and (III) false-positives due to the lack of "expert knowledge" to distinguish artifacts and real WMC, in spite of similar signal characteristics.

Originally, the MRI study of the LADIS cohort was not designed for studying automatic segmentation methods such as the neural network classifiers; therefore only a subset of the MRI scans (56%) fulfilled the criteria of minimal image quality as defined in this study. Future studies including automatic segmentation methods should as a minimum include whole-head coverage, as well as strict criteria for homogenization of tissue contrast, and CNR.

Pruning included in the training procedure was essential to objectively select an optimized neural network architecture for segmentation rather than using a fixed and fully connected neural network (Alirezaie et al., 1995; Goldberg-Zimring et al., 1998; Özkan et al., 1993; Zijdenbos et al., 1994; Zijdenbos et al., 2002). For each of the six neural network configurations, a pruning step generated a "family" of neural networks with different generalization abilities. This process was extremely time consuming and took a few months to complete. For the multi-modality neural networks, the number of initial hidden units in the full-connected feed-forward neural network could be reduced from 80 to around 30–40 hidden units, indicating that in future studies with a similar setup the training/pruning procedure can be reduced to a few days.

The number of hidden units expresses the complexity or flexibility of a neural network. Consequently, this number can be used as an indication of the contrast in the feature space of a particular neural network, and reflects the ease by which the four tissue classes can be segmented. Notably, although the best performing F2 neural network had 9 more input features to account for voxel neighborhood than neural network F3, the number of hidden units decreased from 33 to 26. Likewise, the multi-modality F1 and F2 neural networks needed less hidden units, 48 and 26 respectively, to archive optimal generalization abilities than the single-modality neural networks F4 and F5, 73 and 37 respectively. Once trained, the segmentation of a whole brain data set for a multi-modality neural network was less than 10 min. Note that in contrast to the generally lower image resolution used in the literature input features in the present study were of high resolution. The latter has to be taken into account when comparing segmentation time between methods.

Five subjects were selected for creating training sets for the tested neural networks. The decision of using five subjects was somewhat arbitrary, as the literature on how best to select training samples in studies similar to the present one is spars. Potentially, the small number of subjects (and subsequent selection, number, size and location of sample regions) used to represent a large multi-center cohort could have biased our results. However, there are no indications that the latter was the case. Indeed, if the opposite would be true, we might in extreme cases only have found high SI values for the five selected subjects or subjects belonging to the centers from which they were derived. Nevertheless, we do not know if the SI would improve if more training subjects were used.

Please cite this article as: Dyrby, T.B., et al., Segmentation of age-related white matter changes in a clinical multi-center study, NeuroImage (2008), doi:10.1016/j.neuroimage.2008.02.024

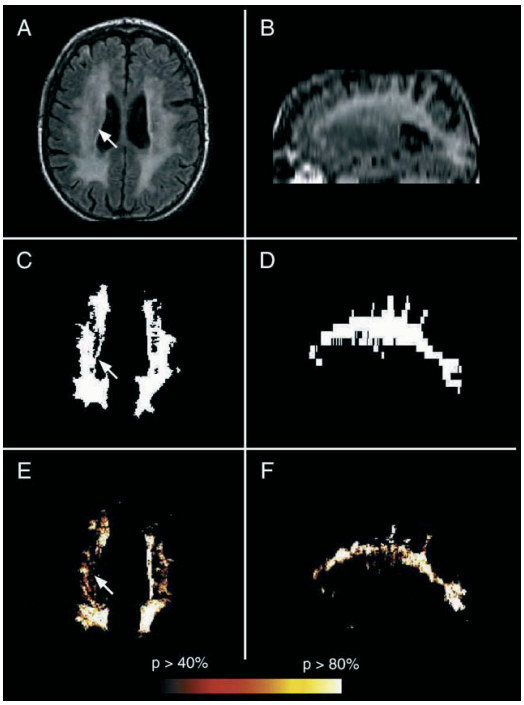

Fig. 7. Subject from center C01 having high WMC volume. Axial (A, C, E) and sagittal (B, D, F) view. Re-sampled FLAIR image (A, B); semi-manual re-sampled WMC VOI (C, D). Probability map of WMC using a F2 neural network (E, F). Manual WMC volume: 117.7 ml; SE=0.19 and SI=0.32. Automatic segmentation was found to be more conservative in detecting WMC compared to manual (arrow).

Future studies on how to optimize the number of training samples are needed to resolve this issue.

The optimal threshold for the WMC probability maps was the value that gave maximum mean SI. We observed that the mean SI (specifically for the multi-modality neural networks) did not fall below 10% of its maximum value over a wide range of thresholds. Therefore, a sub-optimal threshold would not critically alter the quality of segmentations. This indicates that optimized neural networks are robust and able to generalize across a large and heterogeneous multi-center cohort with various degrees of age-related WMC.

The mean SI of 0.56 observed in the present study for the F2 neural network, which achieved the best generalization across the 362 included subjects, lies in the lower end of reported SI values in the literature, e.g. 0.51 (Van Leemput et al 2001), 0.6 (Zijdenbos et al., 2002), 0.75 (Admiraal-Behloul et al., 2005) and 0.8 (Anbeek et al., 2004). However, a direct comparison of SI values between studies is difficult, because we as well as others (Anbeek et al., 2004; Admiraal-Behloul et al., 2005; Zijdenbos et al., 2002) observed that the SI depends on WMC volume, and tends to decrease with lower WMC volumes. In one study, SI also depended on used input features (Anbeek et al., 2004). Finally, studies differ considerably in used pre-processing steps, number of and type of included subjects, subject origin (e.g. single- or multi-center) and WMC volume distribution.

Generally, the neural networks in the present study under- and overestimated WMC volumes at respectively large and small manual WMC volumes. A possible explanation for the underestimation is that in cases with large and diffuse WMC, the actual signal alterations are not as homogeneous as visual inspection might suggest. This might explain why the human rater tended to be more inclusive whereas the opposite was true for the neural networks. In this situation, the SI measure decreases, albeit the large overlap between neural networks and manual segmented WMC voxels as, for example, seen in Fig. 7. In contrast, the increased sensitivity of the neural networks to detect small WMC voxels at low manual WMC volumes led to more false positives, and thus a lower SI. Note that at small WMC volumes false positives have a relative high impact. Although, the manually WMC VOIs were used as ground truth, it might well be that the WMC identified by the neural network are neuropathologically more accurate. Noteworthy, Zijdenbos et al. (2002) noticed that the seven manual raters in their study tended to be more conservative when WMC loads were low and/or poor image quality.

Another factor that might have affected the comparison between the neural network and manual segmentations includes the re-sampling of the semi-manual delineated WMC, obtained at low FLAIR image resolution, into high T1W resolution using a nearest neighbor interpolation. Potentially, nearest neighbor interpolation lowers the specificity of the semi-manual WMC VOI as compared to the high-resolution automatic segmentations. Nevertheless, by up-sampling the FLAIR and T2W images, the detailed structural information in T1W images reduced the impact of the problematic PVE in the FLAIR images. Note that by up-sampling the FLAIR image, the PVE in the re-sampled image was unchanged as compared to the original. Therefore, up-sampling was not expected to deteriorate segmentation results and might partially explain why segmentations improved when the T1W image was used as an input feature. In contrast, down-sampling the high-resolution T1W images to FLAIR resolution would probably result in lower segmentation accuracy since it would introduce more PVE in the re-sampled T1W image, thereby losing its detailed structural information.

Our findings show that segmentations based on the FLAIR image alone had the lowest mean SI. This is most likely due to the substantial variation in FLAIR image quality across the different centers, probably related to differences in scan parameters and MR scanner used (Filippi et al., 1999; Gasperini et al., 2001). In addition, the FLAIR sequences are sensitive to flow artifacts that emerge as hyper-intense WMC (Bakshi et al., 2000; Tanaka et al., 2000). In the present study, false-positive WMC voxels were typically observed on the border of the cortex, in the cerebellum, the septum pellucidum and in the 4th ventricle.

For the multi-modality F2 neural network, the mean SI was improved when including 3×3 neighboring voxels (in axial plane) as an input feature, as compared to F3. Zijdenbos et al. (2002) incorporated local information by applying spatial non-linear anisotropic filtering in their pre-processing, thereby suppressing noise in homogeneous areas within a MR image without affecting tissue boundaries. The problem with such a spatial non-linear filter in the pre-processing phase is the risk of losing contrast of the often already diffuse (age-related) WMC, typically observed in FLAIR images. In contrast, by using neighboring voxels as an input feature, a similar spatial filter effect is "learned" by the neural networks. Although this diminishes the risk of losing contrast, this approach only works if the training data set includes PVE examples.

Using local position as an additional input feature, the multi-modality F1 neural network, as compared to the F2 neural network, seemed to be the best among the six neural networks when only volumetric measures were used in the validation. However, when

Please cite this article as: Dyrby, T.B., et al., Segmentation of age-related white matter changes in a clinical multi-center study, NeuroImage (2008), doi:10.1016/j.neuroimage.2008.02.024

including the SI, which is a measure of spatial agreement, the multimodality F2 neural network performed best. This finding contrasts with Anbeek et al. (2004) who observed that local position as input feature improved the SI. A reason for this discrepancy might be related to the observed asymmetric spatial bias in the probability tissue maps generated by neural network F1 and F4. The weak spatial bias suggests that in the present study the training data set or the generation thereof (e.g. number of training subjects, sample size, location of sample regions, selection of sample voxels or encoding of the spatial feature), used to represent the spatial distribution of voxel position within the brain, might have been insufficient. Retrospectively, one might speculate whether it is possible at all to use relative positional information as a robust input feature in a large study cohort with varying degrees of atrophy and WMC volume. Maybe anatomical templates warped onto the individual brains might provide a more robust way to – on a coarser level than relative positions – spatially represent brain tissues.

Conclusion

In the present study, we showed how optimization of neural networks, input features to these neural networks and network architecture optimization produced reliable probability maps of age-related WMC in the LADIS multi-center study. Pivotal for the successful application, the neural network method was the comprehensive preprocessing pipeline for standardizing image quality. Obviously, segmentation results can only be as good as the image quality provided. It can be expected that high-resolution 3-D FLAIR and T2W sequences in the future allow supervised segmentation methods to reach their full potential. Nevertheless, because of the lack of prior anatomical knowledge, quality inspection of automatic segmentation results by experts should never be underestimated.

Acknowledgment

This study was supported by the European Union (grant QLRT-2000-00446, Impact of age-related brain white matter changes on transition to disability in the elderly "Leukoaraiosis And DISability"). Central data capture was sponsored by the Image Analysis Centre (IAC) in Amsterdam. We would also like to acknowledge the financial support from the Velux Foundation, the Danish Alzheimer Research Foundation and DCSC (Danish Centre for Scientific Computing) grant no. HDW-1104-08'.

Appendix A. List of participating centers and personnel

Helsinki, Finland (Memory Research Unit, Department of Clinical Neurosciences, Helsinki University): Timo Erkinjuntti, MD, PhD, Tarja Pohjasvaara, MD, PhD, Pia Pihanen, MD, Raija Ylikoski, PhD, Hanna Jokinen, LPsych, Meija-Marjut Somerkoski, MPsych; Graz, Austria (Department of Neurology, Medical University): Franz Fazekas, MD, Reinhold Schmidt, MD, Stefan Ropele, PhD, Alexandra Seewann, MD, Katja Petrovic, MagPsychol, Ulrike Garmehi; Lisboa, Portugal (Serviço de Neurologia, Centro de Estudos Egas Moniz, Hospital de Santa Maria): José M. Ferro, MD, PhD, Ana Verdelho, MD, Sofia Madureira, PsyD; Amsterdam, The Netherlands (Department of Neurology, VU Medical Center): Philip Scheltens, MD, PhD, Ilse van Straaten, MD, Alida Gouw, MD, Wiesje van de Flier, PhD, Frederik Barkhof, MD, PhD; Goteborg, Sweden (Institute of Clinical Neuroscience, Goteborg University): Anders Wallin, MD, PhD, Michael Jonsson, MD, Karin Lind, MD, Arto Nordlund, PsyD, Sindre Rolstad, PsyD, Kerstin Gustavsson, RN; Huddinge, Sweden (Karolinska Institute, Department of Clinical Neuroscience and Family Medicine, Huddinge University Hospital): Lars-Olof Wahlund, MD, PhD, Militta Crisby, MD, PhD, Anna Pettersson, physiotherapist, Kaarina Amberla, PsyD; Paris, France (Department of Neurology, Hopital Lariboisiere): Hugues Chabriat, MD, PhD, Ludovic Benoit, MD, Karen Hernandez, Solene Pointeau, Annie Kurtz, Daniel Reizine, MD; Mannheim, Germany (Department of Neurology, University of Heidelberg, Klinikum Mannheim): Michael Hennerici, MD, Christian Blahak, MD, Hansjorg Baezner, MD, Martin Wiarda, PsyD, Susanne Seip, RN; Copenhagen, Denmark (Memory Disorders Research Group, Department of Neurology, Rigshospitalet, and the Danish Research Centre for Magnetic Resonance, Hvidovre Hospital, Copenhagen University Hospital): Gunhild Waldemar, MD, DMSc, Egill Rostrup, MD, MSc; Charlotte Ryberg, MSc, Tim B. Dyrby MSc, Olaf B. Paulson, MD, DMSc; Newcastle-upon-Tyne, UK (Institute for Ageing and Health, University of Newcastle): John O'Brien, DM, Sanjeet Pakrasi, MRCPsych, Thais Minnet, PhD, Michael Firbank, PhD, Jenny Dean, PhD, Pascale Harrison, BSc, Philip English, DCR; Florence, Italy–Coordinating centre (Department of Neurological and Psychiatric Sciences, University of Florence): Domenico Inzitari, MD (Study Coordinator), Leonardo Pantoni, MD, PhD, Anna Maria Basile, MD, Michela Simoni, MD, Giovanni Pracucci, MD, Monica Martini, MD, Eliana Magnani, MD, Anna Poggesi, MD, Luciano Bartolini, PhD, Emilia Salvadori, PhD, Marco Moretti, MD, Mario Mascalchi, MD, PhD.

The LADIS Steering Committee is formed by Domenico Inzitari, MD (study coordinator), Timo Erkinjuntti, MD, PhD, Philip Scheltens, MD, PhD, Marieke Visser, MD, PhD, and Peter Langhorne, MD, BSC, PhD, FRCP who replaced in this role Kjell Asplund, MD, PhD, beginning 2005.

References

Admiraal-Behloul, F., van den Heuvel, D.M., Olofsen, H., van Osch, M.J., van der, G.J., van Buchem, M.A., Reiber, J.H., 2005. Fully automatic segmentation of white matter hyperintensities in MR images of the elderly. Neuroimage 28, 607–617.

Alfano, B., Brunetti, A., Larobina, M., Quarantelli, M., Tedeschi, E., Ciarmiello, A., Covelli, E.M., Salvatore, M., 2000. Automated segmentation and measurement of global white matter lesion volume in patients with multiple sclerosis. J. Magn. Reson. Imaging 12, 799–807.

Alirezaie, J., Jernigan, M.E., Nahmias, C., 1995. Neural network-based segmentation of magnetic resonance images of the brain. Nucl. Sci. Symp. Med. Imaging (NSS/MIC) 44, 194–198.

Anbeek, P., Vincken, K.L., van Osch, M.J., Bisschops, R.H., van der Grond, J., 2004. Probabilistic segmentation of white matter lesions in MR imaging. Neuroimage 21, 1037–1044.

Ashburner, J., Friston, K., 1997. Multimodal image coregistration and partitioning—a unified framework. Neuroimage 6, 209–217.

Bakshi, R., Caruthers, S.D., Janardhan, V., Wasay, M., 2000. Intraventricular CSF pulsation artifact on fast fluid-attenuated inversion-recovery MR images: analysis of 100 consecutive normal studies. AJNR Am. J. Neuroradiol. 21, 503–508.

Bartko, J.J., 1991. Measurement and reliability: statistical thinking considerations. Schizophr. Bull. 17, 483–489.

Bishop, C., 1995. Neural Networks for Pattern Recognition. Oxford University Press.

DeCarli, C., Fletcher, E., Ramey, V., Harvey, D., Jagust, W.J., 2005. Anatomical mapping of white matter hyperintensities (WMH): exploring

the relationships between periventricular WMH, deep WMH, and total WMH burden. Stroke 36, 50–55.

Dyrby, T., Liptrot, M.G., 2005. Standardizing MR image intensity in multi-center studies. Proc. Int. Soc. Magn. Reson. Med. 13, 631.

Erickson, B.J., Avula, R.T.V., 1998. Algorithm for automatic segmentation and classification of magnetic resonance brain images. J. Digit. Imaging 11, 74–82.

Fazekas, F., Barkhof, F., Wahlund, L.O., Pantoni, L., Erkinjuntti, T., Scheltens, P., Schmidt, R., 2002. CT and MRI rating of white matter lesions. Cerebrovasc. Dis. 13 (Suppl 2), 31–36.

Filippi, M., Rocca, M.A., Gasperini, C., Sormani, M.P., Bastianello, S., Horsfield, M.A., Pozzilli, C., Comi, G., 1999. Interscanner variation in brain MR lesion load measurements in multiple sclerosis using conventional spin-echo, rapid relaxation-enhanced, and fast-FLAIR sequences. AJNR Am. J. Neuroradiol. 20, 133–137.

Gasperini, C., Rovaris, M., Sormani, M.P., Bastianello, S., Pozzilli, C., Comi, G., Filippi, M., 2001. Intra-observer, inter-observer and inter-scanner variations in brain MRI volume measurements in multiple sclerosis. Mult. Scler. 7, 27–31.

Goldberg-Zimring, D., Achiron, A., Miron, S., Faibel, M., Azhari, H., 1998. Automated detection and characterization of multiple sclerosis lesions in brain MR images. Magn. Reson. Imaging 16, 311–318.

Jack Jr., C.R., O'Brien, P.C., Rettman, D.W., Shiung, M.M., Xu, Y., Muthupillai, R., Manduca, A., Avula, R., Erickson, B.J., 2001. FLAIR histogram segmentation for measurement of leukoaraiosis volume. J. Magn. Reson. Imaging 14, 668–676.

Jackson, E.F., Narayana, P.A., Wolinsky, J.S., Doyle, T.J., 1993. Accuracy and reproducibility in volumetric analysis of multiple sclerosis lesions [magnetic resonance imaging]. J. Comput. Assist. Tomogr. 17, 200–205.

Kamber, M., Shinghal, R., Collins, D.L., Francis, G.S., Evans, A.C., 1995. Model-based 3-D segmentation of multiple sclerosis lesions in magnetic resonance brain images. IEEE Trans. Med. Imaging 14, 442–453.

Kapeller, P., Barber, R., Vermeulen, R.J., Ader, H., Scheltens, P., Freidl, W., Almkvist, O., Moretti, M., del Ser, T., Vaghfeldt, P., Enzinger, C., Barkhof, F., Inzitari, D., Erkinjunti, T., Schmidt, R., Fazekas, F., 2003. Visual rating of age-related white matter changes on magnetic resonance imaging: scale comparison, interrater agreement, and correlations with quantitative measurements. Stroke 34, 441–445.

Kikinis, R., Guttmann, C.R., Metcalf, D., Wells III, W.M., Ettinger, G.J., Weiner, H.L., Jolesz, F.A., 1999. Quantitative follow-up of patients with multiple sclerosis using MRI: technical aspects. J. Magn. Reson. Imaging 9, 519–530.

Lao, L., Shen, D., Jawad, A., Karacali, B., Liu, D., Melhen, E.R., Bryan, R.N., Davatzikos, C., 2006. Automated segmentation of white matter lesions in 3D brain MR images, using multivariate pattern classification. ISBI 307–310.

Lawton, M.P., Brody, E.M., 1969. Assessment of older people: self-maintaining and instrumental activities of daily living. Gerontologist 9, 179–186.

Le Cun, Y., Denker, J.S., Solla, S.A., 1990. Optimal brain damage. In: Touretzky, D.S. (Ed.), Advances in Neural Information Processing Systems. Morgan Kauffman, pp. 598–605.

Lopez, O.L., Becker, J.T., Jungreis, C.A., Rezek, D., Estol, C., Boller, F., DeKosky, S.T., 1995. Computed tomography–but not magnetic resonance imaging—identified periventricular white-matter lesions predict symptomatic cerebrovascular disease in probable Alzheimer's disease. Arch. Neurol. 52, 659–664.

Özkan, M., Dawant, B.M., Maciunas, R.J., 1993. Neural-network-based segmentation of multi-modal medical images: a comparative and prospective study. IEEE Trans. Med. Imaging 12, 534–544.

Pantoni, L., 2002. Pathophysiology of age-related cerebral white matter changes. Cerebrovasc. Dis. 13 (Suppl 2), 7–10.

Pantoni, L., Basile, A.M., Pracucci, G., Asplund, K., Bogousslavsky, J., Chabriat, H., Erkinjuntti, T., Fazekas, F., Ferro, J.M., Hennerici, M., O'brien, J., Scheltens, P., Visser, M.C., Wahlund, L.O., Waldemar, G., Wallin, A., Inzitari, D., 2005. Impact of age-related cerebral white matter changes on the transition to disability—the LADIS study: rationale, design and methodology. Neuroepidemiology 24, 51–62.

Rask, T., Dyrby, T., Comerci, M., Quarantelli, M., Alfano, B., Berkouk, K., Baron, J., Colchester, A., Hojjat, A., Knudsen, G.M., Paulson, O.B., Svarer, C., 2004. PVE-lab: software for correction of functional images for partial volume errors. Annu. Meet. Organ. Hum. Brain Mapp.

Rey, D., Subsol, G., Delingette, H., Ayache, N., 2002. Automatic detection and segmentation of evolving processes in 3D medical images: application to multiple sclerosis. Med. Image Anal. 6, 163–179.

Scheltens, P., Barkhof, F., Fazekas, F., 2003. White-matter changes on MRI as surrogate marker. Int. Psychogeriatr. 15 (Suppl 1), 261–265.

Scheltens, P., Erkinjunti, T., Leys, D., Wahlund, L.O., Inzitari, D., del Ser, T., Pasquier, F., Barkhof, F., Mantyla, R., Bowler, J., Wallin, A., Ghika, J., Fazekas, F., Pantoni, L., 1998. White matter changes on CT and MRI: an overview of visual rating scales. European Task Force on Age-Related White Matter Changes. Eur. Neurol. 39, 80–89.

Schwarz, G., 1978. Estimating the dimension of a model. Ann. Stat. 6, 461–464.

Sled, J.G., Zijdenbos, A.P., Evans, A.C., 1998. A nonparametric method for automatic correction of intensity nonuniformity in MRI data. IEEE Trans. Med. Imaging 17, 87–97.

Tanaka, N., Abe, T., Kojima, K., Nishimura, H., Hayabuchi, N., 2000. Applicability and advantages of flow artifact-insensitive fluid-attenuated inversion-recovery MR sequences for imaging the posterior fossa. AJNR Am. J. Neuroradiol. 21, 1095–1098.

Van Leemput, K., Maes, F., Vandermeulen, D., Colchester, A., Suetens, P., 2001. Automated segmentation of multiple sclerosis lesions by model outlier detection. IEEE Trans. Med. Imaging 20, 677–688.

van Straaten, E.C., Scheltens, P., Barkhof, F., 2004. MRI and CT in the diagnosis of vascular dementia. J. Neurol. Sci. 226, 9–12.

van Straaten, E.C., Fazekas, F., Rostrup, E., Scheltens, P., Schmidt, R., Pantoni, L., Inzitari, D., Waldemar, G., Erkinjuntti, T., Mantyla, R., Wahlund, L.O., Barkhof, F., 2006. Impact of white matter hyperintensities scoring method on correlations with clinical data. The LADIS Study. Stroke 37, 836–840.

Wahlund, L.O., Barkhof, F., Fazekas, F., Bronge, L., Augustin, M., Sjogren, M., Wallin, A., Ader, H., Leys, D., Pantoni, L., Pasquier, F., Erkinjuntti, T., Scheltens, P., 2001. A new rating scale for age-related white matter changes applicable to MRI and CT. Stroke 32, 1318–1322.

Wen, W., Sachdev, P., 2004. The topography of white matter hyperintensities on brain MRI in healthy 60- to 64-year-old individuals. Neuroimage 22, 144–154.

Wu, M., Rosano, C., Butters, M., Whyte, E., Nable, M., Crooks, R., Meltzer, C.C., Reynolds III, C.F., Aizenstein, H.J., 2006. A fully automated method for quantifying and localizing white matter hyperintensities on MR images. Psychiatry Res. 148, 133–142.

Zijdenbos, A.P., Dawant, B.M., Margolin, R.A., Palmer, A.C., 1994. Morphometric analysis of white matter lesions in MR images: method and validation. IEEE Trans. Med. Imaging 13, 716–724.

Zijdenbos, A.P., Forghani, R., Evans, A.C., 2002. Automatic "pipeline" analysis of 3-D MRI data for clinical trials: application to multiple sclerosis. IEEE Trans. Med. Imaging 21, 1280–1291.

Please cite this article as: Dyrby, T.B., et al., Segmentation of age-related white matter changes in a clinical multi-center study, NeuroImage (2008), doi:10.1016/j.neuroimage.2008.02.024

Manuscript IV

Dyrby T. Liptrot M.G., Standardizing MR image Intensity In Multi-Center Studies. (Oral presentation) Proc Intl Soc Magn Reson Med 2005. (Miami, USA)

Standardizing MR image intensity in multi-centre studies

T. Dyrby[1], M. Liptrot[1]
[1]Danish Research Centre for MR, Copenhagen University Hospital, Hvidovre, Denmark

Introduction

The standardization of the inter-subject intensities of MR images acquired with the same protocol is an important, but not a simple, task required by many analysis schemes. Its importance becomes even clearer once analysis is to be performed on data from large multi-centre trials, which often involve a variety of scanner manufacturers, field strengths and an inherent diversity of protocols. When the outcome of such trials is the comparison of the outcome of identical methods upon the data, then it is imperative that the starting points are the same. Methods such as intensity-based segmentation algorithms are inherently sensitive to variations in the intensity distribution. In existing methods, e.g. histogram matching [1,2], the shape of the histogram is not guaranteed to be preserved, making it difficult to compare histograms between normal and diseased brain volumes. With this in mind a new intensity standardization method is introduced where the shape of the histogram is preserved.

Method

A multi-stage approach is taken. First image artefacts such as RF inhomogenity, and intra-slice intensity variation in data acquired interleaved, are corrected. Then, samples from two of the three major tissue classes (e.g. grey-matter (GM), white-matter (WM) and CSF) within the modality to be corrected are required. To do this a simple pre-segmentation is needed, which is simplest to perform on a co-registered image from a modality with clearly defined classes e.g. a T1-weighted protocol. Conservative borders between the classes are found, and only the upper 80% of voxels within each thus-obtained class are then used as samples for the next stage. By obtaining such a robust, highly homogenous sample set, problems of partial-volume, non-brain, mixed class, and disease-induced distortions are suppressed. These samples are then used for the normalization stage. Here the mean and the standard deviation of two classes are determined, and then used to zero-mean the entire dataset, and to fix the standard deviation (std) at 1. Finally, in order to avoid any negative-valued voxels, a 'de-normalization' is applied where a new (arbitrary) mean and standard deviation are applied to the dataset. The values chosen have no effect upon the image appearance as the contrast-to-noise ratio (CNR) between tissue classes is maintained.

$$CNR_{AB} = 20 \cdot \log \left(\frac{|\mu_A - \mu_B|}{\sqrt{\frac{\sigma_A^2 \cdot N_A + \sigma_B^2 \cdot N_B}{N_A + N_B}}} \right) \quad [dB]$$

The CNR_{AB} is an image contrast measure based on the relative separation between two intensity distributions where μ_A is the mean intensity of tissue A, σ_A the standard deviation and N_A the number of voxels. Similarly for B.

Results

Over a three year period 487 brain volumes were scanned at 9 different centres in the European LADIS (Leukoraiosis And DISability) project with different protocols. Here the T1-weighted Magnetization-Prepared Gradient-Echo (MPRAGE) protocol was used for the validation due to its optimal tissue contrast. CSF and WM were used as primary tissue classes and the de-normalisation factors were set to mean=150 and std=15. The mean values from the three dominating tissue classes before and after normalization are shown in Figure 1. Beforehand, intensity variation is observed even within centres. The extremely large variation in centre 3 can be explained by the use of different scanners. After normalisation, the inter-subject and tissue variation are clearly standardized. The CNR between all three tissue classes remains unchanged ($p>0.96$, paired t-test), indicating that the images are visually identical post standardization. Outliers caused by incorrect protocol parameters are easy to isolate, e.g. in subject 151 and 155, GM and WM are overlapping indicating low initial image quality (prior $CNR_{GM\text{-}WM}$ -150dB and -220dB respectively), verified by visual inspection in Figure 2. Note that even in presence of erroneous images, the method performs correctly, and original CNR is maintained.

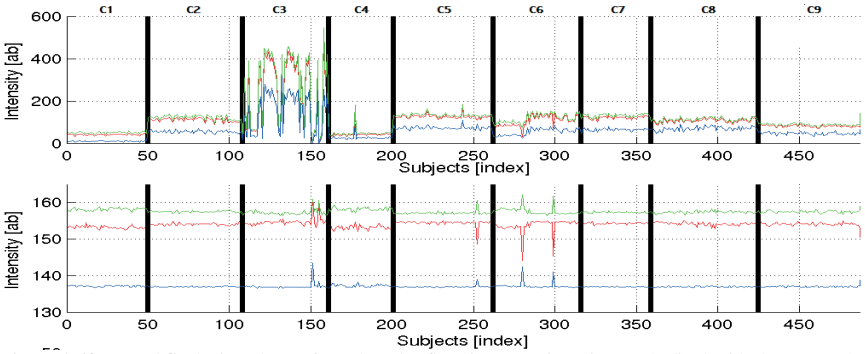

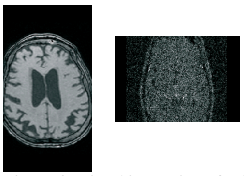

Figure 2: Visual inspection of subject 155 and 151 (right) before intensity normalisation. The low $CNR_{GM\text{-}WM}$ after normalisation can be explained by low prior image quality.

Figure 1 487 MPRAGE brain volumes from the LADIS project were intensity standardized with the proposed method. (y-axis) Mean intensity values of dominating tissues found by pre-segmentation of CSF (blue), GM (red), WM (green). (x-axis) Subjects divided into the 9 different centres (C1-C9). C3 used a 0.5 Tesla MR scanner, all others a 1.5 Tesla scanner. Top) Before and Bottom) after intensity standardization were tissues classes of all subjects are seen to be homogeneous.

Conclusion

A new approach to intensity normalization has been developed. It overcomes the problems inherent in many other methods such as histogram-matching, because the shapes of the histograms are preserved. In addition, the CNR is maintained so there is no effect upon subjective rating. The result is the ability to perform identical pre- and post-processing, and analysis methods on all scans from different MR centres with no bias.

References

1 Nyul LG, Udupa JK., On standardizing the MR image intensity scale. MRM. 1999 Dec;42(6):1072-81.
2 Wang L, Lai HM, et al., Correction for variations in MRI scanner sensitivity in brain studies with histogram matching. MRM. 1998 Feb;39(2):322-7.